2011

Effect of rib aspect ratio on heat transfer and friction in rectangular channels

Lucky Vo Tran
University of Central Florida

EFFECT OF RIB ASPECT RATIO ON HEAT TRANSFER AND FRICTION IN RECTANGULAR CHANNELS

by

LUCKY VO TRAN

A thesis submitted in partial fulfillment of the requirements
for the Honors in the Major Program in Mechanical Engineering
in the Department of Mechanical, Materials, and Aerospace Engineering
in the College of Engineering and Computer Science
at the University of Central Florida
Orlando, Florida

Fall Term
2011

Thesis Chair: Dr. Jayanta S. Kapat

ABSTRACT

The heat transfer and friction augmentation in the fully developed portion of a 2:1 aspect ratio rectangular channel with orthogonal ribs at channel Reynolds numbers of 20,000, 30,000, and 40,000 is studied both experimentally and computationally. Ribs are applied to the two opposite wide walls. The rib aspect ratio is varied systematically at 1, 3, and 5, with a constant rib height and constant rib pitch (rib-pitch-to-rib-height ratio of 10). The purpose of the study is to extend the knowledge of the performance of rectangular channels with ribs to include high aspect ratio ribs. The experimental investigation is performed using the transient Thermochromic Liquid Crystals technique to measure the distribution of the local Nusselt numbers on the ribbed walls. Overall channel pressure drop and friction factor augmentation is also obtained with the experimental setup. A numerical simulation is also performed by solving the 3-D Reynolds-averaged Navier-Stokes equations using the realizable-k-ϵ turbulence model for closure. Flow visualization is obtained from the computational results as well as numerical predictions of local distributions of Nusselt numbers and overall channel pressure drop. Results indicate that with increasing rib width, the heat transfer augmentation of the ribbed walls decreases with a corresponding reduction in channel pressure drop.

DEDICATION

To all of mankind who were born on Earth

ACKNOWLEDGMENTS

A special thanks to my professor, Dr. Jay S. Kapat, for his guidance, mentorship, and commitment to my continued growth throughout the years have been overwhelmingly daring. In particular, his overly busy schedules and lack of restraint allowed me the freedom to explore the many topics of internal cooling and expand my portfolio as an engineering researcher.

My sincerest gratitude goes to my two fellow graduate student mentors Carson D. Slabaugh and Michelle I. Valentino; to whom the distinction of my undergraduate status was never fretted against. The unnaturally high level of coherent team work that I enjoyed with these two was definitely a contributing factor to my health, productivity, and success as an undergraduate researcher. I feel most fortunate to have been able to have had these two as colleagues, for they were my twin pillars of support during my most vulnerable times as a young student.

Additional thanks again to Michelle, who helped to design and establish the new TLC setup and then together, faithfully we endured the more than dozen failed attempts to debug the rig. Her subtle efforts were not any less essential than my own. I wish her the greatest fortune in the upcoming phases of her life as she leaves UCF.

This work was performed at the Siemens Energy Center – a research laboratory made possible through funds from Siemens Energy. Part of the resources used was made available through the Florida Center for Advanced AeroPropulsion (FCAAP). This thesis was completed utilizing the experience and facilities of the Laboratory for Turbine Aerodynamics, Heat

Transfer, and Durability a part of the Center for Advanced Turbines and Energy Research at the University of Central Florida.

Finally I would like to acknowledge the love and support of my family members, especially my many younger siblings who continuously invigorate my existence.

TABLE OF CONTENTS

NOMENCLATURE xviii

INTRODUCTION 1

Turbomachinery 2

The Gas Turbine Engine 2

Generators 6

More Heat, Less Friction 8

Internal Cooling 11

Rib-Shaped Turbulators 13

Overview of Present Work 22

Rib Configurations 23

Thermochromatic Liquid Crystals 25

Computational Fluid Dynamics 26

The Problem of Turbulence 27

The Reynolds-averaged Navier-Stokes equations 28

Turbulence modeling 30

The realizable-k-ϵ model 31

The boundary layer and near-wall treatments 31

Near-wall treatments and y^+ 32

Periodic Flows....34
EXPERIMENTAL METHOD....37
Experimental Setup....38
Experimental Procedure....43
Friction Factor Testing....43
Heat Transfer Testing....44
Data Reduction....45
The Semi-Infinite Solid....49
Lumped Capacitance Model....52
Post-Processing....55
Experimental Uncertainty....58
Experimental Results....58
Smooth Wall Validation....59
Case A1: 1:1 Rib Aspect Ratio Local Heat Transfer Results....65
Case A3: 3:1 Rib Aspect Ratio Local Heat Transfer Results....67
Case A5: 5:1 Rib Aspect Ratio Local Heat Transfer Results....69
Comparison of Experimental Local Heat transfer Results....71
Comparison of Experimental Spanwise Averaged Heat transfer Results....73
Comparison of Experimental Friction Results....77

Comparison of Numerical Rib and Wall Averaged Heat Transfer Results 79

COMPUTATIONAL METHOD 82

Mesh Generation 84

Solution Monitors 92

Solution Strategy 93

Computational Results 100

Wall y^+ 100

Flow visualization: A1 102

Flow visualization: A3 113

Flow visualization: A5 123

Case A1: 1:1 Rib Aspect Ratio Local Heat Transfer Results 133

Case A3: 3:1 Rib Aspect Ratio Local Heat Transfer Results 138

Case A5: 5:1 Rib Aspect Ratio Local Heat Transfer Results 144

Comparison of Numerical Friction Results 150

Comparison of Numerical Rib and Wall Averaged Heat Transfer Results 152

COMPARISON OF EXPERIMENTAL AND NUMERICAL RESULTS 154

Comparison of Friction Results 154

Comparison of Heat Transfer Results 157

CONCLUSION 162

REFERENCES 165

APPENDIX A: EXPERIMENTALLY MEASURED STATIC PRESSURE DISTRIBUTIONS IN RIBBED CHANNELS 171

APPENDIX B: EXPERIMENTAL FRICTION RESULTS 177

APPENDIX C: EXPERIMENTAL HEAT TRANSFER RESULTS 179

APPENDIX D: NUMERICAL FRICTION RESULTS 182

APPENDIX F: NUMERICAL HEAT TRANSFER RESULTS 184

LIST OF FIGURES

Figure 1: Brayton cycle schematic 3

Figure 2: Advances in turbine entry temperature from new cooling schemes (Lakshminarayana, 1996) 4

Figure 3: Typical cooled aircraft turbine blade (Gladden & Simoneau, 1989) 6

Figure 4: Cross section of hydrogen-cooled turbogenerator rotor slots (Eriksson, 2007) 7

Figure 5: Rib spacing effect studied by (Liu, Wright, Fu, & Han, 2006) 16

Figure 6: Angled rib configurations studied by (Wright & Gohardani, 2008) 18

Figure 7: Building block approach to turbine aerothermal research (Gladden & Simoneau, 1989) 20

Figure 8: Channel cross section 23

Figure 9: Rib nomenclature 23

Figure 10: Aligned rib configurations, A1 (top), A3 (middle), A5 (bottom) 24

Figure 11: TLC bandwidth and crystallic phases 25

Figure 12: Schematic of Experimental Setup 39

Figure 13: Test Section Assembly 40

Figure 14: Camera and lighting setup for TLC experiment 42

Figure 15: Static pressure distribution 47

Figure 16: 1-D Semi-infinite solid domain 49

Figure 17: Centerline entrance temperature at start of viewing window 52

Figure 18: Rib surface area denotations 55

Figure 19: TLC processing flow chart 56

Figure 20: Time history of recorded green intensities 57
Figure 21: Local heat transfer augmentation of smooth wall validation 60
Figure 22: Static pressure distribution of Smooth Wall at 20,000 Re 62
Figure 23: Static pressure distribution of Smooth Wall at 30,000 Re 62
Figure 24: Static pressure distribution of Smooth Wall at 40,000 Re 63
Figure 25: Local heat transfer augmentation of Case A1.....66
Figure 26: Local heat transfer augmentation of Case A3.....68
Figure 27: Local heat transfer augmentation of Case A5.....70
Figure 28: Local heat transfer augmentation of ribbed walls at 30,000 Re 72
Figure 29: Spanwise-averged heat transfer augmentation of ribbed walls at 30,000 Re.....74
Figure 30: Experimental friction factor.....78
Figure 31: Experimental friction factor augmentation.....79
Figure 32: Heat transfer augmentation on rib from experimental study.....80
Figure 33: Average heat transfer augmentation on ribbed walls from experimental study 80
Figure 34: Computational domain 83
Figure 35: Case A1 topology.....85
Figure 36: Case A3 topology.....85
Figure 37: Case A5 Topology.....86
Figure 38: Mesh cross section over ribbed section for Case A1 88
Figure 39: Mesh cross section over non-ribbed section for Case A1 88
Figure 40: Mesh outline of Case A1 at symmetry plane.....89
Figure 41: Mesh near rib of Case A1 at symmetry plane.....89

Figure 42: Mesh near rib of Case A3 at symmetry plane 90
Figure 43: Mesh outline of Case A3 at symmetry plane 90
Figure 44: Mesh outline of Case A5 at symmetry plane 91
Figure 45: Mesh near rib of Case A5 at symmetry plane 91
Figure 46: Skin friction coefficient monitors for Case A3 at 40,000 Re 96
Figure 47: Streamwise velocity monitors for Case A3 at 40,000 Re 96
Figure 48: Fluid temperature monitors for Case A3 at 40,000 Re 97
Figure 49: Heat transfer coefficient monitors for Case A3 at 40,000 Re 98
Figure 50: Wall y^+ contours of Case A1 at 40,000 Re 100
Figure 51: Wall y^+ contours of Case A3 at 40,000 Re 101
Figure 52: Wall y^+ contours of Case A5 at 40,000 Re 101
Figure 53: Contours of streamwise velocity at the symmetry plane for Case A1 at 20,000 Re .. 102
Figure 54: Contours of streamwise velocity at the symmetry plane for Case A1 at 30,000 Re .. 103
Figure 55: Contours of streamwise velocity at the symmetry plane for Case A1 at 40,000 Re .. 103
Figure 56: Contours of normal velocity at the symmetry plane for Case A1 at 20,000 Re 105
Figure 57: Contours of normal velocity at the symmetry plane for Case A1 at 30,000 Re 105
Figure 58: Contours of normal velocity at the symmetry plane for Case A1 at 40,000 Re 106
Figure 59: Vector plot of absolute velocity at the symmetry plane for Case A1 at 20,000 Re ... 108
Figure 60: Vector plot of absolute velocity at the symmetry plane for Case A1 at 30,000 Re ... 108
Figure 61: Vector plot of absolute velocity at the symmetry plane for Case A1 at 30,000 Re ... 109
Figure 62: Turbulence intensity at the symmetry plane for Case A1 at 20,000 Re 111
Figure 63: Turbulence intensity at the symmetry plane for Case A1 at 30,000 Re 111

Figure 64: Turbulence intensity at the symmetry plane for Case A1 at 40,000 Re.....112

Figure 65: Contours of streamwise velocity at the symmetry plane for Case A3 at 20,000 Re..113

Figure 66: Contours of streamwise velocity at the symmetry plane for Case A3 at 30,000 Re..114

Figure 67: Contours of streamwise velocity at the symmetry plane for Case A3 at 40,000 Re..114

Figure 68: Contours of normal velocity at the symmetry plane for Case A3 at 20,000 Re 116

Figure 69: Contours of normal velocity at the symmetry plane for Case A3 at 30,000 Re 117

Figure 70: Contours of normal velocity at the symmetry plane for Case A3 at 40,000 Re 117

Figure 71: Vector plot of absolute velocity at the symmetry plane for Case A3 at 20,000 Re...119

Figure 72: Vector plot of absolute velocity at the symmetry plane for Case A3 at 30,000 Re...119

Figure 73: Vector plot of absolute velocity at the symmetry plane for Case A3 at 40,000 Re...120

Figure 74: Turbulence intensity at the symmetry plane for Case A3 at 20,000 Re.....121

Figure 75: Turbulence intensity at the symmetry plane for Case A3 at 30,000 Re.....122

Figure 76: Turbulence intensity at the symmetry plane for Case A3 at 40,000 Re.....122

Figure 77: Contours of streamwise velocity at the symmetry plane for Case A5 at 20,000 Re..124

Figure 78: Contours of streamwise velocity at the symmetry plane for Case A5 at 30,000 Re..124

Figure 79: Contours of streamwise velocity at the symmetry plane for Case A5 at 40,000 Re..125

Figure 80: Contours of normal velocity at the symmetry plane for Case A5 at 20,000 Re 126

Figure 81: Contours of normal velocity at the symmetry plane for Case A5 at 30,000 Re 127

Figure 82: Contours of normal velocity at the symmetry plane for Case A5 at 40,000 Re 127

Figure 83: Vector plot of absolute velocity at the symmetry plane for Case A5 at 20,000 Re...129

Figure 84: Vector plot of absolute velocity at the symmetry plane for Case A5 at 30,000 Re...129

Figure 85: Vector plot of absolute velocity at the symmetry plane for Case A5 at 40,000 Re...130

Figure 86: Turbulence intensity at the symmetry plane for Case A5 at 20,000 Re.....131
Figure 87: Turbulence intensity at the symmetry plane for Case A5 at 30,000 Re.....132
Figure 88: Turbulence intensity at the symmetry plane for Case A5 at 40,000 Re.....132
Figure 89: Local heat transfer augmentation on ribbed wall of Case A1 at 20,000 Re.....134
Figure 90: Local heat transfer augmentation on non-ribbed wall of Case A1 at 20,000 Re.....134
Figure 91: Local heat transfer augmentation on ribbed wall of Case A1 at 30,000 Re.....135
Figure 92: Local heat transfer augmentation on non-ribbed wall of Case A1 at 30,000 Re.....135
Figure 93: Local heat transfer augmentation on ribbed wall of Case A1 at 40,000 Re.....136
Figure 94: Local heat transfer augmentation on non-ribbed wall of Case A1 at 40,000 Re.....136
Figure 95: Local heat transfer augmentation on ribbed wall of Case A3 at 20,000 Re.....139
Figure 96: Local heat transfer augmentation on non-ribbed wall of Case A3 at 20,000 Re.....139
Figure 97: Local heat transfer augmentation on ribbed wall of Case A3 at 30,000 Re.....140
Figure 98: Local heat transfer augmentation on non-ribbed wall of Case A3 at 30,000 Re.....141
Figure 99: Local heat transfer augmentation on ribbed wall of Case A3 at 40,000 Re.....142
Figure 100: Local heat transfer augmentation on non-ribbed wall of Case A3 at 40,000 Re.....142
Figure 101: Local heat transfer augmentation on ribbed wall of Case A5 at 20,000 Re.....144
Figure 102: Local heat transfer augmentation on non-ribbed wall of Case A5 at 20,000 Re.....145
Figure 103: Local heat transfer augmentation on ribbed wall of Case A5 at 30,000 Re.....146
Figure 104: Local heat transfer augmentation on non-ribbed wall of Case A5 at 30,000 Re.....146
Figure 105: Local heat transfer augmentation on ribbed wall of Case A5 at 40,000 Re.....147
Figure 106: Local heat transfer augmentation on non-ribbed wall of Case A5 at 40,000 Re.....148
Figure 107: Numerical friction factor.....150

Figure 108: Numerical friction factor augmentation 151

Figure 109: Heat transfer augmentation on rib from numerical study.....152

Figure 110: Average heat transfer augmentation on ribbed walls from numerical study 153

Figure 111: Comparison of experimental and numerical friction factor.....155

Figure 112: Comparison of experimental and numerical friction augmentation.....156

Figure 113: Comparison of rib-averaged heat transfer augmentation 158

Figure 114: Comparison of heat transfer augmentation in non-ribbed portion.....159

Figure 115: Comparison of ribbed wall averaged heat transfer augmentation.....160

Figure 116: Static pressure distribution of Case A1 at 20,000 Re.....172

Figure 117: Static pressure distribution of Case A1 at 30,000 Re.....172

Figure 118: Static pressure distribution of Case A1 at 40,000 Re.....173

Figure 119: Static pressure distribution of Case A3 at 20,000 Re.....173

Figure 120: Static pressure distribution of Case A3 at 30,000 Re.....174

Figure 121: Static pressure distribution of Case A3 at 40,000 Re.....174

Figure 122: Static pressure distribution of Case A5 at 20,000 Re.....175

Figure 123: Static pressure distribution of Case A5 at 30,000 Re.....175

Figure 124: Static pressure distribution of Case A5 at 40,000 Re.....176

LIST OF TABLES

Table 1: Rib parameters in current study 24

Table 2: Regions within the inner layer 33

Table 3: Ratios of rib and projected surface areas 55

Table 4: Wall-averaged heat transfer augmentation for Smooth Wall Validation 61

Table 5: Summary of experimental friction results for smooth wall validation 64

Table 6: Computational test matrix 84

Table 7: Mesh density parameters 87

Table 8: Monitor locations 92

Table 9: Computational test matrix 93

Table 10: Properties used in Fluent runs 94

Table 11: Boundary conditions at each Reynolds number 95

Table 12: Summary of experimental friction results for Case A1 178

Table 13: Summary of experimental friction results for Case A3 178

Table 14: Summary of experimental friction results for Case A5 178

Table 15: Summary of experimental heat transfer augmentation results for Case A1 180

Table 16: Summary of experimental heat transfer augmentation results for Case A3 180

Table 17: Summary of experimental heat transfer augmentation results for Case A5 180

Table 18: Wall-averaged heat transfer results for Case A1 from TLC 181

Table 19: Wall-averaged heat transfer for Case A3 from TLC 181

Table 20: Wall-averaged heat transfer results for Case A5 from TLC 181

Table 21: Summary of numerical friction results for Case A1 183

Table 22: Summary of numerical friction results for Case A3 183

Table 23: Summary of numerical friction results for Case A5 183

Table 24: Summary of numerical heat transfer augmentation results for Case A1 185

Table 25: Summary of numerical heat transfer augmentation results for Case A3 185

Table 26: Summary of numerical heat transfer augmentation results for Case A5 185

Table 27: Wall-averaged heat transfer results for Case A1 from CFD 186

Table 28: Wall-averaged heat transfer results for Case A3 from CFD 186

Table 29: Wall-averaged heat transfer results for Case A5 from CFD 186

NOMENCLATURE

Roman Symbols

A	=	cross-sectional area
A	=	bulk temperature curve fit spatial variation coefficient
A_s	=	convective surface area
A_p	=	projected smooth wall area
A_{actual}	=	total convective surface area of ribbed wall
A_{sw}	=	projected smooth wall area of ribbed wall, equivalent area of un-ribbed wall
B	=	bulk temperature curve fit time constant
Bi	=	Biot number
c	=	solid specific heat
c_p	=	constant pressure specific heat
C_f	=	skin friction coefficient
D	=	diameter
D_h	=	hydraulic diameter
e	=	roughness, rib height
f	=	Darcy friction factor
f_0	=	baseline friction factor
h	=	surface heat transfer coefficient
h_s	=	heat transfer coefficient based on convective area
h_p	=	heat transfer coefficient based on projected area
H	=	Channel height
L	=	periodic length

L_{cr}	=	critical length
k	=	turbulent kinetic energy
k	=	thermal conductivity
k_f	=	fluid thermal conductivity
$\dot{m}$	=	mass flow rate
Nu	=	Nusselt number
Nu_0	=	baseline Nusselt number
q”	=	wall normal heat flux
Q	=	total heat addition
P	=	Rib pitch
P	=	wetted perimeter
P	=	static pressure
Pr	=	Prandtl number
r	=	position
Re	=	Reynolds number
s	=	entropy
t	=	time
T	=	temperature
T_f	=	Film temperature
T_f	=	final temperature
T_1	=	compressor inlet temperature
T_2	=	compressor exit, combustor inlet temperature
T_3	=	turbine inlet temperature
T_4	=	turbine exit temperature

T_b = bulk temperature

T_w = wall temperature

T_i = initial temperature

u = streamwise velocity component

u = fluid velocity

u^+ = non-dimensional velocity

u_τ = friction velocity

U = bulk streamwise velocity

V = normal velocity component

V = volume

w = rib width

w = spanwise velocity component

W = Channel width

W_p = Pumping power

x = depth into solid substrate

X = streamwise coordinate

y^+ = non-dimensional wall distance

Y = normal coordinate

Z = spanwise coordinate

Greek Symbols

α = thermal diffusivity

β = linear pressure coefficient

δ = Kronecker delta

Δ	=	difference
ϵ	=	turbulent dissipation rate
η	=	thermal efficiency
θ	=	temperature
κ	=	von Karman constant
μ	=	dynamic, absolute viscosity
μ_t	=	turbulent viscosity
ν	=	kinematic viscosity, momentum diffusivity
ρ	=	density
σ	=	periodic temperature gradient
τ	=	shear stress
τ	=	dummy integration variable
τ_w	=	wall shear stress

Subscripts

$_0$	=	baseline
$_b$	=	bulk
$_{cr}$	=	critical
$_{cu}$	=	copper
$_i$	=	initial
$_f$	=	film
$_f$	=	final
$_p$	=	pumping

$_{p}$	=	projected
$_{sw}$	=	smooth wall
$_{t}$	=	apparent, turbulent
$_{\tau}$	=	friction
$_{w}$	=	wall

Superscripts

$\bar{}$	=	Averaged
$'$	=	Instantaneous
$^{+}$	=	non-dimensional, inner coordinate
$\sim$	=	Periodic
$\rightarrow$	=	vector

Abbreviations

AR	=	Aspect ratio
CAR	=	Channel aspect ratio (W/H)
CCD	=	Charge-coupled Device
CFD	=	Computational fluid dynamics
DNS	=	Direct Numerical Simulation
FD	=	Fully Developed
LED	=	Light-emitting diode
LES	=	Large Eddy Simulation
RANS	=	Reynolds-averaged Navier-Stokes
RAR	=	Rib Aspect ratio (w/e)

RSM = Reynolds Stress Modeling

SW = Smooth Wall

TLC = thermochromic, thermochromatic liquid crystal

INTRODUCTION

In order to interact with the environment that we inhabit, various machines are typically employed to convert energy from one form to another and perhaps in the process also produce some usable amount of work. If the work produced is mechanical, the device is referred to as an engine such as those used in automobiles and airplanes. Depending on the particular need, the definition of useful work can be different for different machines. These machines, in obeying the operating principles dictated by the laws of physics, are limited in the manner in which they can operate.

The desire for a sustainable energy society has spawned a number of technological issues that are challenging today's engineers. These issues and developments include: the introduction of renewable energy sources; increasing efficiency in energy production, use, storage, and transportation; as well a reduction of emissions of greenhouse gases and the development of carbon capture and storage technologies.

Although the ideal efficiency and performance of any energy systems can be described by an overall thermodynamic analysis, there will always exist irreversible losses (production of entropy) in the system associated with the diffusion and transport various potentials such as temperature differences, species concentration, and possibly electrochemical potentials. To enhance, reduce, and suppress these irreversible losses can potentially lead to enormous benefits for the human society. In particular, the enhancement of the heat transfer in heat exchangers and components used in power production plants can have a tremendous impact on energy production, the environment, as well as the world economy.

The interfaces, where the previously mentioned transport processes occur, play a central role in determining the efficiency of the device, equipment, and plant used and will be crucial in shaping the future technology used in energy production, utilization, and storage. The turbulent convective heat transfer occurring at the interfaces is the focus of the current study, as it is applicable to a wider range of applications involving the transport of heat than laminar flows and also because of the inherent difficulty in controlling turbulence.

Turbomachinery

Turbomachineries in some shape or form are responsible for virtually all of commercial power and electricity production in the United States and as well as commercial and military air transport. The main turbomachines employed in electricity production are typically the turbine, where fuel is burned to produce the mechanical work to run a generator, which in turns converts the mechanical work into electricity. For aviation, gas turbine engines are used to produce thrust. Because of their widespread use, even the slightest improvement in the operating efficiency of these devices can have enormous benefits, such as a reduction of the current greenhouse gas emissions and reduced energy prices.

The Gas Turbine Engine

Gas turbines are the workhorse for propulsion and power systems. Gas turbine engines can be grouped into three categories based on their application: 1) aircraft engine turbines, 2) power generation turbines, and 3) marine turbines and industrial turbines. The third category includes gas turbines that are usually derived from the first air-based group but modified and

adapted for land-use to suit their specific purpose. Marine turbines are typically aero-derivatives in a shipboard package. Figure 1 is a schematic of a simple Brayton cycle.

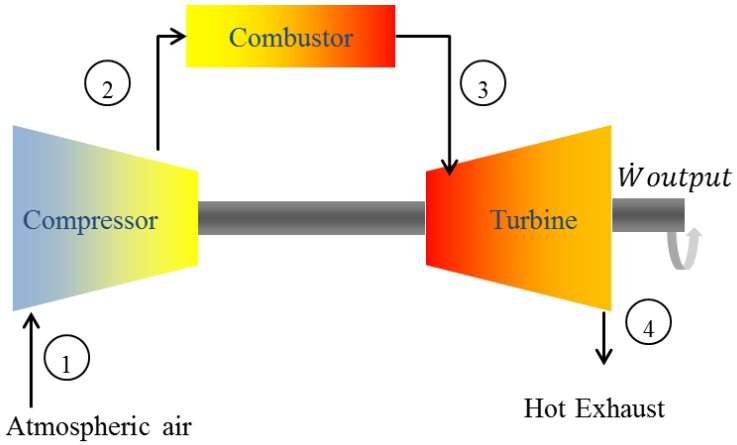

Figure 1: Brayton cycle schematic

The simple Brayton cycle efficiency can be expressed as (1):

$$\eta = 1 - \frac{T_4 - T_1}{T_3 - T_2} \qquad (1)$$

It is desirable to push the cycle efficiency of the gas turbine as high as possible. One method to achieve this is to increase the gas temperature at the turbine inlet (T_3). The increase in turbine inlet temperature is limited in practice by the capability of the metal alloys used to make the turbine components (combustion liners, vanes, and blades). The component operating temperature must be maintained well below the material melting temperature. Gas temperatures throughout the turbine are also restricted in order to reduce NO_x emissions to comply with local regulatory standards.

Figure 2 describes the historical advances in the increase in turbine inlet temperatures made possible by the introduction of various cooling technologies. The turbine inlet temperature employed in modern gas turbine engines is well above the allowable material temperature. The higher than allowable gas temperature is only possible through a number advanced cooling schemes used to cool the components and maintain their part temperature below the allowable temperature. Advancements in materials have led to an increase in the allowable metal temperature, allowing for an increase in the turbine entry temperature. However, advances in cooling technology were responsible for the most significant increases in the turbine entry temperature.

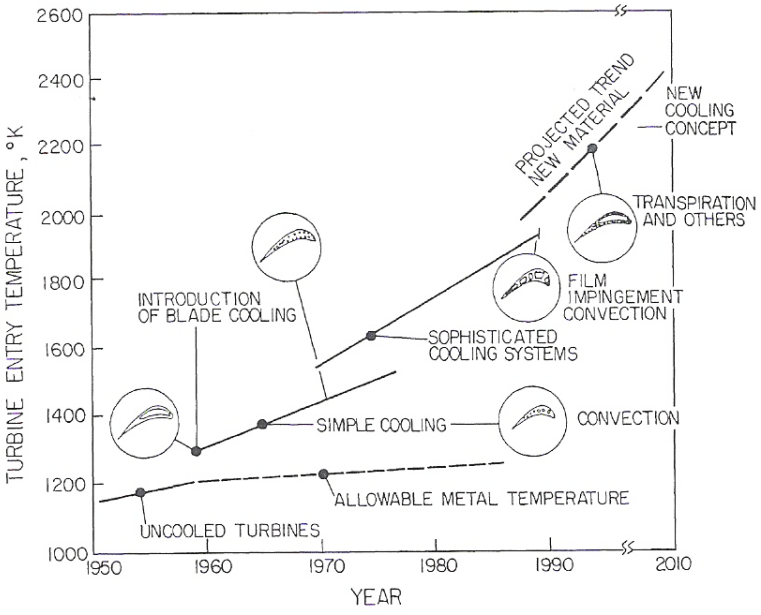

Figure 2: Advances in turbine entry temperature from new cooling schemes (Lakshminarayana, 1996)

Because the turbine inlet temperature is directly related to the overall cycle efficiency of the gas turbine engine, the actual turbine inlet temperature attainable in an operating engine is a

considered a technological standard for the engine. Engines operating at a higher turbine inlet temperature are considered to be more advanced. The turbine inlet temperature in the near future is expected to be as high as 1700 ℃ for power generation turbines and 1900 ℃ for advanced military engines (Chyu M. K., 2010). Current gas turbine engine technology is so advanced that today's engines are approaching the stoichiometric limit of the chemistry involved.

One of the parts in the gas turbine engine that needs considerable attention is the gas turbine blade. Figure 3 depicts a turbine lade for aero-type engines; the three major cooling regimes are all labeled on the figure. Serpentine channels, often lined with rib and also pin-fin turbulators, are run through the interior of the turbine blade. Coolant bled from the compressor stage passes through the internal passages of the turbine and cools the inner surface. Impingement cooling is also sometimes employed, near the leading edge to remove a large amount of heat closer to its source. The coolant is then bled from the internal passages through discrete holes on the blade surface. The coolant exiting the blade through these film cooling holes forms a protective blanket over the surface and effectively shields the blade surface from the high temperature gas.

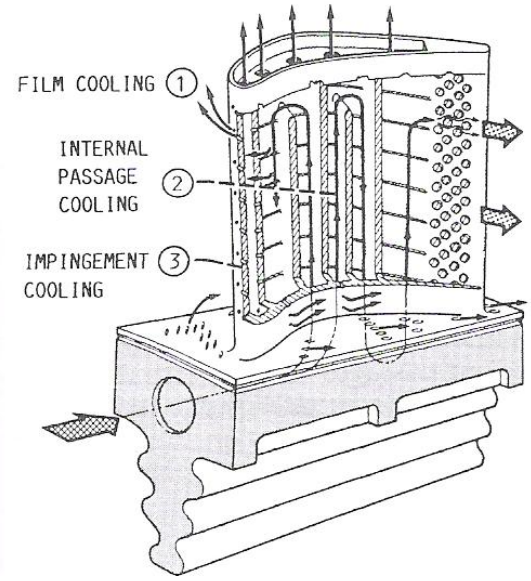

Figure 3: Typical cooled aircraft turbine blade (Gladden & Simoneau, 1989)

Generators

Although the components of the generators employed in electricity production are not exposed to the high temperature environment found in gas turbine engines, the cooling of the generator rotor and stators in land-based power generation equipment is no less a daunting task. Despite the high efficiency of modern generators, which can exceed 98%, an enormous amount of heat must be removed from the generator. One of the mechanisms through which the heat is generated is through Joule heating because of resistance of the conductors used in the generator windings.

The three main components that need cooling are the stator core, stator winding, and rotor winding. The windings in the generator must be maintained below a certain temperature at all times in order to not burn the insulation and cause a short in the generator circuit. When air

cooling is insufficient, hydrogen gas is used as the working fluid because of the lower viscosity and also because of the better thermal transport properties of hydrogen as compared to air. A cross section of a three hydrogen-cooled turbogenerator rotor concepts is given in Figure 4. All three cooling concepts require a fairly complicated manufacturing process and also a necessity to build the generators as pressure vessels to contain the hydrogen gas and also the need for external systems to supply and control the hydrogen.

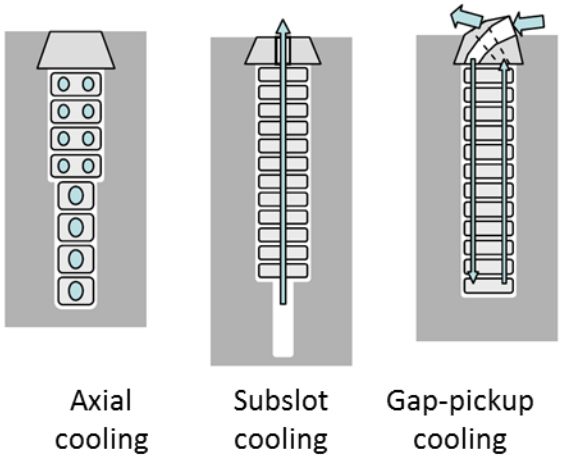

Figure 4: Cross section of hydrogen-cooled turbogenerator rotor slots (Eriksson, 2007)

For more demanding cooling requirements, water cooling may be used. Water has a much greater heat capacity and density than air and hydrogen and can remove much more heat for the same volumetric flow rate. Water cooling allows for the generator to be much lighter and more compact, and potentially more cost effective from the better cooling. The drawback of water cooling is the complication of circulating water through the windings and other parts of the generator. The aerodynamic losses of water in the rotor would lead to considerable pumping requirements. Water cooling is often employed only when necessary, for very large machines,

and is used typically only for the non-rotating stator components with hydrogen cooling used in the rotating parts.

Generators employing both water-cooled stators and rotors are scarce, the Swedish manufacturing company Asea produces and operates a number of units of this class (Eriksson, 2007). A major road block to the use of water-cooled rotors in the next generation of power generation equipment by the leading manufacturers is the cost needed to develop the new technology and obtain an operating record to demonstrate its reliability and robustness. Asea, in the early 1960s decided to avoid hydrogen cooling and chose to develop completely water-cooled machines and thereby was able to skip the hydrogen cooling phase of development.

Because of the already high efficiency of the state-of-the-art generators, a further increase in efficiency is not only difficult and costly to develop but also would not lead to as much benefit as an increase in efficiency in other components in the power plant. Hence, the research and development of more optimum cooling channel designs for use in generator rotor and stator cooling has not received as much attention as in gas turbine cooling. However, the operation of the generator to produce electricity and the generator cooling challenge are no less vital to the overall plant performance and will likely be considered for as long as a device is necessary to turn mechanical work into electricity.

More Heat, Less Friction

Improvements in cooling technology can have direct benefits for both the gas turbine engine and the generator. In principle, introducing a new cooling scheme that transfers more heat

with less pumping power required should increase the overall efficiency of the device. The maximum generator size is often limited by the total cooling available.

It is known that the momentum transport and heat transport are proportional in most engineering flows, a behavior well-known to fluids engineers as the Reynolds analogy. With increasing heat transfer in the flow, more momentum transfer also occurs. The heat transfer process being the transport of heat away from the wall, and the momentum transport process corresponding to the effect of wall friction and shear stress in slowing the fluid which must be overcome by the work used to drive the fluid flow. The Reynolds analogy implies that the occurrence of more heat transfer also implies more friction.

Although the Reynolds analogy is strictly applicable to pipes and flow over flat plats, its implications are nonetheless applicable to other flows, at least qualitatively. It is important to note that more complicated analogies of heat, mass, and momentum have been derived for other flow configurations, such as the Chilton-Colbourn analogy.

In general, the heat transfer enhancement of fluid flow in pipes involves complicated geometrical configurations. However, the analogy can always be made by considering the canonical configuration, the fluid flow and heat transfer in a straight smooth pipe. The essential aspects of heat transfer are all present in this configuration. A certain pumping power is necessary to drive the fluid flow in the pipe in order to oppose the friction in the pipe, which manifests itself as a shear stress to the fluid near the walls of the pipe. For fully developed flow, the pumping power is exactly the product of the channel pressure drop and the volumetric flow rate of the fluid. Hence, in fully developed flows, the pumping power is converted entirely,

directly, and irreversibly into heat through viscous dissipation. This thermodynamic process therefore has an unavoidable entropy generation associated with it and can be written as:

$$\Delta s = \Delta s_f + \Delta s_h = \frac{W_p}{T_f} + q" \left(\frac{1}{T_f} - \frac{1}{T_w} \right) = \frac{\tau_w U_b}{T_f} + \frac{h(T_w - T_f)^2}{T_f T_w} \quad (2)$$

where U is the bulk mean velocity, h is the heat transfer coefficient based on the temperature difference between the wall and the fluid, $\Delta T = T_w - T_f$. A detailed discussion of the use of Equation (2) and its consequences can be found in works by Adrian Bejan (Bejan, 1978) or his textbook on Advanced Engineering Thermodynamics (Bejan, 2006). For fully developed flows, the pumping power is the product of the channel pressure drop and the volumetric flow rate of the fluid. Equation (2) suggests that the ultimate heat transfer technology is to achieve either complete thermal insulation or infinite heat transfer rate, while minimizing losses caused by friction. The frictional losses also need to be reduced to minimize the work required to drive the flow, since the pumping power is always irreversibly dissipated into heat.

The fundamental question remains as to whether the heat transfer can be further enhanced while reducing the pumping power. The Reynolds analogy claims that the heat, mass, and momentum transport processes are mathematically the same and seems to suggest that more friction is expected if more heat transfer is to occur whereas Eq. (2) demands that a search be made for a channel that can promote more heat transfer but without added friction in order to minimize the irreversible losses. The answer is non-trivial but is of profound influence to further advancements in cooling technology. The difference in how the local turbulent transport of momentum and that of heat contribute to the friction and heat transfer coefficients is a key to the answer of whether the dissimilar control is possible.

Recent progress in analyzing turbulence mechanics and designing turbulence control offers a chance to develop a scheme for dissimilar momentum and heat transport, how to obtain more heat transfer with less friction. A detailed discussion of recent progress in methods of turbulent flow control is given by Kasagi et al., where the mathematical formulations of the contribution of turbulent transport to wall friction and heat transfer is discussed (Kasagi, Hasegawa, Fukagata, & Iwamoto, 2010). By reexamining the governing equations and boundary conditions for convective heat transfer, the possibility of achieving dissimilar control in turbulent flow is revived. The Reynolds analogy and such equivalent analogies fail to acknowledge an inherent difference in the fact that velocity is divergence free whereas temperature is a conservative scalar. By exploiting the inherent difference, the dissimilar control can be achieved even in flows where the averaged momentum and heat transport equations have the same form (Kasagi, Hasegawa, Fukagata, & Iwamoto, 2010).

Internal Cooling

Optimization of internal cooling channels has been the subject of a great deal of study in past years for thermal management of hot-gas-path-components in turbomachines. To improve the efficiency of these cooling channels, one must optimize the various aspects of the channel to remove the maximum amount of heat for a given amount of coolant. A variety of techniques are employed to accomplish this task. The most common method is to apply some form of transport enhancing geometry to the walls of the channel which acts to increase secondary flows and turbulence within the channel resulting in improved mixing and more effective heat transfer. These geometries break up the viscous sublayer and, in some cases, promote the formation of vortices and improve the advection of heat from the hot surfaces. The penalty for the addition of

these geometries is usually an increase in pressure drop over the length of the channel. Different components are designed with different cooling schemes based on the specific design requirements. For example, dimples are typically applied in areas where a low pressure drop is desired to allow more favorable pressure margins for other regions of the cooling design because of their notably low pressure drop characteristics. Therefore it is important to find a configuration that provides the best balance between heat transfer and friction augmentation for the specific channel configuration. For this reason, wall surface geometries found in literature are vast and diverse in nature; including dimples, pin fins, ribs, and numerous derivatives of these designs.

These surface enhancements improve the heat transfer capabilities of the cooling channels by two mechanisms. The first is through an increase in the available surface area through which the heat transfer takes place; under similar flow conditions, an increase in the available area for heat exchange is directly proportional to the heat. The other mechanism is by changing the flow field in such a way as to improve the mixing of the fluid in the channel and convection of heat away from the channel walls. Large surface features can potentially influence the bulk flow in the channel and promote better mixing in the bulk flow, and mix the relatively colder fluid near the center of the channel with the relatively hot fluid closer to the channel walls. Smaller surface features, that might not influence the bulk flow, can trip the boundary layer, disrupting the viscous sublayer near the channel walls, which is occupied by slow moving fluid, and to bring the colder fluid from the mainstream directly into contact with the hot walls of the cooling channel. A number of cooling channel geometries has been investigated by utilizing one or more of these phenomena.

Ribs are positive features that act to trip the flow, disrupting the viscous sub-layer formation and causing the formation of complex vortices. Ribs cause separation and reattachment as well as induce secondary flows depending on their size, configuration, and alignment. The increased turbulence leads to a greater mixing of the flow and improvement in the advection of heat away from the channel walls. Typically, rib turbulators are rectangular in cross-section. Many other parameters such as rib aspect ratio, channel blockage ratio, rib orientation to the flow direction, and rib spacing (pitch) can be varied such that an optimal design is achieved. A great deal of studies has been devoted to the application of these features to internal cooling channel designs, for gas turbine vanes and blades.

Rib-Shaped Turbulators

One of the earliest studies of the application of rib turbulators to channel walls was performed on single-pass, stationary channels. Han et al. studied the effects of rib orientation, rib shape, and rib pitch-to-rib-height ratio (P/e) on the overall heat transfer performance of the channel (Han, Glicksman, & Rohsenow, 1978). This study concluded that for the same pumping power, ribs with a 45° orientation with respect to the flow yield better results than those oriented perpendicular to flow direction. Han also studied the heat transfer and friction in channels with two opposite rib roughened walls and developed a method for predicting the heat transfer and friction in channels with ribs on two opposite walls using correlations for four-sided smooth channel and similar laws for four-sided ribbed channels (Han J.-C. , 1984).

Han et al. investigated the effects of channel aspect ratio on the heat transfer characteristics of the channel with angled ribs (Han, Park, & Lei, 1985). It was concluded that

the cooling channels perform best with a channel aspect ratio of ` and a rib-orientation angle in the range of 30-45°. It was also found that the same range of angles is also optimal for rectangular channels; and square channels surpassed rectangular channels in overall performance.

Han et al. provided Nusselt number augmentation and friction factor augmentation data for wedge-shaped and delta-shaped transport promoters in a square channel (Han, Huang, & Lee, 1993). The authors compared the performance of broken-wedge and delta configurations to the full-length configurations. It was found that the broken arrangements perform better than the full-length case. Chandra et al. studied the heat transfer and friction in a rectangular channel with transverse ribs on one, two, and four walls and was the first study performed on the application of ribs to four channel walls (Chandra, Niland, & Han, 1997). Taslim et al. studied twelve different rib geometries, with square as well as trapezoidal cross-section, applied to all four walls of a channel (Taslim, Li, & Spring, 1998). This work characterized the heat transfer and flow characteristics of each geometry. Casarsa et al. characterized the hydrodynamic and heat transfer performance of square ribs oriented perpendicular to the flow in a rectangular cooling channel (Casarsa, Cakan, & Arts, 2002). The ribs studied were comparatively very large, creating a 30% blockage ratio. Reported results included time-averaged distributions of mean velocity components, and Nusselt number values.

Mahmood et al. presented spatially resolved Nusselt numbers and friction factors for a channel with an aspect ratio of four and 45° angled ribs (Mahmood, Ligrani, & Won, 2002). The ribs were arranged such that they were oriented perpendicular to each other on opposite walls.

The rib-height to hydraulic diameter was 0.078, rib pitch-to-height was 10, and blockage ratio is 25%. This work concluded that the highest spatially resolved Nusselt numbers are present on the top surface of the rib with the lowest values being found on the flat surfaces in between the ribs where flow separation and shear layer reattachment have a pronounced effect. Ribs oriented at 45° were also studied by Wang et al. (Wang, Ireland, Kohler, & Chew, 1998). Cho et al. investigated a combination of continuous and discrete, parallel and cross arrays of ribs in a single pass square channel (Cho, Lee, & Wu, 2001).

Because the driving force behind these advancements has been the gas turbine industry, these studies have been primarily limited to channel aspect ratios of one to four, which represent those found in the gas turbine engine. Although high aspect ratio channels (CAR > 8) and high aspect ratio ribs (RAR > 1) do exist in industrial applications, the literature on their performance is found to be quite limited. With industrial applications such as heat exchangers, modern power generators, and electronics cooling, high aspect ratio channel and rib performance is an important characteristic in need of development.

Some previous works in high aspect ratio cooling channels include Bunker et al., Zhang et al., and Sparrow and Cur. In these studies, the channel aspect ratios are kept at 14:1, 10:1, and 18:1, respectively. Bunker et al. tested a channel that combined the trailing edge and the adjacent rib channel of an aero engine airfoil (Bunker, Wetzel, & Rigby, 2002). Zhang et al. utilized ribbed and grooved walls on the same surface in search for the optimum thermal performance (Zhang, Gu, & Han, 1994). Sparrow and Cur used mass transfer to study smooth rectangular channels and the effect of symmetric heating versus asymmetric heating (Sparrow & Cur, 1982).

They reported that heat transfer augmentation between both conditions deviates less than seven percent in the fully developed portion of the channel.

Liu et al. applied 45˚ rib turbulators to two sides of a two-pass channel in a rotating rig. The rib pitch was varied to obtain rib pitch-to-height (P/e) ratios of 10, 7.5, 5, and 3 (Liu, Wright, Fu, & Han, 2006). The rib cross section was square. The rib with the closest rib spacing of P/e = 3 had the best performance in both rotating and nonrotating channels. The rib layouts studied by Liu et al. are shown in Figure 5.

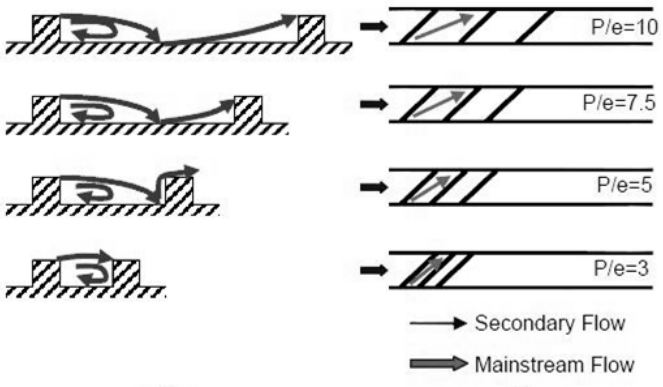

Figure 5: Rib spacing effect studied by (Liu, Wright, Fu, & Han, 2006)

Because of the secondary flows induced by the skewed ribs, as the number of ribs increased and the rib spacing decreased, the strength of the secondary flows also increased and resulted in a continued increased in heat transfer enhancement. This increase in heat transfer is not expected to occur for channels with orthogonal ribs, where the flow is trapped between the ribs and is not forced to circulate by the secondary flows. In their argument of the increased heat transfer with decreasing rib pitch, Liu et al. based used the heat transfer enhancement of their

ribbed channel based on the projected smooth channel area. However, in increasing the number of ribs in the channel with decreasing rib spacing, the total surface area of the channel also increased. When taking into account the additional surface area with the addition of ribs, the heat transfer enhancement with decreasing rib pitch was eliminated. The friction results also indicated that the channel friction increased with decreasing rib pitch until 5. Less than 5, the friction factor decreased.

A number of studies have considered the effect of rib spacing but predominately for square ribs. Few studies have varied the rib width systematically. Wright & Gohardani studied the thermal performance (heat transfer and friction) of rib turbulators in a 3:1 aspect ratio rectangular channel at a channel Reynolds number range of 10,000–70,000 . (Wright & Gohardani, 2008). The ribs studied were oriented 45° to the mainstream flow. Ribs were placed only on the two wide walls. Wright & Gohardani considered rib aspect ratios of 1,2,3, and 4 as well as the distance between ribs in order to investigate the combined effect of rib width and rib spacing on the thermal performance of the channel. The rib aspect ratio was varied by changing the rib width (w) while keeping the rib height (e) constant. The rib configurations studied by Wright & Gohardani are shown in Figure 6. Results from the study by Wright & Gohardani indicate that heat transfer enhancement decreases as the rib width increases and also decreases when the rib spacing increases; increasing the rib width is only effective in increasing the thermal performance of the passage if the rib width and spacing are varied in conjunction with one another.

More complicated rib configurations have also been studied. Kuntsmann et al. studied the performance of W-shaped, 2W-shaped and 4W-shaped ribs in a rectangular channel for channel aspect ratios of 2:1, 4:1 and 8:1 (Kunstmann, von Wolfersdorf, & Ruedel, 2009). The Reynolds numbers were considerably high (Re > 90000). Heat transfer measurements were conducted with the transient TLC technique. The results from this study found that with increasing order of the W-shape (W, 2W, 4W) the number of pairs of counter rotating vortices also increased. The W-shaped ribs produce two counter rotating vortices in each channel half. The 2W-shaped ribs produced four counter rotating vortices and 4W-shaped ribs produced eight counter rotating vortices.

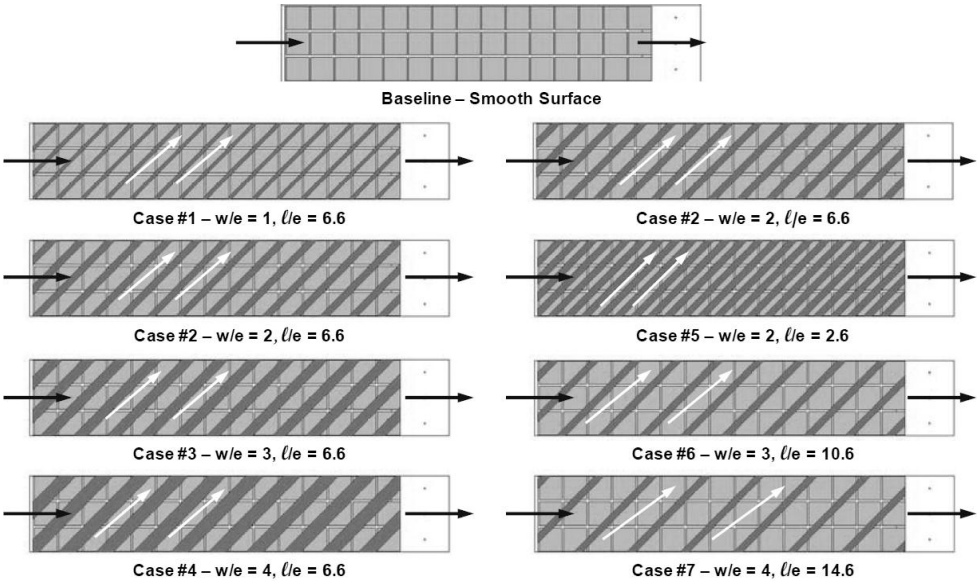

Figure 6: Angled rib configurations studied by (Wright & Gohardani, 2008)

Using a segmented copper block test section, Wright & Gohardani were only able to obtain pseudo-local data at different locations in the channel. With the limited results available

from the spatial distribution of heat transfer, well-supported conclusions for the reasons for the differences in heat transfer observed could not be made. Better spatially resolved measurements of the local heat transfer are necessary to support or refute the findings Wright & Gohardani. In addition, the ribs were width was varied in only one configuration at 45° to the mainstream flow and only for a 3:1 aspect ratio channel, additional studies of other rib configurations and channel configurations are necessary before the effect of varying the rib width can be truly understood. The current work attempts to overcome some of these shortcomings in past studies in order to provide further insight into the flow changes with varying the rib width.

The previous studies mentioned made use of altering the spacing between two consecutive ribs. In some cooling applications, such as in generator rotor cooling, the spacing between any two consecutive features is fixed. To reduce the cost of manufacturing the cooling channels in the rotors, each of the straps that form the generator rotor typically has identical features applied. The drawback of the reduced manufacturing cost and complexity is that the relative locations of each feature are also the same for each strap. Hence, the varying rib pitch or spacing between ribs is sometimes not permitted for rotor cooling applications. Other means of varying the rib shape and parameters must be used that does not require varying the parameters that are fixed by the rotor configuration. This example demonstrates that an optimum cooling channel design cannot be achieved from just considering the thermal performance characteristics. In practice, manufacturing capabilities and cost considerations also play an important role. The effects of spatially non-uniform cooling are also important in considering the thermal stresses induced by the non-uniform cooling which can lead to component failure. A specific cooling arrangement with a higher rate of heat transfer and a greater degree of non-uniformity in the

cooling can actually lead to component failure and would be less desirable than the setup that, while it may transport less heat and provide less cooling, is guaranteed to at least perform its duty. A non-functional device serves no purpose, whereas even a poorly performing device has some utility.

The optimization of a cooling channel design or to progress towards an ideal cooling requires much more than just the thermo-aero-mechanical considerations; in practice it is a multidisciplinary study where economic considerations also come into play, and possibly even aesthetics.

A building block approach to turbine aerothermal research is shown in Figure 7. Both experimental and analytical (or numerical) techniques are often used in conjunction with one another in order to reduce the total time of development.

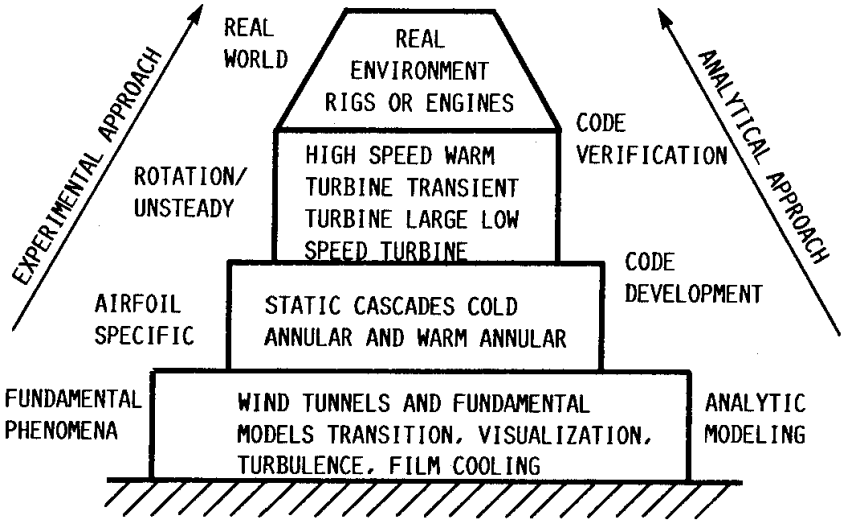

Figure 7: Building block approach to turbine aerothermal research (Gladden & Simoneau, 1989)

At the lowest level of development, the fundamental and basic phenomena occurring are the primary interest. Testing is performed on very basic configurations or specific sections of interest in a simplified and well controlled environment. The experiments are designed to assess the strength of certain phenomena, and analytical and numerical approaches are designed in order accurately model or reproduce the same phenomena. For experimental testing of cooling channel performance, the performance tests are done on channels that may not be entirely representative of the actual implementation in the final product. Straight rectangular channels may be used to mimic the actual channels in the gas turbine blade. These channels may be tested on stationary experimental setups without any rotation, scaled-up in dimensions in order to improve the experimental accuracy of the results, use different materials (such as copper) for the cooling channel walls to reduce experimental uncertainties. Similarly, the analytical approach will attempt to model the most fundamental features. At progressively higher levels of development, the testing is performed in more realistic environments to take into account more effects that might be expected or experienced by the part in operation until the actual engine environment or actual engine performance is tested at the highest level.

The building block approach is not strictly linear. Development of a component can start at any level and need not progress strictly upward to higher levels. Past experience can allow for many of the lowest levels to be skipped if only minor changes are made. Drastic changes to the engine design however, may require a complete ground-up development process. Likewise, newer issues encountered at higher levels of development or that was not expected beforehand might call for a recess to a lower level of development to retest or improve the understanding of the basic phenomena.

Overview of Present Work

The current study employs both experimental and numerical techniques to investigate the heat transfer and friction performance of ribs of different aspect ratios in a 2:1 aspect ratio channel. The experimental study uses the transient TLC technique to determine the local distribution of the surface heat transfer coefficient. The same wind tunnel is also instrumented with wall static pressure taps to measure the wall static pressure distribution throughout each of the channels, enabling the determination of the channel pressure drop, friction factor, and friction factor augmentation. A detailed knowledge of both the heat transfer and friction characteristics of the channels is necessary in order to understand the overall thermal performance of the ribbed channels.

The generation of the topology and mesh for the computational study is done using the commercial grid generation software GridPro (Program Development Company). The numerical solver used is the commercially available software Fluent (Ansys, Inc). Additional post-processing of both experimental and computational results and figures are created using the commercial software Tecplot 360 (Tecplot, Inc). The experimental techniques are employed to obtain robust and accurate measurements of the ribbed channel heat transfer and pressure characteristics. The computational study is performed to provide further insight into the flow physics and support some of the trends obtained with the experimental data. In addition to the insight into the flow physics offered by the computational study, the accuracy of the behavior of the cooling channels predicted by the numerical technique is of great interest to both members of academia and industry.

Rib Configurations

A schematic of the channel cross section used in the experiments is given in Figure 8, the channel width (W) and channel height (H) are labeled on the figure.

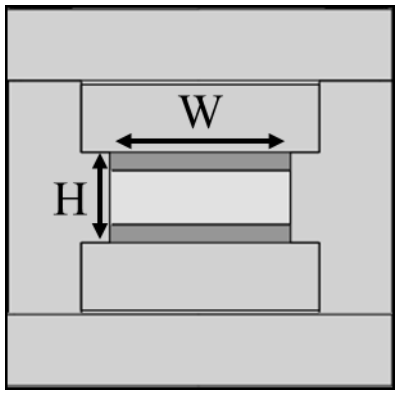

Figure 8: Channel cross section

Figure 9 explains the relevant rib parameters. The rib or roughness height, *e*, the rib pitch, *P*, and rib width, *w*, are labeled in the figure.

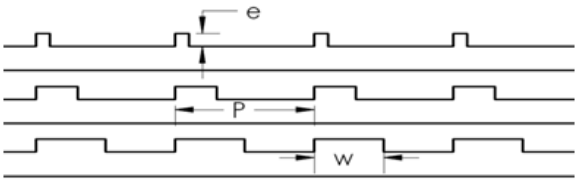

Figure 9: Rib nomenclature

Ribs are applied to only the top and bottom walls in the current study (the two opposite wide walls). The ribs on opposite wall are aligned (un-staggered) with respect to one another and oriented perpendicular or orthogonal to the main flow direction. This configuration leads to a

double symmetric expansion after each rib pair. Figure 10 is a view of each of the rib configurations from the side wall angle. Table 1 contains the relevant rib parameters used in the current study for each case.

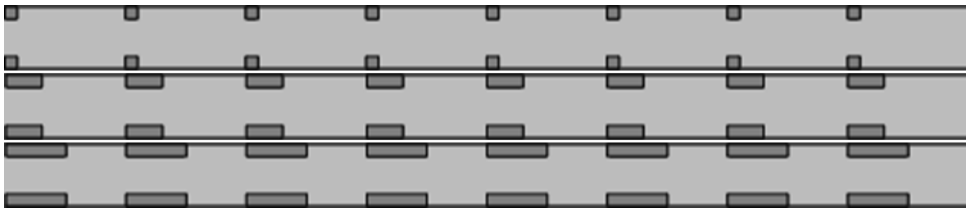

Figure 10: Aligned rib configurations, A1 (top), A3 (middle), A5 (bottom)

The ribs are machined out of commercial grade copper. All the ribs have the same height (e=0.125 inches), only their width is changed to obtain different rib aspect ratios. The rib widths (w) are 0.125 in., 0.375 in., and 0.625 in. for cases A1, A3, and A5 respectively. The ribs are 1.26 in. in length so that they span the entire width of the channel. The same rib pitch (P=1.25 in.) is used for all rib cases which results in a constant relative pitch of 10 (P/e = 10).

Table 1: Rib parameters in current study

Case	CAR $\frac{W}{H}$	RAR $\frac{w}{e}$	$\frac{P}{e}$	$\frac{e}{H}$	$\frac{e}{D_h}$
SW	2	-	∞	0	0
A1	2	1	10	0.20	0.15
A3	2	3	10	0.20	0.15
A5	2	5	10	0.20	0.15

Thermochromatic Liquid Crystals

Thermochromatic Liquid Crystals, also known as thermochromic liquid crystals, are color changing crystals whose color depends on temperature. The use of TLC is widespread; a good example is in the medical industry where TLC is commonly employed as a disposable thermometer for accurately measuring the human body temperature. The liquid crystals' ability to modify incident white light is attributable to a combination of certain optical phenomena: birefringence, circular dichroism, and Bragg diffraction. An in-depth explanation of the specific tunable properties of thermochromic liquid crystals can be found in the Handbook of Thermochromic Liquid Crystal Technology (Hallcrest, 1991).

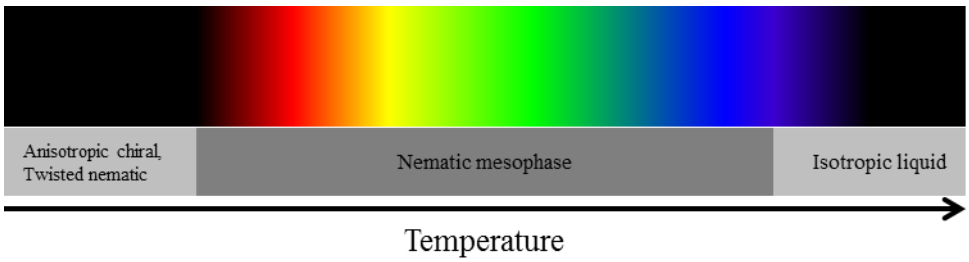

Figure 11: TLC bandwidth and crystallic phases

The color play is the temperature range over which the liquid crystal mixture exhibits changes in temperature. The crystal mixture is colorless below the color play, becomes red when a characteristic temperature is reached (the red start) and then transitions through the entire visible light spectrum until it exceeds the color play bandwidth and turns colorless again. Although often referred to as colorless, the bare TLC mixture color when outside the bandwidth is cloudy and still visible to the naked eye. Typically, the red color appears at the lower operating

temperature and blue or violet appears at the higher operating temperature, although specialized liquid crystal mixtures are capable of the opposite.

A black backing is typically employed to absorb any light not reflected by the liquid crystals, and to also improve the contrast for better discernment of the color under a camera system. The liquid crystal mixture can be systematically varied to change the temperature at which the red or green start appears or to achieve a certain color play bandwidth. A selective reflection of certain wavelengths by the crystal structure of the mixture as it changes crystallic phases can be obtained by tuning the individual components of the liquid crystal mixture. TLC manufacturers can produce mixtures with a bandwidth as low as 1 K and can control the red or green start temperature occurrences to less than 1 K. The sprayable form of TLC based paint is used in the current study.

Computational Fluid Dynamics

A computational fluid dynamics study is performed in conjunction with the experimental study. The commercial software Fluent as implemented in ANSYS, Release 13.0 by ANSYS, Inc. is used as the solver. Fluent utilizes a finite volume method approach by solving the governing equations of fluid flow over discrete control volumes defined by the computational grid or mesh and then iterating the solution repeatedly. In this chapter, the problem of closure in turbulence is introduced in order to establish the background for utilizing turbulence models when attempting to solve the Navier-Stokes equations numerically.

The Problem of Turbulence

The time dependent, incompressible continuity, momentum, and energy equations are given by Eqns. (3), (4), and (5) respectively in Einstein notation. Equation (4) is the Navier-Stokes equation for an incompressible Newtonian fluid:

$$\frac{\partial u_i}{\partial x_i} = 0 \tag{3}$$

$$\frac{\partial u_i}{\partial t} + u_j \frac{\partial u_i}{\partial x_j} + \frac{1}{\rho}\frac{\partial P}{\partial x_i} = \nu \frac{\partial^2 u_i}{\partial x_j \partial x_j} \tag{4}$$

$$\frac{\partial \theta}{\partial t} + u_j \frac{\partial \theta}{\partial x_j} = \alpha \frac{\partial^2 \theta}{\partial x_j \partial x_j} \tag{5}$$

where i = 1, 2, 3, corresponds to x(u), y(v), and z(w) coordinates (velocities) in the three dimensions, respectively. P is the hydrodynamic pressure, ρ is the fluid density, θ is the temperature, α is the thermal diffusivity, and ν is the momentum diffusivity or kinematic viscosity. In principle, Eqns. (3),(4), and (5) can be solved to provide a complete description of any Newtonian fluid flow at all given points in space and time; there are 5 independent equations and 5 unknowns that need to be solved for (pressure, the three velocity components, and temperature). However, a brute force numerical approach (called Direct Numerical Simulation) is not practical for turbulent flows because of the size of the smallest scales of turbulent motions that must be resolved, the dissipative or Kolmogorov scale. Direct Numerical Simulations (DNS) of turbulent flows are currently only feasible for simple flows at low Reynolds number because the decreased in size of the dissipative scale decreases with increasing Reynolds number. For complex flows and high Reynolds numbers, most engineering flows, immense computational resources are necessary to resolve the dissipative eddies. Many advances

will have to be made to current computational technology, equipment, and methods before direct numerical simulations are practical.

An even greater problem is that there is yet to be a guarantee that solutions to the Navier-Stokes equations even exist, or even when they do, that they are bounded. The lack of this basic property is one of the greatest unsolved problems in physics; a proof (or counterproof) for the guaranteed existence of smooth solutions to the Navier-Stokes equations was listed as one of the seven Millennium Prize Problems by the Clay Mathematics Institute in 2000 (Carlson, Jaffe, & Wiles, 2000).

The Reynolds-averaged Navier-Stokes equations

Until the nature of fluid flow and turbulence is better understood, and until direct solutions to the Navier-Stokes equations are practical, engineers must continue to work with other tools that are available. One approach is to instead seek solutions to the simpler mean flow, or time average flow. When Reynolds averaging is used to time average the Navier-Stokes equation, the Reynolds-averaged Navier-Stokes equations (RANS equations) can be arrived at by decomposing the flow into a mean portion and fluctuating portion and then simplifying the resultant equation, Eqn. (6):

$$\rho\overline{u}_j\frac{\partial\overline{u}_i}{\partial x_j}=\frac{\partial}{\partial x_i}\left[-\overline{P}\delta_{ij}+\mu\left(\frac{\partial\overline{u}_i}{\partial x_j}+\frac{\partial\overline{u}_j}{\partial x_i}\right)-\rho\overline{u_i'u_j'}\right] \quad \textbf{(6)}$$

The last terms on the right hand side are called the Reynolds stresses, and assigned their own tensor and symbol, Eqn. (7):

$$\tau_{ij} = \rho\overline{u_i' u_j'} \quad (7)$$

The Reynolds stress captures the contribution exerted onto the mean motion by the turbulent velocity fluctuations. The Reynolds stress tensor has additional properties, it is symmetric. The diagonal terms in the Reynolds stress tensor are the normal stresses and the off-diagonal terms are the shear stresses. In most flows, the off-diagonal shear stress terms dominate the momentum transfer caused by the turbulent motions of the flow. The symmetric property of the Reynolds stress limits the actual independent variables in the Reynolds stress to six terms instead of nine.

Reynolds averaging can also be performed onto the heat diffusion equation, Eqn. (5), to arrive at Eqn. (8) which is the energy equation that must be solved simultaneously with the RANS equations and continuity.

$$u_j \frac{\partial \overline{\theta}}{\partial x_j} = \frac{\partial}{\partial x_i}\left(-\overline{\theta u_j} + \alpha \frac{\partial \overline{\theta}}{\partial x_j}\right) \quad (8)$$

In performing the Reynolds-averaging operation, six additional unknowns were introduced into the governing equations in the form of the Reynolds stresses. The appearance of the Reynolds stress makes the governing equations difficult to solve because the RANS equations are no longer closed, there are more unknowns than there are equations to solve. It is known from experience that turbulent flows do exist, that the governing equations are not inconsistent, and that there must be solutions to them because turbulent flows are also flows. In order for the RANS equations to be solvable, there must be additional relationships that somehow bring closure to the governing equations and relate the six Reynolds stresses (the

turbulent velocity fluctuations) back to the mean flow motions. Unfortunately, all the physical principles (mass conservation, momentum conservation, and energy conservation) have been exhausted and no new equations can be derived. The lack of the needed equations is often called the closure problem of turbulence (Tennekes & Lumley, 1972). So long as a brute force direct numerical simulation is not being performed, and until the nature of turbulence is fully understood, additional turbulence models must be introduced to bring closure to the RANS equations.

Turbulence modeling

The basis of most turbulence models makes use of the Boussinesq hypothesis or approximation, which states that the Reynolds stress is proportional to the mean strain rate tensor by the relation given in (9):

$$\tau_{ij} = \mu_t \left(\frac{\partial \overline{u}_i}{\partial x_j} + \frac{\partial \overline{u}_j}{\partial x_i} \right) - \frac{2}{3} \rho k \delta_{ij} \qquad \textbf{(9)}$$

where μ_t is the eddy viscosity, δ_{ij} is the Kronecker delta, and k is defined as the turbulence kinetic energy, (10):

$$k = \frac{\overline{u_i' u_i'}}{2} \qquad \textbf{(10)}$$

The Boussinesq approximation allows a simplification to be made by treating the effect of turbulence similar to an effect caused by molecular viscosity, hence the name eddy viscosity for μ_t. The Boussinesq approximation is not true for all flows, it holds only for simple flows. Complex flows, such as flows with strong streamline curvature, strong acceleration and deceleration (rapid contraction and expansion) do not satisfy well the Boussinesq approximation.

Models that rely on the Boussinesq approximation therefore have inherent difficulty in correctly predicting flows that do not strictly satisfy the Boussinesq approximation.

The realizable-k-ϵ model

Two equations models are one of the most common types of turbulence models. Models such as the k-ϵ and k-ω models are two popular models that are commonly used to solve engineering flows. The turbulence model used in the numerical portion of the current study is the two equation realizable-*k*-ϵ model, an improvement of the standard-k-ϵ model, developed by Shih et al. (Shih, Liou, Shabbir, Yang, & Zhu, 1995). Two equations because are so-called because they introduce two transport equations to account for the turbulence effects of the flow in order to bring closure to the RANS equations. The first transported variable is the turbulent kinetic energy, *k*. The second transported variable (in the k-ϵ model) is the turbulent dissipation, ϵ. The turbulent dissipation determines the scale of the turbulence motions in the flow whereas the turbulent kinetic energy determines the energy within the turbulence. Details of the implementation of the realizable-k-ϵ model in Fluent can be found in the Fluent Theory Guide as well as supported documentation by ANSYS.

The boundary layer and near-wall treatments

The structure of the turbulent boundary layer contains large gradients of velocity and turbulence characteristics. A sufficiently fine mesh must be used near the gradients in order to accurately account for the changes across cell volumes and not “lose” the property of the flow.

Near-wall treatments and y^+

In the outer layer, the turbulence is rapidly augmented and replenished by the production of turbulent kinetic energy generated by the large velocity gradients. Very close to the wall, viscous damping reduces the tangential velocity fluctuations whereas kinematic blocking limits the normal velocity fluctuations. Most turbulence modeling approaches are primarily valid for the turbulent core of the flow (away from the walls). Additional steps must be taken in order to couple the turbulence models away from the wall to the near wall region dominated by viscous affects. The non-dimensional wall distance y^+ defined in (11) is commonly used to determine the location of the first grid point with respect to the law of the wall. The friction velocity, u_τ, is defined in (12), and can also be considered in non-dimensional form as u^+ in (13):

$$y^+ = \frac{y u_\tau}{\nu} \quad \textbf{(11)}$$

$$u_\tau = \sqrt{\frac{\tau_w}{\rho}} \quad \textbf{(12)}$$

$$u^+ = \frac{u}{u_\tau} \quad \textbf{(13)}$$

The viscosity affected region, or inner layer, of the boundary layer is typically further divided into the three regions, Table 2. In these inner coordinates expressed in terms of y^+, the linear region of the viscous sublayer extends to $0< y^+<5$, the buffer layer occupies $5<y^+<30$, and the logarithmic layer occupies $y^+>30$.

Table 2: Regions within the inner layer

linear sublayer	$y^+<5$
Buffer layer	$5<y^+<30$
log-law region	$y^+>30$

In the log-law region, the non-dimension velocity profile obeys the semi-logarithmic relationship, (14).

$$u^+ = \frac{1}{\kappa}\ln(y^+) + C^+ \quad \textbf{(14)}$$

where κ=0.41 is the dimensionless von Karman constant and C^+ is also a constant (with typically values of approximately 0.50). Very close to the wall, within the linear sublayer, the velocity profile obeys the linear relation:

$$u^+ = y^+ \quad \textbf{(15)}$$

With either approach, a sufficient number of grid points must be available in the near wall region in order to resolve the gradients there. A strategy for dealing with the wall y^+ in wall-bounded flows is described by Salim & Cheah for different approaches (Salim & Cheah, 2009). In determining the quality of the near wall mesh the value of y^+ for the first grid point is a very important parameter since it dictates the wall layer regime of the first gird point. For generated meshes that do not have abrupt changes in cell size away from the walls bounding the domain, the y^+ of the first grid point provides a useful estimate of the grid resolution and quality in the near wall region. However, the actual y^+ value depends on the solution obtained and can only be calculated after the momentum equation has already been solved. Hence it is very important to

check the values of y^+ for all the grid cells near the wall bounded regions in order to verify that the mesh used is adequate for the near wall modeling approach. To accurately predict the grid spacing needed to achieve a certain y^+ criteria is difficult unless the expected friction velocity is already known beforehand. In this study, the channel friction factor obtained from the experiments allowed for an accurate prediction of the wall shear stress, which aided in the calculation of the grid spacing needed to achieve the desired y^+ of less than unity.

Periodic Flows

By taking advantage of the periodic nature of the periodically fully developed flow in the ribbed channel configurations, a significant reduction in the size of the computational domain is achieved. In the computational study performed, the computational domain consists of one rib pitch. The reduction of the computational domain reduces the computational resources that would otherwise be wasted to yield the same results and allows for a more detailed study to be performed on the reduced domain.

One of the necessary conditions for periodic flows is for the each of the velocity components to repeat themselves in space after each period. In general, the periodicity can be complex and can involve a number of rotational and translational periodicity components. In this study, no rotational periodicity is used, only the translational periodicity is applied. The periodicity of the domain is the rib pitch (P). The periodic velocity components are expressed in Eqns. (16),(17), &(18) for an arbitrary position , r, and translational period, L:

$$u(\vec{r}) = u\left(\vec{r} + \vec{L}\right) = u\left(\vec{r} + 2\vec{L}\right) = \cdots \quad \textbf{(16)}$$

$$v(\vec{r}) = v\left(\vec{r} + \vec{L}\right) = v\left(\vec{r} + 2\vec{L}\right) = \cdots \quad \textbf{(17)}$$

$$w(\vec{r}) = w\left(\vec{r} + \vec{L}\right) = w\left(\vec{r} + 2\vec{L}\right) = \cdots \quad \textbf{(18)}$$

Another necessary condition is for the pressure to also be periodic. For viscous flows, the fluid pressure is not periodic in the same sense as the velocity components, since a pressure drop must occur, in the streamwise direction, to overcome the viscous losses in the flow. However, the pressure drop or pressure difference is periodic, Eqn. (19).

$$\Delta p = p(\vec{r}) - p\left(\vec{r} + \vec{L}\right) = p\left(\vec{r} + \vec{L}\right) - p\left(\vec{r} + 2\vec{L}\right) = \cdots \quad \textbf{(19)}$$

For periodically fully developed flows, such as the ribbed configurations in this study, the periodic pressure drop is constant. The local pressure gradient of the fluid flow can then be decomposed into the gradient of a linearly-varying component and the gradient of a periodic component.

$$\nabla p(\vec{r}) = \beta \frac{\vec{L}}{\left|\vec{L}\right|} + \nabla \tilde{p}(\vec{r}) \quad \textbf{(20)}$$

The linear component results in a force acting on the fluid in the momentum equations, much like a body force. The β must be iterated on to satisfy one of the operating conditions defining the flow, either the pressure drop if the pressure drop is already known or to satisfy a user specified mass flow rate condition. The specified mass flow rate constraint is used in this study to control the flow Reynolds number. The value of β is updated during the pressure

correction step of the SIMPLE algorithm used in Fluent based on the difference in the actual and desired mass flow rate of the flow.

For flows with heat transfer, the energy equation must also be solved. The periodic temperature gradient, like the pressure drop, is also constant, Eqn. (21).

$$\frac{T(\vec{r}+\vec{L})-T(\vec{r})}{L}=\frac{T(\vec{r}+2\vec{L})-T(\vec{r}+\vec{L})}{L}=\sigma \qquad \textbf{(21)}$$

The temperature gradient can be written in terms of the total heat addition within the domain, Q, as:

$$\sigma=\frac{T_{b,exit}-T_{b,inlet}}{L}=\frac{Q}{\dot{m}C_pL} \qquad \textbf{(22)}$$

where the total heat rate is known if a uniform specified heat flux condition is used. The specified heat flux approach is used in this study. The value of the heat flux applied used is different for each Reynolds number. The necessary heat flux to obtain a bulk temperature increase of 10 K over the periodic domain is calculated beforehand from the mass flow rate at each channel Reynolds number.

The periodic flow conditions are not easy to manipulate for complicated flow physics. A discussion of their suitability to different flow configurations and their limitations can be found in the Fluent Theory Guide.

EXPERIMENTAL METHOD

In this chapter, the details of the experimental setup used and experimental procedure that was followed are discussed as well as the data reduction process of translating the measured quantities into the sought-after parameters. The calculated experimental uncertainty and resultant data collected is presented at the end of the chapter.

The current work employs the 'hybrid" measurement technique based on transient liquid crystal imaging employed by Chen et al. (Chen, Li, & Chyu, 2006) for measurements of heat transfer over a trailing edge configuration with an internal cooling channel containing an aluminum pedestal array on an acrylic substrate. In the study by Chen et al., the heat transfer coefficient on the sections not covered by pedestals was calculated using the one-dimensional transient model. The heat transfer over the pedestal surface was calculated with the lumped capacitance model.

The hybrid measurement was also later employed by Maurer et al. to study the heat transfer enhancement in a rectangular channel with W-shaped and WW-shaped ribs for the backside cooling of combustor liners (Maurer, Ruedel, Gritsch, & von Wolfersdorf, 2008). Maurer et al. improved on the method by Chen et al. and segmented the copper rib into multiple sections and applied the lumped capacitance model to the individual segments to obtain regional surface heat transfer coefficients. Maurer et al. also studied a configuration of only positive hemispheres with no ribs and used an approximate solution for the 1D heat conduction equation to calculate the heat transfer coefficient on the hemispherical surfaces. Kuntsmann et al. also studied similar rib configurations as Maurer et al; in the study by Kuntsmann et al., W-shaped,

2W-shaped, and 4W-shaped ribs were studied for channel aspect ratios of 2:1, 4:1, and 8:1 (Kunstmann, von Wolfersdorf, & Ruedel, 2009). Maurer et al. and Kuntsmann et al. used aluminum alloy as the rib material.

Experimental Setup

The experimental setup is a further development of a previously used setup. The current test section is entirely new to accommodate the new channel cross section dimensions. However, many elements of the previous setup were incorporated into the design of the new test setup.

The flow path arrangement of the experimental setup is shown in Figure 12. Flow is provided from a 1.5 hp Spencer Vortex® Regenerative Blower operated under suction. The vortex blower is operated under suction so that the air entering the test section can be induced from the ambient surroundings in order to avoid having to use the hot air from the blower exhaust. The use of ambient air at the inlet simplifies the procedure needed to maintain a uniform initial temperature since experimental setup can be allowed to cool in-between tests to room temperature. The ambient room temperature is also controlled by the air conditioning, whereas the temperature of the hot air exiting the blower depends on the work load and is difficult to control.

A gate valve and venturi flow meter (Preso brass series venturi, PVBRCAAA3A) is used to control and measure the flow rate respectively. Ambient air passes through a staged, stainless steel fine-mesh heater module before entering the test section. The heater module is powered by a high current DC power supply which is switched on at the start of the test to provide a change in the flow temperature. T-type thermocouples are distributed throughout the test section in order

to capture the spatial and temporal evolution of the centerline temperature during the test. A thermocouple is placed immediately at the entrance of the test section after the flow exits the mesh heater; additional thermocouples are placed immediately at the start, middle, and end of the TLC coated viewing window. Two more thermocouples are placed further downstream of the test section to monitor the flow temperature.

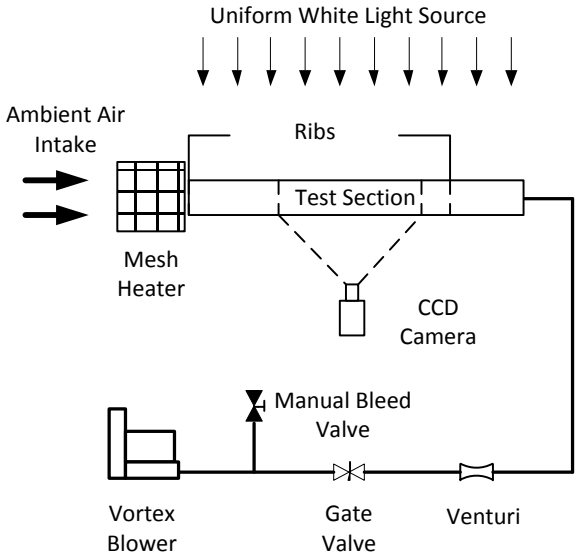

Figure 12: Schematic of Experimental Setup

The acrylic test section has a flow cross section of 0.63 inches by 1.26 inches (16mm by 32 mm), schematic shown in Figure 8 and includes additional details in Figure 13. The test section is constructed from a number of pieces of ½ inch thick acrylic. The total length of each acrylic piece is 40 inches. Two inserts are used for the top and bottom walls that are painted with TLC and applied with ribs. The two inserts are held in place by the assembled configuration of the two side walls and the top and bottom walls that form the housing of the channel. One of the

side walls, denoted in Figure 13 is applied with pressure taps. The pressure taps are distributed throughout the entire 40 inch length of the test section to measure the static pressure distribution throughout, with 8 taps located within the viewing window.

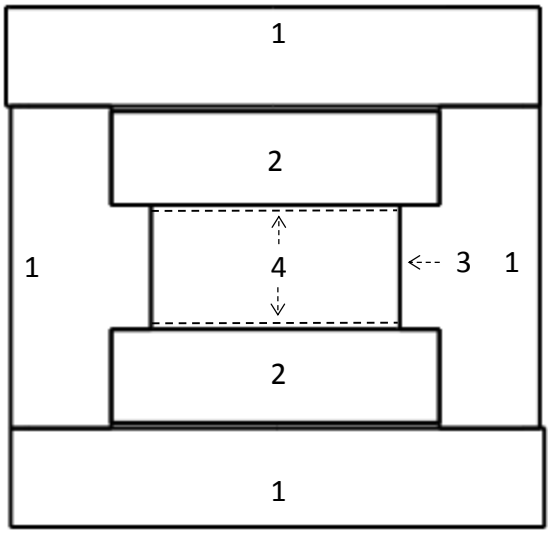

1	Clear Acrylic Housing
2	½" Thick Acrylic Inserts
3	Pressure Tap Location
4	TLC Coat and Backing

Figure 13: Test Section Assembly

Sprayable TLC is used without modification as purchased from LCR Hallcrest (SPN1000G35C1W with a color play bandwidth of 1°C centered at 35°C). The green temperature of this particular batch of liquid crystals was known to occur at 35.1°C from thermal profiles provided by the manufacturer. The TLC is first applied to the acrylic inserts using an air brush and then painted over with a black backing (also from LCR Hallcrest) to improve the color contrast. The TLC is only applied to the 10 inch viewing window, which starts 10 inches from

the exit of the mesh heater, in order to reduce the total amount of TLC used, which is limited to the 500g batch purchased. For a smooth channel, the developing length for turbulent flows is taken to be approximately 10 hydraulic diameters. Since only the heat transfer in the fully developed portion is of interest in this particular study, the developing section was left unpainted. The 10 inch gap between the exit of the mesh heater to the start of the TLC painted window covers a length of approximately 12 hydraulic diameters to allow room for the hydrodynamic boundary layer to become fully developed. For channels with added roughness and features, the additional flow interactions can significantly shorten the length required for the flow to become periodically fully developed. Fully developed in this latter sense does not necessarily refer to the completed growth of the hydrodynamic boundary layer, since the boundary layer can be repeated tripped and disrupted by the added features.

The copper ribs were machined to shape from commercial grade copper. The rib height is equal for each of the rib cases studied (0.125 in). Three sets of ribs were machined, one for each rib case with the proper width to obtain the desired rib aspect ratio and proper length (1.26 in) to span the width of the test section. The ribs are attached on top of the already TLC coated acrylic using 3M 1182 double-sided copper tape; 0.088 mm thickness. Ribs are applied immediately at the inlet of the acrylic test section (just after the exit of the mesh heater box) and cover the 20 inch distance to the end of the viewing window (16 ribs total). This arrangement provides for eight ribs before the viewing window and another eight within the viewing window. The remaining 20 inches of the acrylic section downstream of the viewing window is left smooth. The addition of ribs increased the total surface area of each of the ribbed walls by 20%, shown in

Figure 18. Because the rib pitch is held constant, the ribbed wall surface area is the same for each rib case, with only a reduction on the non-ribbed side wall with increasing rib aspect ratio.

Florescent white-light lamps were installed on the rig frame and behind each camera to achieve a constant and uniform lightning condition for the TLC as shown in Figure 14. The entire frame of the acrylic test section was also covered with a blackout material to block out any ambient lightning.

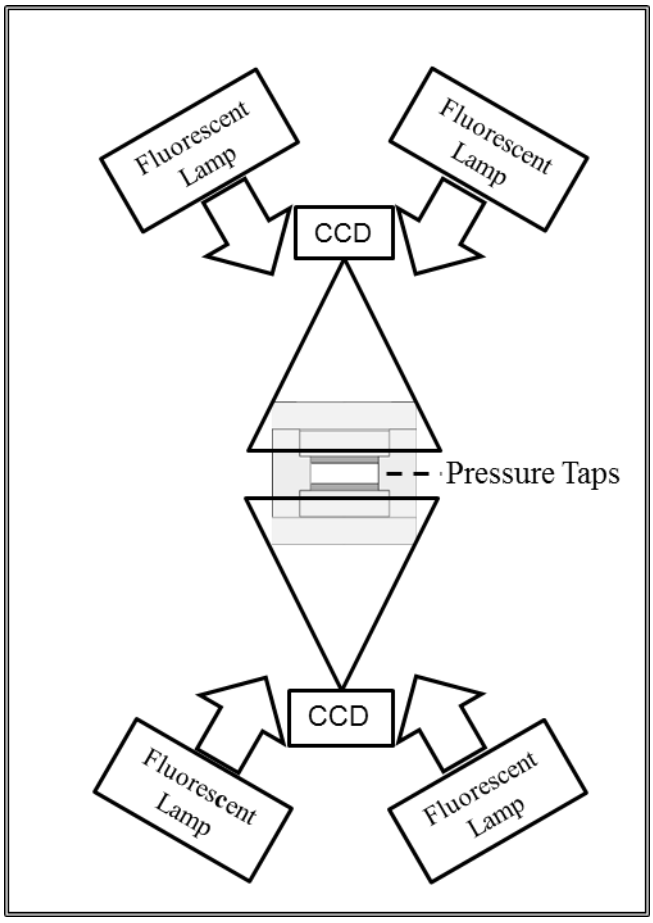

Figure 14: Camera and lighting setup for TLC experiment

Tests are run only with the facility lights turned off. The time history of the visible color change of the TLC coating applied to the channel walls is recorded with two Panasonic NVGS240 3CCD digital-video camcorders with a 720 pixels by 480 pixels resolution and a capture frame rate of 30 frames per second. One camera is mounted over each TLC coated wall, centered over and orthogonal to the viewing window. The camera resolution and test setup used allows for approximately 6 pixels to cover the base of the rib width for case A1. After recording, the images are digitized onto a PC. Once digitized, the images are then post-processed by an in-house MATLAB code. The images are analyzed frame-by-frame to obtain the time history of the recorded RGB intensity values at each individual pixel location. This process generates a time history of the development of the reflected color intensities at each location in the channel. Knowing the corresponding temperature of the TLC with respect to the peak reflected intensity of each color, the time at which the peak reflected intensity occurs can be used to calculate the heat transfer coefficient at each location.

Experimental Procedure

In these sub-sections, the experimental procedure is described for the two separate measurements performed in this study, the friction factor test to measure the overall channel pressure drop and friction and the heat transfer test used measure the local distribution of surface heat transfer coefficients.

Friction Factor Testing

To test the overall channel friction, the flow is first set to the desired Reynolds number in the test section. The pressure differential across the venturi is measured with an HHP-2021

handheld digital manometer, Omega Engineering; the flow rate is controlled by adjusting the gate valve until the desired flow rate is obtained. Static pressure measurements are taken using a Scanivalve, a mechanical multiplexer which switches through each pressure port sequentially and takes measurements. The pressure transducer used has a full scale operating range of +/- 5 psig. Ten measurements of the static pressure are taken at 2 Hz at each pressure port location within the channel, as well as three additional ambient ports. The static pressure distribution throughout the length of the channel is then obtained. Ten measurements are taken to reduce precision error. The measurements of the ambient static pressure are used to correct for the bias in the static pressure readings. Once the venturi pressure differential and channel static pressure measurements are completed, the channel friction data can be processed independently of the heat transfer data from the transient TLC test.

Heat Transfer Testing

To test the heat transfer coefficient of the channel walls, the flow is first set up for the desired Reynolds number in the heat transfer test section. After the flow has reached steady state, the channel bulk temperature is measured to obtain the initial start temperature (which is near ambient temperature). The power supply voltage is set so that the flow entrance temperature at the start of the TLC viewing window is approximately 55 °C for each case. The actual power supply setting is iterated beforehand. With the flow running and cameras recording, the power supply is switched on, to heat the flow and provide an increase in the temperature of the flow. At the same time that the power supply is switched on, the thermocouple data collection is also started simultaneously. The thermocouple data are recorded at a repetition rate of 4 Hz.

An LED light is wired into the mesh heater circuit and placed in the viewing plane of the recorder. When the mesh heater is switched on, the light also becomes lit, which marks the time at which the heater was turned on in the recorded video. The heater is left on until the color play bandwidth of the TLC has been exceeded in the entire channel (visible when the TLC turns black). Once the threshold has been exceeded, the power supply is turned off and the channel is allowed to cool back to room temperature before testing is performed for the next Reynolds number. The longest test duration of a single color play event was not allowed to exceed 45 seconds. The recorded data is then gathered for post-processing which includes the recorded thermocouple data and camera videos during the transient test and the flow rate measurements.

Data Reduction

The characteristic channel parameters are taken from the equivalent smooth wall channel in order for the results from the ribbed study to be comparable to their equivalent smooth walled counterpart. In particular, the hydraulic diameter and channel Reynolds number should at this point be clearly defined.

The wetted perimeter of the channel is defined according to (23) and the channel cross sectional area is defined as (24). The resultant open channel hydraulic diameter is defined according to (25), called open because it is equivalent to the hydraulic diameter of the unobstructed channel, or channel with no ribs. The hydraulic diameter is useful in engineering applications it allows for the diameter of a circular pipe to be generalized to pipes of non-circular cross section. The hydraulic diameter also has the special property that it is equal to the circular

diameter if the pipe cross section is round. The hydraulic diameter allows for comparisons of rectangular channel to also be made to round pipes.

$$P = 2W + 2H \tag{23}$$

$$A = WH \tag{24}$$

$$D_h = \frac{4A}{P} \tag{25}$$

The channel Reynolds number is calculated using the open channel hydraulic diameter just defined, (26). The Reynolds number of the channels tested (20,000, 30,000, and 40,000) are calculated from the open channel hydraulic diameter.

$$Re_{D_h} = \frac{4\dot{m}}{\mu P} = \frac{UD_h}{\nu} \tag{26}$$

where $\dot{m}$ is the channel mass flow rate, U is the bulk velocity in the streamwise direction, and ν is the momentum diffusivity of the fluid.

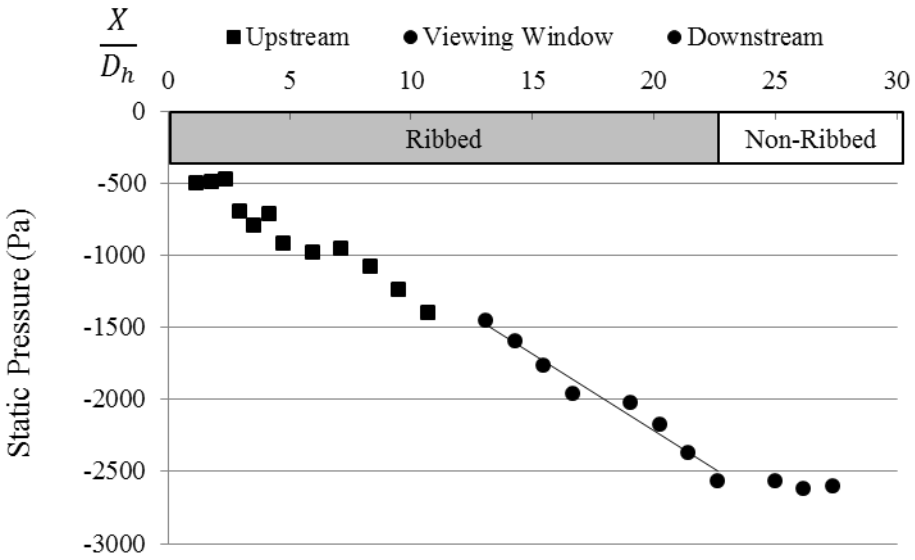

Figure 15: Static pressure distribution

Figure 15 is an example of the measured static pressure distribution during the experiment. From the distribution, the pressure gradient in the fully developed region (the viewing window) can be determined by finding the slope of the line of best fit through the points. The pressure gradient can then be used to calculate the channel friction factor according to (27).

$$f = \frac{\frac{\partial P}{\partial x} D_h}{\frac{1}{2}\rho U^2} \quad \textbf{(27)}$$

The baseline friction factor is taken from the Blasius correlation for the turbulent flow in a smooth round pipe (28):

$$f_0 = \frac{0.316}{Re^{0.25}} \quad \textbf{(28)}$$

The friction augmentation, also the friction factor augmentation, is the ratio of the actual friction factor to the baseline friction factor taken from the Blasius correlation. The Nusselt number, is a non-dimensional number which yields the ratio of convective to conduction heat transfer normal to the surface, is used to non-dimensionalize the surface heat transfer coefficient, (29):

$$Nu = \frac{hD_h}{k_{air}} \quad \textbf{(29)}$$

where h is the surface heat transfer coefficient and k_{air} is the thermal conductivity of the working fluid, air in this study. For calculating heat transfer augmentation, the baseline Nusselt number is taken from the Dittus-Boelter correlation for the heat transfer in a smooth round pipe (30):

$$Nu_0 = 0.023Re^{0.8}Pr^{0.3} \quad \textbf{(30)}$$

where Pr is the Prandtl number of the fluid. The exponent of the Prandtl number term is taken as 0.3 for cooling of the fluid, which occurs during the transient test. If heating of the fluid was occurring, the exponent on the Prandtl number term would have been taken to as 0.4.

The heat transfer augmentation (Nusselt number ratio) is the ratio of the actual Nusselt number to the baseline Nusselt number taken from the Dittus-Boelter correlation. At this point, the importance the definition and subsequent use of the channel hydraulic diameter and Reynolds number should be clear. The Blasius correlation and Dittus-Boelter correlations for friction factor and Nusselt number are both for round pipes. The channel cross section in this study is rectangular; the hydraulic diameter must be used for these two correlations to still be applicable. In addition, a characteristic length scale is needed for the Reynolds number and Nusselt number

of the channel. The hydraulic diameter serves as a convenient characteristic length for these numbers.

The Semi-Infinite Solid

The heat diffusion equation (31) is a partial differential equation that describes the distribution of heat in a given region over a period of time:

$$\rho c \frac{\partial T}{\partial t} + \nabla \cdot (-k \nabla T) - Q = 0 \qquad \textbf{(31)}$$

where ρ is the material density, c is the specific heat, k is the thermal conductivity. Whenever the heat diffusion can be considered one-dimensional and there are no heat sources or sinks (Q = 0), the heat equation of the domain of Figure 16 can be described by (32), where α is the thermal diffusivity of the solid material. The solution to (32) with initial conditions given by (33) and boundary conditions described by (34) has been obtained analytically, (35).

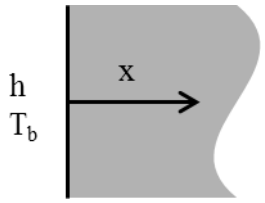

Figure 16: 1-D Semi-infinite solid domain

Governing Equation

$$\alpha \frac{\partial^2 T}{\partial x^2} = \frac{\partial T}{\partial t} \quad (32)$$

Initial Condition

$$T(x,0) = T_i \quad (33)$$

Boundary Conditions

$$-k\frac{\partial T(0,t)}{\partial t} = \mathrm{h}(T_b - T)$$
$$\mathrm{T}(\mathrm{x} \to \infty, 0) = T_i \quad (34)$$

$$\frac{T(x,t) - T_i}{T_b - T_i} = erfc\,\frac{x}{2\sqrt{\alpha t}} - \left[\exp\left(\frac{hx}{k} + \frac{h^2 \alpha t}{k^2}\right)\right]\left[\mathrm{erfc}\left(\frac{x}{2\sqrt{\alpha t}} + \frac{h\sqrt{\alpha t}}{k}\right)\right] \quad (35)$$

The temperature at the surface of the solid then can be determined by evaluating (35) at *x=0* to obtain (36). Additional discussion of the semi-infinite solid can be found in the external texts Fundamentals of Heat and Mass Transfer (Incropera, Dewitt, Bergman, & Lavine, 2006) and Heat Transfer (Bejan, 1993).

$$\frac{T_w - T_i}{T_b - T_i} = 1 - \exp\left(\frac{h^2 \alpha t}{k^2}\right)\mathrm{erfc}\left(\frac{h\sqrt{\alpha t}}{k}\right) \quad (36)$$

Introducing a new variable β defined in (37), (36) can be rewritten in the form of (38).

$$\beta = \frac{h\sqrt{\alpha t}}{k} \quad (37)$$

$$\frac{T_w - T_i}{T_b - T_i} = 1 - \exp(\beta^2)\,\mathrm{erfc}(\beta) \quad (38)$$

If the left-side of the equality in (38) is known (T_w is known for some time, say *t*), the right hand side can be solved using iterative techniques to solve for β. Following the premise that the time t is known for when T_w occurs, if α, and *k* are also known then the heat transfer

coefficient (h) can also be solved for. This method of calculating the heat transfer coefficient is the principle of several transient techniques, including the transient-TLC technique used in this study. Equations (35) and (38) are for the case of a constant bulk temperature (T_b does not vary with time). For situations in which the bulk temperature does vary with time, then the surface temperature obeys a slightly different relation (39) which makes use of Duhamel's superposition theorem. Because the heat equation is linear, any linear combination of solutions to the heat equation is also a solution. Equation (39) describes a method to obtain the surface temperature through a superposition of infinitesimal changes or steps of the bulk temperature.

$$T_w - T_i = \int_0^t \left[1 - \exp\left(\frac{h^2\alpha(t-\tau)}{k^2}\right)\operatorname{erfc}\left(\frac{h\sqrt{\alpha(t-\tau)}}{k}\right)\right]\left[\frac{\partial T_b}{\partial \tau}\right]d\tau \qquad \textbf{(39)}$$

The characteristic TLC temperature of the peak green color intensity is used for T_w. The channel bulk temperature measured at steady state before the heat is provided is used as the initial temperature, T_i. The measured centerline temperatures from the thermocouples dispersed in the test section is used to curve fit the local time varying bulk temperature according to (40) to obtain the curve fit parameters A, B, and T_f.

$$T_b(x,t) = \left(T_f - T_i\right)(Ax+1)(1-e^{Bt}) + T_i \qquad \textbf{(40)}$$

A typical measurement of the centerline temperature at the start of the viewing window is shown in Figure 17, from the bulk temperature is seen not as an instantaneous step. The straightforward application of (36) is not applicable and (39) must be used to maintain the accuracy of the solution.

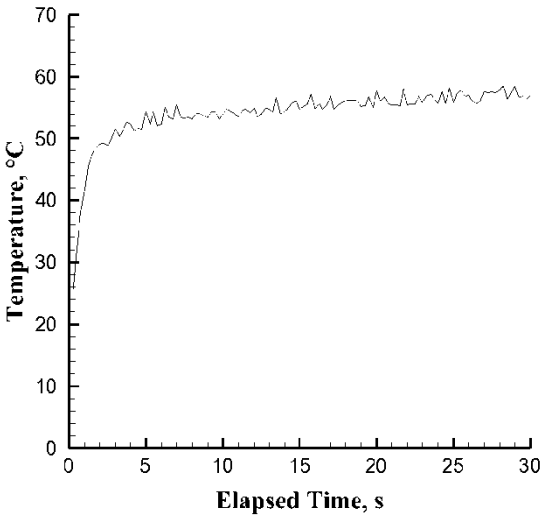

Figure 17: Centerline entrance temperature at start of viewing window

The local heat transfer coefficient over a surface coated with liquid crystals can be obtained from a transient test using the 1D semi-infinite solid model. This assumption is valid for sufficiently short test duration such that the heat penetration depth is less than the total wall thickness; the maximum Fourier number of the longest test was calculated to be less than 0.02 to verify this assumption. The 1-D semi-infinite solid approach is only applied to the non-ribbed portions of the channel where the surface is directly exposed to the convective conditions. For the copper ribs, a lumped capacitance approach is used to calculate the heat transfer coefficients on the surface of the ribs.

Lumped Capacitance Model

Another class of problems in transient heat conduction can be solved for the lumped capacitance model which assumes that the temperature of the solid is spatially uniform at each instant in the transient process; the temperature of the solid depends only on the time elapsed and

not the position within the solid at which the temperature is sampled. In principle, heat conduction in the absence of any temperature gradient implies that the conductivity of the solid is infinite, an impossible condition. However, the condition that the temperature is spatially uniform can be well-approximated if the conduction resistance within the solid is small compared to the resistance to heat transfer outside the solid. A criteria used to determine whether the temperature differences within the solid can be neglected is the Biot number, (41). In order to neglect the temperature differences and used the lumped capacitance method the Biot number should be small, less than 0.1. Conservative estimates of the Biot number for the copper ribs used in this study were calculated to be less than 0.0001 and hence the validity of the lumped capacitance model was determined to be acceptable before performing the experiments.

$$Bi = \frac{hL_{cr}}{k_{cu}} \ll 0.1 \qquad \textbf{(41)}$$

In neglecting the temperature gradients inside the solid, the heat equation no longer provides useful solutions. Instead, an energy balance on the surface of the control volume is used to derive a new solution, (42). The linear ordinary differential equation (42) has the solution given by (43). An introductory discussion into the lumped capacitance model can be found in Fundamentals of Heat and Mass Transfer (Incropera, Dewitt, Bergman, & Lavine, 2006) and Heat Transfer (Bejan, 1993).

$$-hA_s(T - T_b) = \rho Vc\frac{dT}{dt} \qquad \textbf{(42)}$$

$$\frac{T(t) - T_i}{T_b - T_i} = 1 - e^{-\frac{hA_s}{\rho Vc}t} \qquad \textbf{(43)}$$

Equation (43) is only valid where the external bulk temperature is constant with respect to the time variable. To obtain the solution to the lumped capacitance model for a time-varying bulk temperature, (44) must be used to solve for time evolution of the temperature of the solid. In this study, (44) is used to solve for the surface heat transfer coefficient of the copper rib features after the transient test.

$$T(t) - T_i = \int_0^t \frac{hA_s}{\rho Vc}[T_b(\tau) - T_i]\left[e^{-\frac{hA_s}{\rho Vc}(t-\tau)}\right]d\tau \qquad \textbf{(44)}$$

The heat transfer coefficient used in (44) is the actual surface heat transfer coefficient, the heat transfer coefficient based on the projected smooth wall area can be obtained from the ratio of areas of the convectively exposed surfaces of the rib (A_s) to the projected area at the base (A_p) by virtue of the fact that the actual heat flux is invariant to definitions of surface area and heat transfer coefficient (45). Figure 18 provides a description of the surface areas. The area ratios are tabulated in Table 3 along with the ratio of the total convective surface area on the top and bottom ribbed walls (A_{actual}) with the projected smooth wall area (A_{sw}).

If the baseline heat transfer performance of the channel is taken from an equivalent smooth pipe then the heat transfer coefficient should be based on the projected smooth wall area is used to calculate the heat transfer augmentation in order to capture all of the additional heat transfer benefit from the flow disruption caused by the feature and the increase in surface area. The heat transfer coefficients obtained for the semi-infinite solid are already calculated from the actual smooth wall area and hence do not need to be re-scaled, unlike the lumped capacitance model.

$$h_p A_p = h_s A_s \quad \textbf{(45)}$$

Table 3: Ratios of rib and projected surface areas

	A1	A3	A5
$\frac{A_s}{A_p}$	3.00	1.66	1.40
$\frac{A_{actual}}{A_{sw}}$	1.20	1.20	1.20

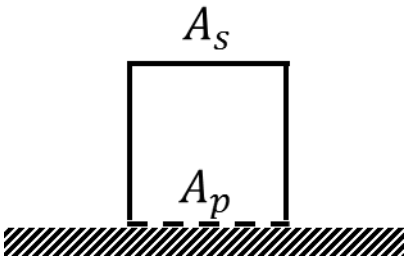

Figure 18: Rib surface area denotations

Post-Processing

Post processing is performed using a MATLAB code. A diagrammatic flow chart of the post processing process to arrive at the heat transfer coefficient is shown in Figure 19.

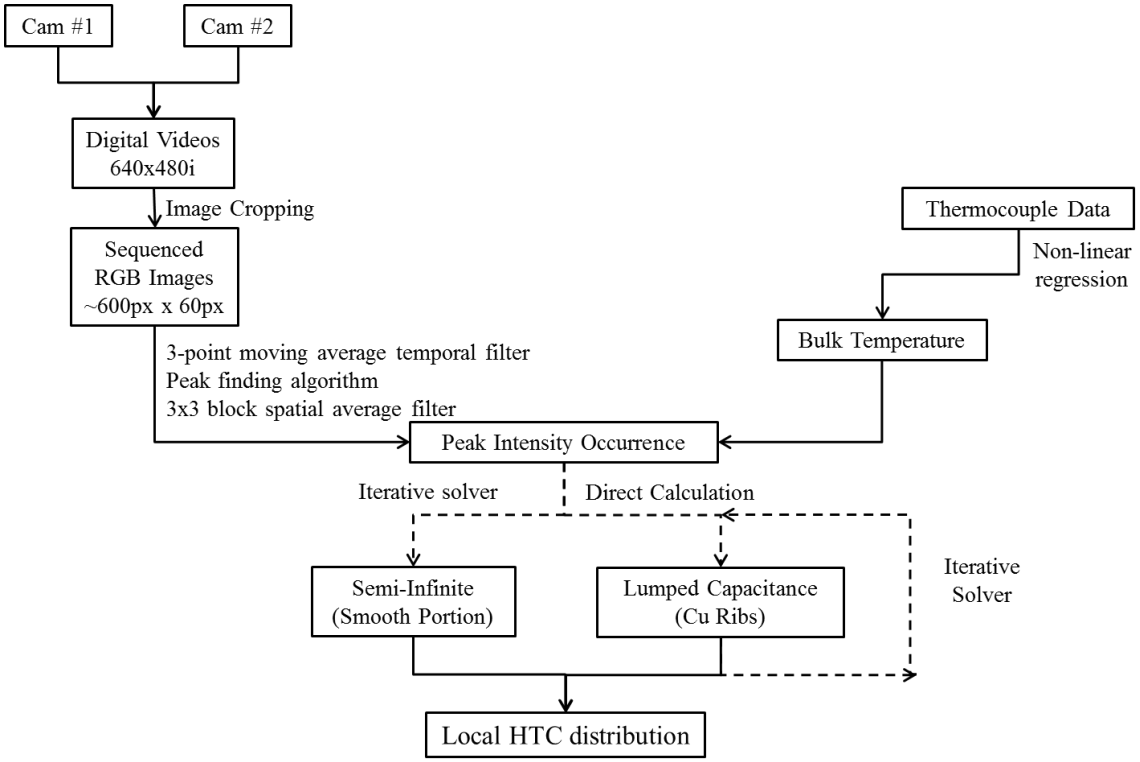

Figure 19: TLC processing flow chart

The recorded videos from each CCD camera are digitized onto a PC. The raw videos are divided to remove any extra recorded events that are not needed for the post processing and then cropped to keep only the viewing window, any background is removed to reduce the size of the video for the following steps in the post processing. The cropped videos are then converted into a series of sequenced images containing the local RGB intensities measured by the CCD at each pixel location. An example of the recorded time history of the green signal intensity for a single pixel is given by Figure 20 .

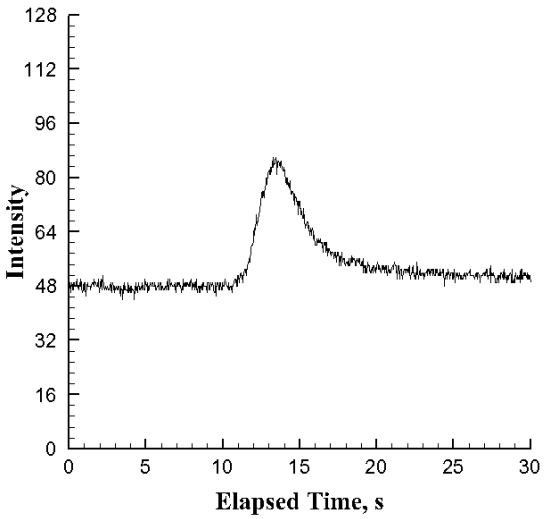

Figure 20: Time history of recorded green intensities

From the sequence of RGB image intensities, a three point moving average filter is applied in the temporal domain to each pixel location to smooth the time series data and reduce the influence of the background noise. The peak finding algorithm is then used to determine the precise frame number at which the peak color intensities occur which can then be converted into a physical time using the camera frame rate. The peak finding algorithm used in this study searches for the frame or time occurrence of the absolute maximum intensity of each color. The peak finding algorithm is performed for every pixel location in the viewing window to determine precisely the time at which the peak reflected intensity occurs for each color. After the peak finding algorithm is complete, a 3x3 pixel block spatial averaging filter is performed to smooth the calculated peak times. Only the time occurrence of the green reflected intensity is used in the current study because it has both a high reflected intensity and distinct peak. The blue signal, although comparable in intensity to the green signal does not exhibit as distinct peak intensity as

the green and red peaks, which would lead to large uncertainties in the temperature and time occurrence of the peak if blue were used. On the other hand, the red peak is distinct, but the reflected color intensity of the red signal is not as strong as the green signal. Hence the green signal can be more accurately recorded using a CCD camera.

Knowing T_i, T_b, T_w, the thermophysical properties of acrylic, and the time at which T_w occurs for each pixel, the heat transfer coefficient at each pixel location can be calculated by iterating.

Experimental Uncertainty

The calculated uncertainty for the final results was performed using the procedures described by (Kline & McClintock, 1953) and (Moffat, 1985). Each rib pitch was measured to be at least accurate to within 2.5% of the overall rib pitch, 1 mm (0.03 in). The uncertainty in the flow rate measurement and Reynolds number is less than 2.5%. The uncertainty in the friction factor augmentation is less than 8.2%. Neglecting the bias from the error in assuming a lumped capacitance model the maximum uncertainty in the ribbed heat transfer coefficients using the lumped capacitance model is estimated to be less than 11% for all cases, the uncertainty in the un-ribbed semi-infinite model heat transfer coefficients is less than 5% after neglecting the uncertainties in material properties and errors in assuming one-dimensional semi-infinite solid, the combined uncertainty in the overall heat transfer augmentation is less than 8.0% for case A5.

Experimental Results

The key experimental results obtained are all presented in this section along with dissemination of their trends and implications. First, the results of the smooth wall validation

testing is presented in order to establish confidence in the methodology and accuracy of the applied (transient TLC) technique. The results from the ribbed channel studies are then presented in the following subsection.

Smooth Wall Validation

A smooth wall validation test (with no ribs) was performed to validate the experimental setup and procedure used. Since no ribbed features were tested, the smooth wall validation testing corresponds to the standard transient TLC technique. The lumped capacitance model is not applied to any portion of the channel and all of the surface heat transfer coefficients are calculated from the one-dimensional semi-infinite solid model. The smooth wall validation testing is performed using the same method and tested under the same conditions as the ribbed channels. The smooth wall validation test can be considered as a baseline test and any inaccuracies in the smooth wall test are also applicable to the ribbed channels. Following the experimental procedure and post-processing steps described in previous chapters, the local contours of the heat transfer augmentation (Nusselt number ratio) of the smooth wall tests are plotted in Figure 21. The streamwise direction is plotted on the horizontal axis and the channel spanwise direction is plotted on the vertical axis. The streamwise coordinate is non-dimensionalized by the channel hydraulic diameter starting from the exit of the heater box. The TLC painted window is 10 inches from the exit of the heater box, hence the data are only available after ~12 D_h. The spanwise coordinate is non-dimensionalized using the channel width starting at the channel half-width. The contours levels are colored by the magnitude of the Nusselt number ratio, interpolation between cells is used to produce a continuous color map.

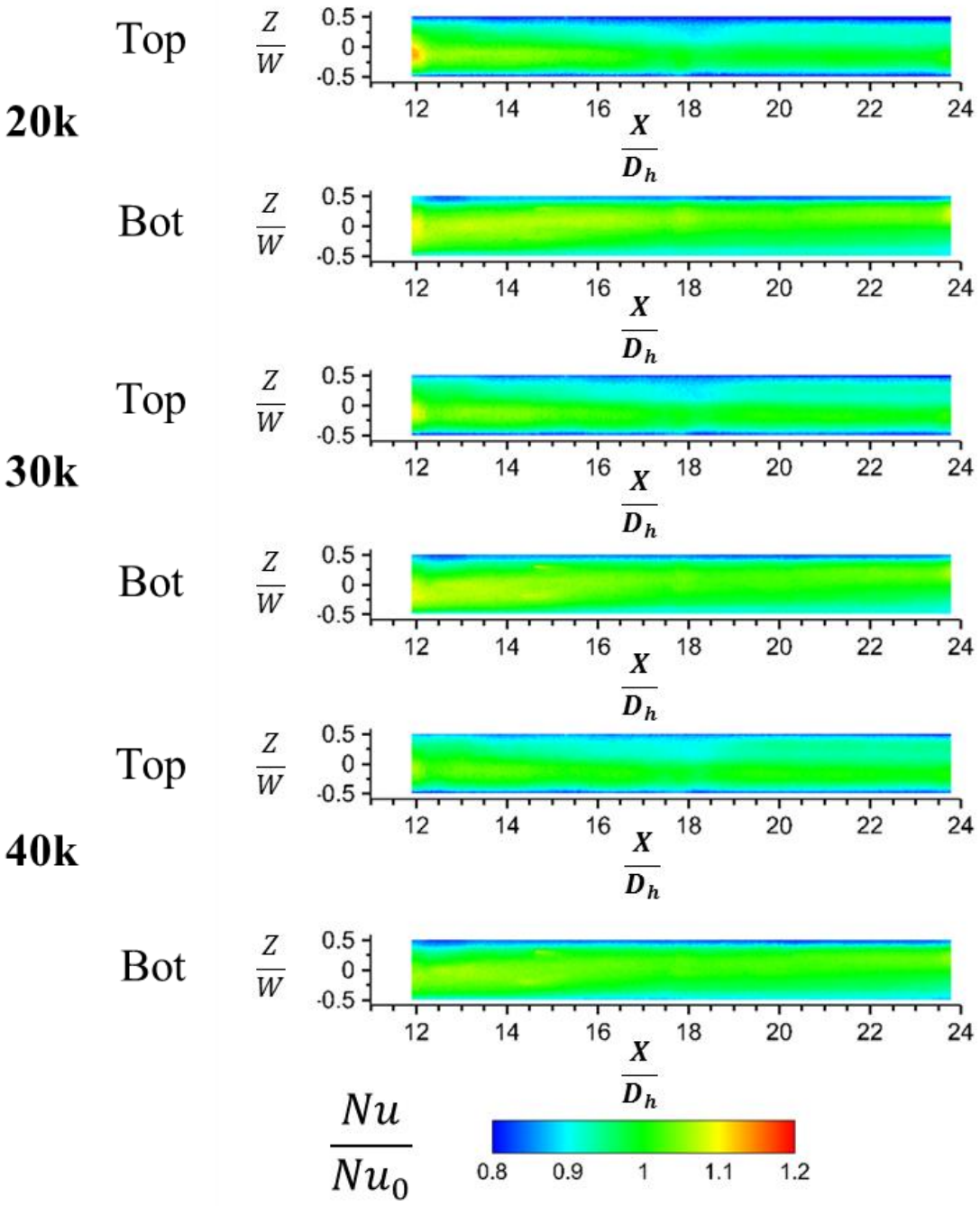

Figure 21: Local heat transfer augmentation of smooth wall validation

From the local plots, the highest Nusselt numbers occur near the channel centerline, with the lowest occurring near the corners. The turbulence anisotropy in a rectangular channel and the resulting secondary flows and corner vortices as described by Pinelli et al. help to explain the differences in Nusselt number near the corners from the Dittus-Boelter correlation (Pinelli, Uhlmann, Sekimoto, & Kawahara, 2010). To begin with, the Dittus-Boelter correlation only applies to the overall channel averaged heat transfer anyway; hence local differences (minima and maxima) are expected to occur. The heat conduction into the acrylic substrate near the corners also cannot be considered strictly 1-D, the heat transfer coefficients calculated near these corners are also affected by this error in assuming a 1-D semi-infinite solid.

The experimental data from the smooth wall validation test, Table 4, agree well with the predicted Nusselt numbers from the Dittus-Boelter correlation for all three Reynolds numbers, the overall average Nusselt number ratio being 0.97 at 20,000 Re, 0.96 at 30,000 Re, and 0.96 at 40,000 Re. Since the smooth wall validation results were in agreement for heat transfer, the Dittus-Boelter correlation is determined to be acceptable for use as the baseline case for heat transfer when normalizing the heat transfer results of the ribbed cases.

Table 4: Wall-averaged heat transfer augmentation for Smooth Wall Validation

Case	$\frac{\overline{Nu}}{Nu_0}$	20,000 Re	30,000 Re	40,000 Re
SW	Overall	0.97	0.96	0.96

Just as the current experimental setup must match known correlations for heat transfer, it must likewise agree with correlations for friction factor. The measured static pressure

distribution in the channel is plotted in Figure 22, Figure 23, and Figure 24 for channel Reynolds numbers of 20,000, 30,000, and 40,000, respectively.

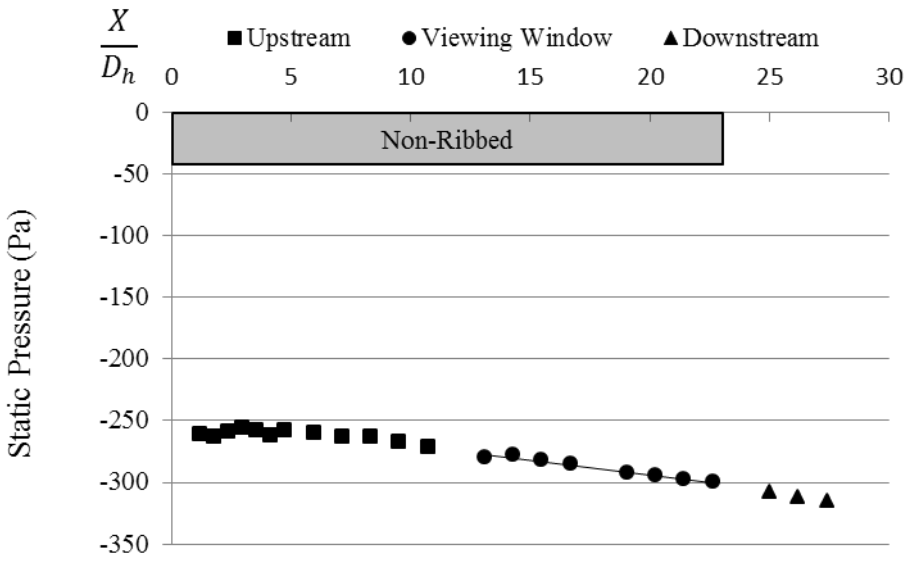

Figure 22: Static pressure distribution of Smooth Wall at 20,000 Re

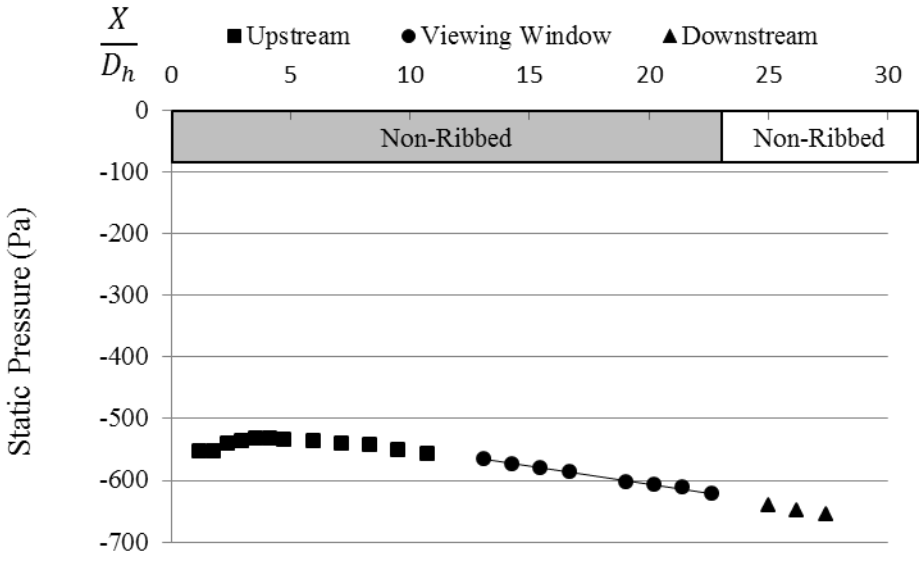

Figure 23: Static pressure distribution of Smooth Wall at 30,000 Re

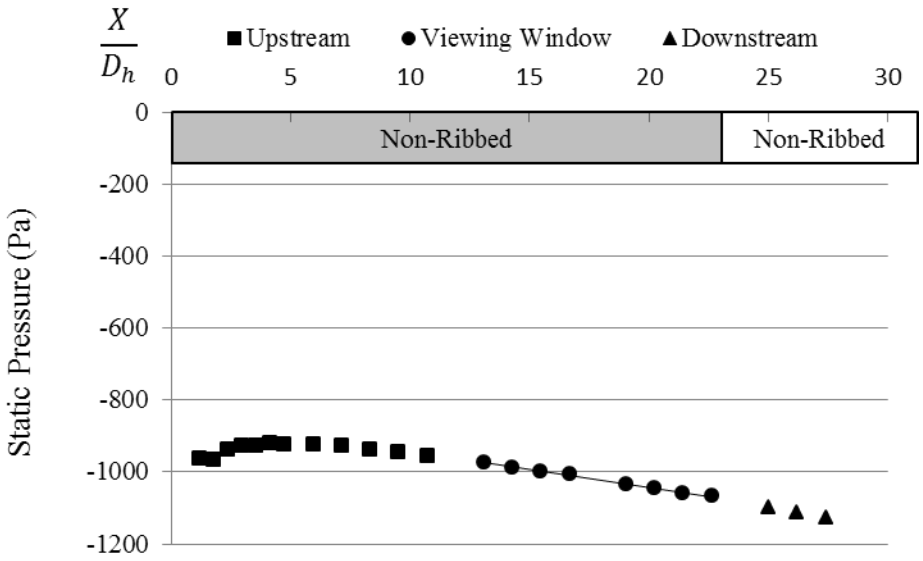

Figure 24: Static pressure distribution of Smooth Wall at 40,000 Re

The initial development of the hydrodynamic boundary layer can be seen the locations upstream of the viewing window by the non-linear portion. Smooth pipes are notoriously difficult to reach a fully developed state, the velocity profile and friction factor can take more than 25 hydraulic diameters to reach a fully developed state (Kakac, Shah, & Aung, 1987). A common engineering prediction for the developing length of turbulent flow in pipes is approximately 10 hydraulic diameters; that convention is seen to be valid in this case. After 5 hydraulic diameters, the static pressure is already approaching a linear profile for all three Reynolds numbers tested. Table 5 is a summary of the pressure gradients in the fully developed portion of the channel, calculated friction factor, and friction factor augmentation at each channel Reynolds number tested.

Table 5: Summary of experimental friction results for smooth wall validation

Re	$\frac{\partial P}{\partial x}$	f	$\frac{f}{f_0}$
20000	127	0.0201	0.76
30000	300	0.0217	0.90
40000	511	0.0208	0.93

The channel friction factor and friction augmentation of the smooth walled channel was 25% lower than the Blasius solution at 20,000 Re and approximately 10% lower at 30,000 Re and 40,000 Re. This discrepancy is attributable to the small magnitudes of the static pressure measurements in the smooth walled channel. The inlet flow is from ambient; at the location in the channel where the static pressure is measured the static pressure in the channel is near ambient pressure in magnitude, because the smooth wall does not incur large pressure drops in the channel. The resulting static pressures being close to ambient pressure, was prone to bias with the Scanivalve device used to measure the static pressure. The greater pressure drop occurring for the ribbed channels and the corresponding greater static pressure magnitudes is not as susceptible to this bias error.

The current results are acceptable for the purpose of validating the accuracy of the experimental setup. More accurate results of the friction factor in the channels could be done on channels of much longer relative lengths (more length in hydraulic diameters). This approach however is not as practical for the ribbed studies because of the cost of the machining of additional ribs and TLC (for the heat transfer test). Only a very limited number of ribs could be

machined for testing (16 for each case) because of the expense. It is also logistically difficult to apply TLC to a very long section; many additional factors need to be considered, such as the viewing angle effect and possibly the need for additional cameras to maintain resolving power.

Case A1: 1:1 Rib Aspect Ratio Local Heat Transfer Results

The local contours of the heat transfer augmentation of the square ribs case (Case A1) are plotted in Figure 25. Instead of the channel hydraulic diameter, the streamwise coordinate of the ribbed channels is non-dimensionalized instead by the rib pitch (P) starting from the leading edge (upstream edge) of the 1st rib in the TLC painted window (the 9th rib from the exit of the heater box). The ribs have a relative coverage of $0<X/P<0.1$ with the remaining portions non-ribbed $0.1<X/P<1.0$. The local data presented only shows the portion between the 2nd rib in the TLC painted window and the 7th rib.

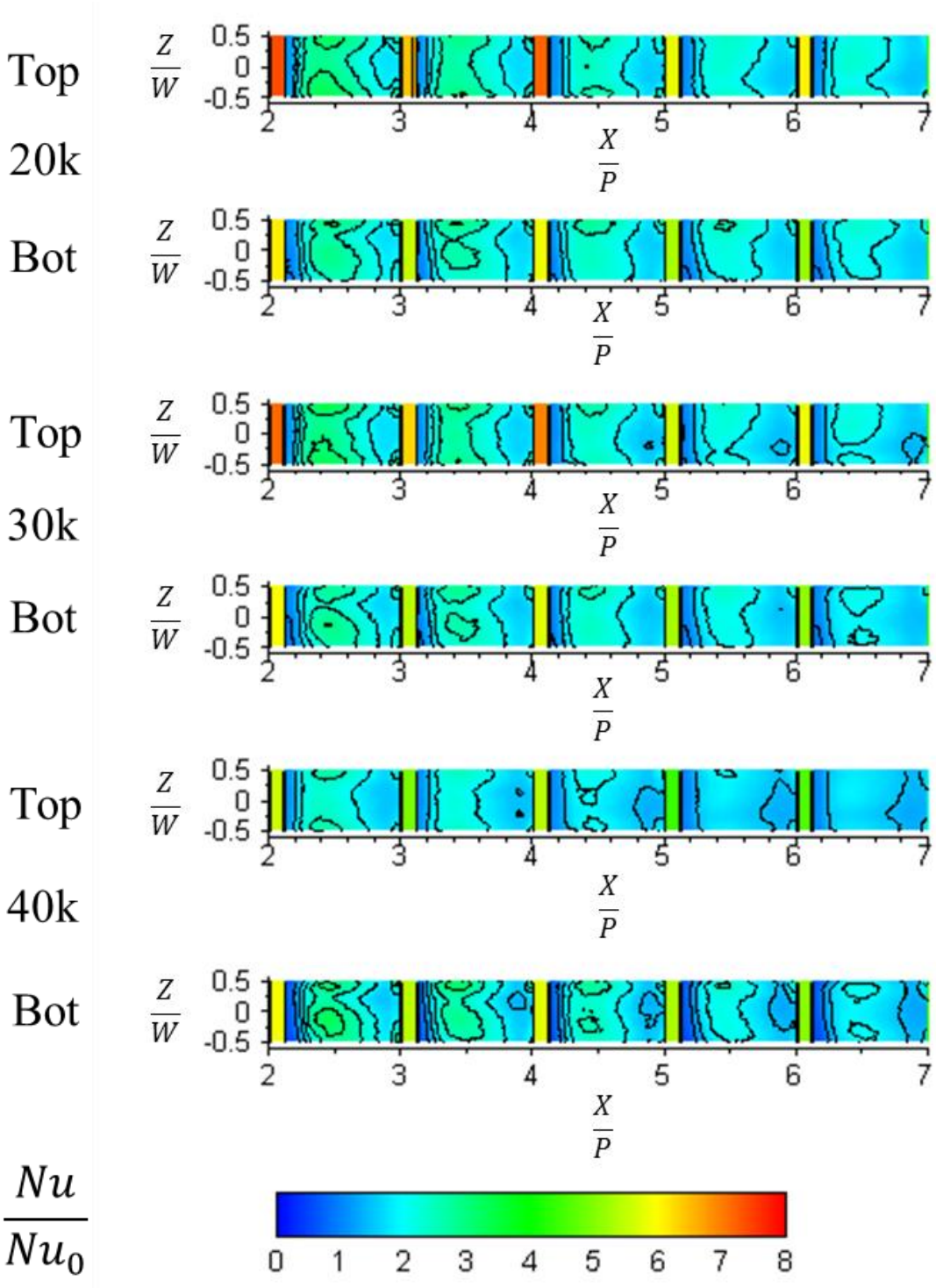

Figure 25: Local heat transfer augmentation of Case A1

Immediately behind each rib, a region of relatively low heat transfer is encountered. After a few rib heights, the heat transfer increases rapidly to reach a maximum before decreasing again before the next rib is encountered. The same local trends occurred at each Reynolds number tested; the local trends in Nusselt number ratios did not change significantly with Reynolds number. Consistently, the ribbed portions of the channel have the highest heat transfer enhancement (higher than the non-ribbed portions). Bearing in mind that the heat transfer coefficient of the ribs is calculated from the area of the base of the rib (the projected smooth walled area), the actual heat transfer coefficient of the active surfaces of the rib is really smaller. However, in comparing the ribbed channel to an equivalent smooth channel, the heat transfer coefficient based on the equivalent smooth channel must be used and the total contribution of the ribs onto the resulting heat transfer must be accounted for.

Case A3: 3:1 Rib Aspect Ratio Local Heat Transfer Results

The local contours of the heat transfer augmentation of the 3:1 aspect ratio ribs case (Case A3) are plotted in Figure 26. The ribs have a relative coverage of $0<X/P<0.30$ with the remaining portions non-ribbed $0.0.30<X/P<1.0$.

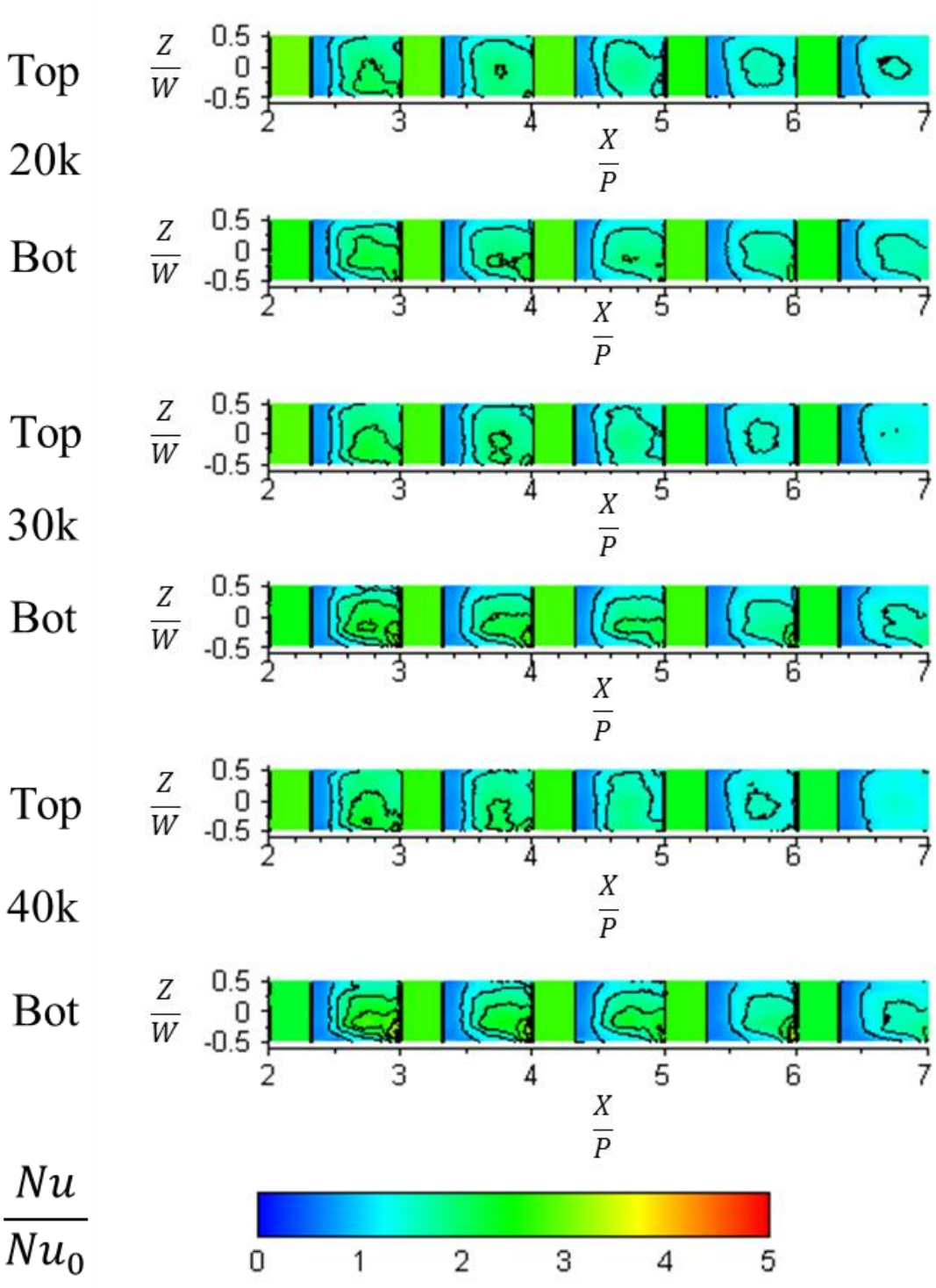

Figure 26: Local heat transfer augmentation of Case A3

Similar to the square ribs case, a region of relatively low heat transfer is encountered immediately behind each rib, but has increased in relative size over the square ribs case. The increase in the heat transfer enhancement after the region of poor heat transfer is also not as strong as the square rib. The local maximum of heat transfer between ribs is also not distinct for Case A3 compared to Case A1. The heat transfer enhancement of the ribbed portions is also much less than the square ribs. The local trends in heat transfer enhancement also did not change significantly with Reynolds number for Case A3.

Case A5: 5:1 Rib Aspect Ratio Local Heat Transfer Results

The local contours of the heat transfer augmentation of the 5:1 aspect ratio ribs case (Case A5) are plotted in Figure 27. The ribs have a relative coverage of $0<X/P<0.50$ with the remaining portions non-ribbed $0.0.50<X/P<1.0$.

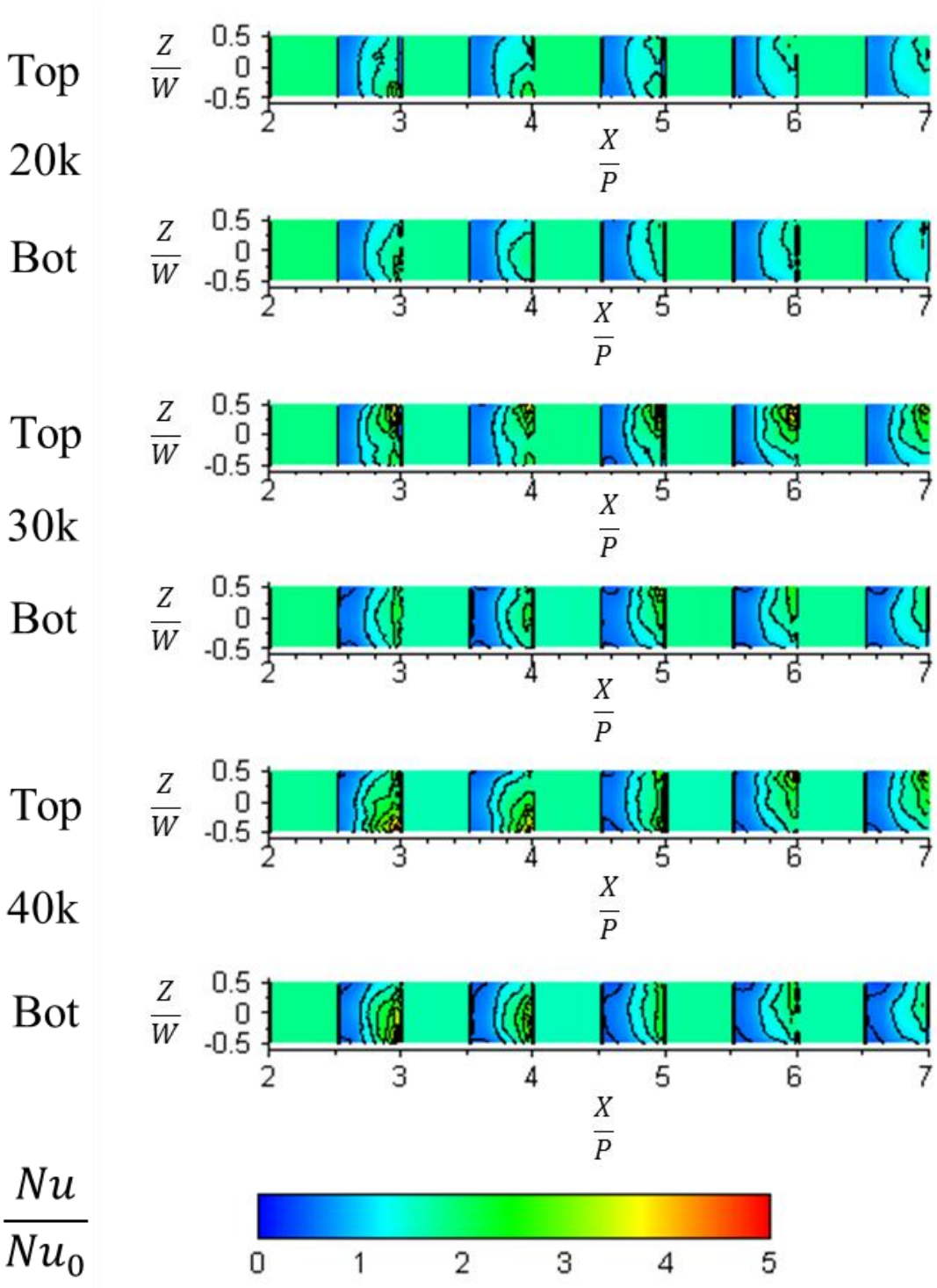

Figure 27: Local heat transfer augmentation of Case A5

Similar to the two previous rib cases, a region of relatively low heat transfer is encountered immediately behind each rib. The size of the lowest heat transfer region however, occupies nearly half of the region in between ribs, significantly greater coverage than before After the low heat transfer region, the heat transfer increases until the next rib is reached. Unlike the past rib cases, there is no local maximum in heat transfer in between the ribs and no subsequent decrease in heat transfer enhancement before the next rib, the greatest heat transfer enhancement on the non-ribbed portion occurs directly before the start of the next rib. The local trends in heat transfer augmentation for Case A5 also did not change significantly with the Reynolds numbers tested, similar to the previous two ribbed cases

Comparison of Experimental Local Heat transfer Results

The local heat transfer augmentation results of each of the ribbed channels at 30,000 Reynolds number are shown together in Figure 28; the local heat transfer results are plotted for a single Reynolds number to compare the heat transfer performances of each rib geometry. The contour level has been truncated to shown only Nusselt Number ratios of 0-5, with higher values taken on the greatest color of the contour. The same contour applied to all three channels helps to make the comparison easier between the performances of each case.

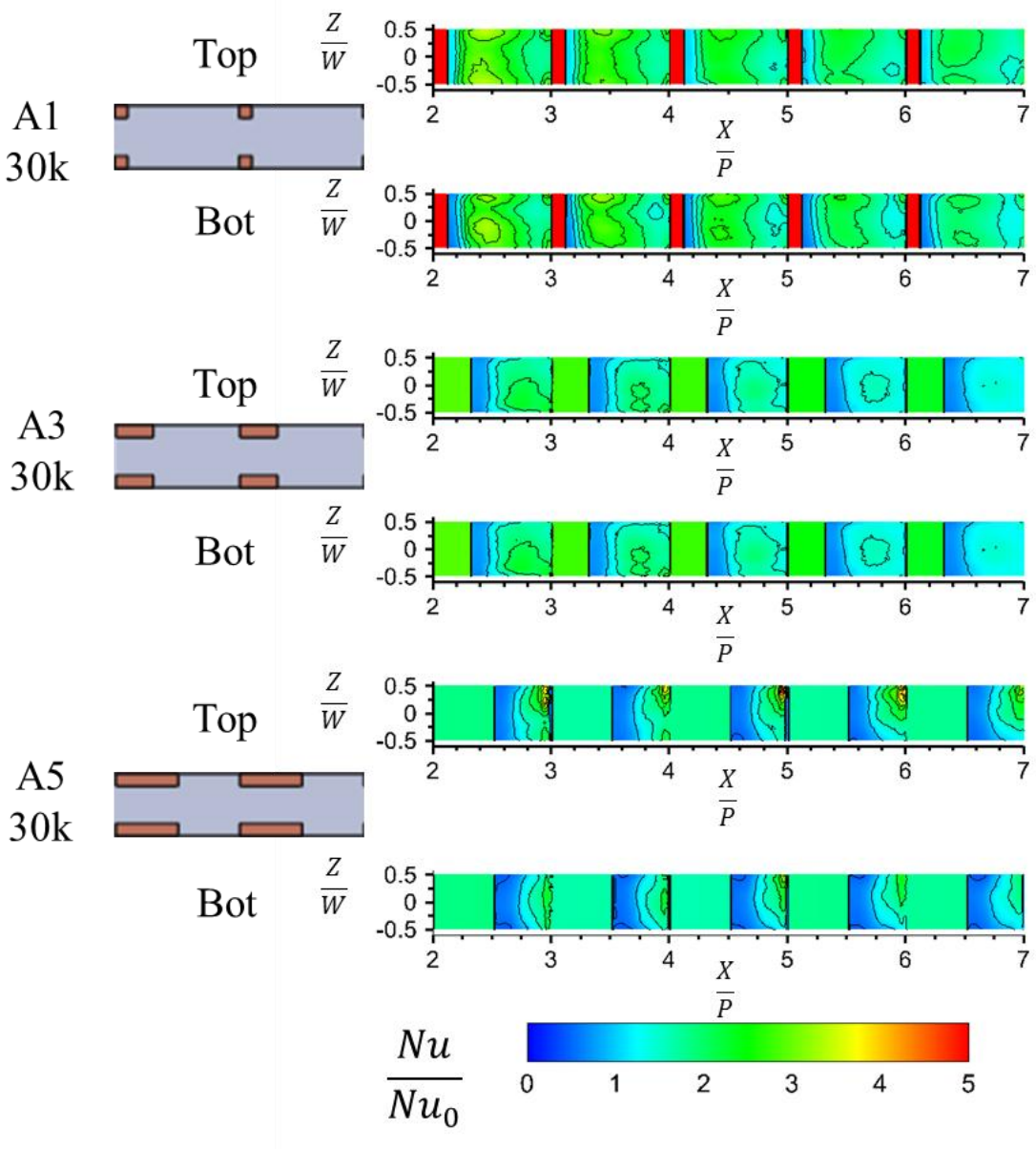

Figure 28: Local heat transfer augmentation of ribbed walls at 30,000 Re

The highest heat transfer augmentation for Case A1 occurs roughly half a rib pitch from the start of each rib (X/P ~ 0.5). For Case A3, the peak heat transfer location is pushed further downstream (X/P ~ 0.75). For Case A5, the widest rib case, the location of the highest heat

transfer is delayed to immediately before the next rib. With increasing rib width, the size of the lowest heat transfer region immediately behind each rib also widens. The magnitude of the peak heat transfer augmentation also decreases as well as the average heat transfer augmentation of the ribbed portion of the channel. The square ribs also produced the highest heat transfer enhancement on the rib. The 5:1 aspect ratio ribs produced the lowest heat transfer.

Comparison of Experimental Spanwise Averaged Heat transfer Results

The spanwise-averaged heat transfer augmentation of each rib case at 30,000 Reynolds number is shown in Figure 29. The spanwise average is performed by averaging all of the local Nusselt number ratios along the same spanwise direction (along the direction of the channel width). The upward triangle shapes correspond to the spanwise average of the data from the top walls, and the downward facing triangle shapes in the figure correspond to the spanwise average of the data from the bottom walls.

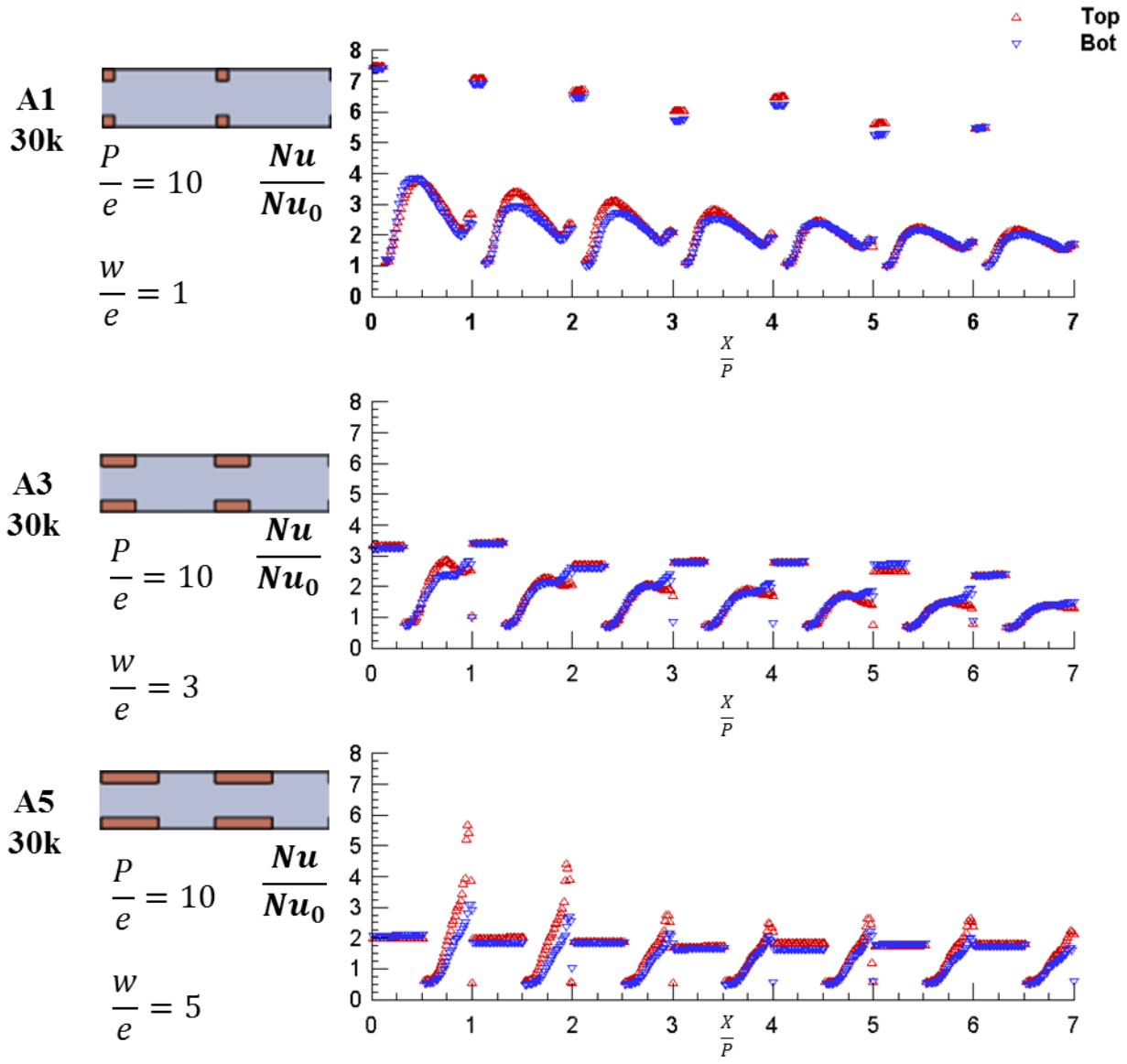

Figure 29: Spanwise-averged heat transfer augmentation of ribbed walls at 30,000 Re

For case A1, despite the separation region directly behind the rib and the relatively low heat transfer in that region, the Nusselt number ratios are still greater than unity by approximately 10%. The flow over a rib is essentially a flow over a backward facing step. The separated shear layer behind each rib contributes to a high turbulent kinetic energy in this region

and maintains the thermal transport capabilities of the flow and prevents the Nusselt numbers from dropping below unity.

The Nusselt number ratios reach a maximum at a relative pitch of around 0.4-0.5 P for Case A1. Since no wall shear measurements were taken, it is difficult to claim that the region of peak heat transfer is also the location of the reattachment. The two locations should be loosely correlated, the location of peak heat transfer and location of reattachment. Physically, the reattachment disrupts any boundary layer in this region, resulting in the characteristically high heat transfer in this area. Moving upstream and downstream from this location, the heat transfer decreases. The reversed flow boundary layer growth causes the reduction in heat transfer upstream. Downstream, the growth of the boundary layer after reattachment also causes a reduction in heat transfer. The heat transfer augmentation at the reattachment location is in the range of 2.8-3.0 and decays to approximately 1.8 directly in front of the rib.

The reattachment length for smaller transverse ribs is well known to occur after 6-8 rib heights (Kakac, Shah, & Aung, 1987). With the larger rib height in the current study, the expansion ratio behind each rib is much greater compared to the smaller rib height and can explain the shorter reattachment lengths found in the current study, or at least the earlier peak in the heat transfer. Larger expansion ratios behind a backward facing step lead to higher turbulence intensities inside the separated shear layer and was previously reported by Otugen (Otugen, 1991). The increase in turbulent diffusion leads to a faster shear layer growth and results in smaller normalized (with respect to the step height) reattachment lengths.

Despite the higher Nusselt number ratios of the ribbed portion compared to the heat transfer augmentation at the reattachment, the heat transfer coefficient of the ribbed portion was calculated using the projected smooth wall area. For the 1:1 RAR, square ribs, the exposed rib surface area is triple the rib base. If the actual surface heat transfer coefficient is used, the Nusselt number ratios of the ribbed portions would be less (by a factor of one-third for the square ribs case). In this light, the actual heat transfer augmentation of the rib is not as dramatic as the reattachment. For the square ribs case, the actual surface heat transfer augmentation of the rib is actually comparable to the peak heat transfer augmentation at the reattachment location. This example demonstrates the effect of the reattachment on the heat transfer in a ribbed channel; the rib-induced reattachment effect can produce an increase in heat transfer elsewhere in the channel that is of the same strength as the rib itself. The repeated tripping of the flow caused by the rib and the reattachment occurring behind each rib in combination results in an improvement in heat transfer many times over the equivalent smooth wall and is very useful for applications where a large amount of cooling is required, hence their history of application to the internal passages of turbine blades.

The rib averaged heat transfer augmentation is significantly reduced for Case A3 and Case A5 compared to Case A1. The magnitude of the heat transfer augmentation on the rib for Case A1 was actually greater than the maximum occurring in-between two ribs. For Case A3, the heat transfer enhancement on the rib is marginally higher than the peak in-between ribs. For Case A5, the heat transfer enhancement on the rib is reduced to below that of the peak heat transfer in-between ribs. The lowest Nusselt number ratios for Case A3 and Case A5 are also significantly reduced, lower than unity immediately behind each rib. With the widening of the rib and

decreased space available between ribs, the shear layer and reattachment for the two wider rib cases is not able to maintain the heat transfer enhancement in the recirculation zone. This difference is even more evident in Case A5, where unlike Case A1 and Case A3, there is no location of maximum heat transfer in-between ribs. Instead, the location of the maximum Nusselt number ratio is pushed completely rearward and occurs immediately in front of the next rib. The decreased space between ribs prevents the reattachment from occurring and also inhibits the shear layer growth and weakens the turbulence in the channel for Case A5.

Comparison of Experimental Friction Results

The overall channel friction factor of all the cases studied is plotted in Figure 30. The overall channel friction factor is nearly constant with Reynolds number for each of the rib cases studied; the differences are on the order of the experimental uncertainty. With an increase in Reynolds number, the constant friction factor results in the friction factor augmentation of each rib configuration to be increasing with Reynolds number.

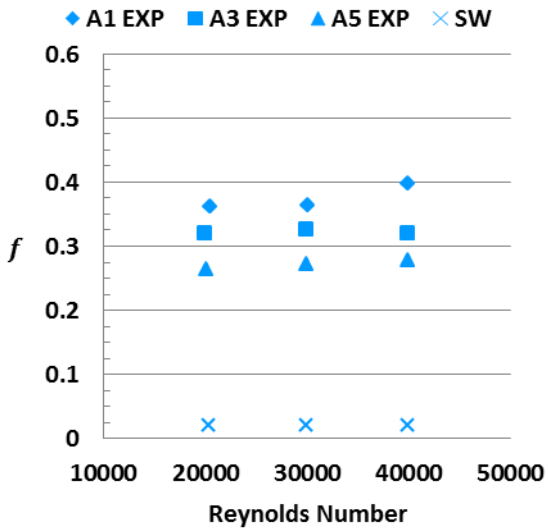

Figure 30: Experimental friction factor

The corresponding channel friction actor augmentation for each configuration is plotted in Figure 31. At each Reynolds number studied, the friction factor augmentation of A1 was consistently greater than A3; the friction factor augmentation of case A3 was also consistently greater than case A5. Case A1, which had the highest overall heat transfer augmentation, also had the greatest friction factor augmentation of the rib cases studied. The friction factor augmentation ranged from 13.6-17.8 for Case A1, 12.0-14.3 for Case A3, and 10-12.4 for Case A4 (A1>A3>A5). With increasing rib width, the friction factor augmentation also decreased.

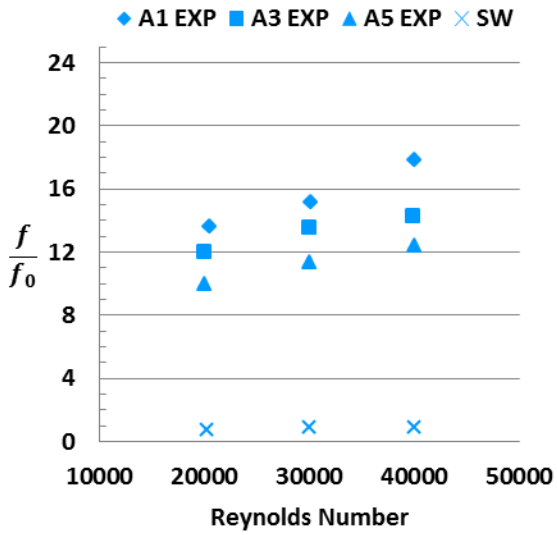

Figure 31: Experimental friction factor augmentation

Comparison of Numerical Rib and Wall Averaged Heat Transfer Results

The average heat transfer augmentation of only the ribbed portions of the channel is plotted in Figure 32. Unfilled symbols in the figure represent the rib-only averaged Nusselt number ratio. The wall averaged heat transfer augmentation of the entire top and bottom wall is contained in Figure 33. Filled symbols are used to represent the wall averaged Nusselt number ratios. The wall averaged heat transfer augmentation includes both the heat transfer augmentation of the ribbed and non-ribbed portions of the channel.

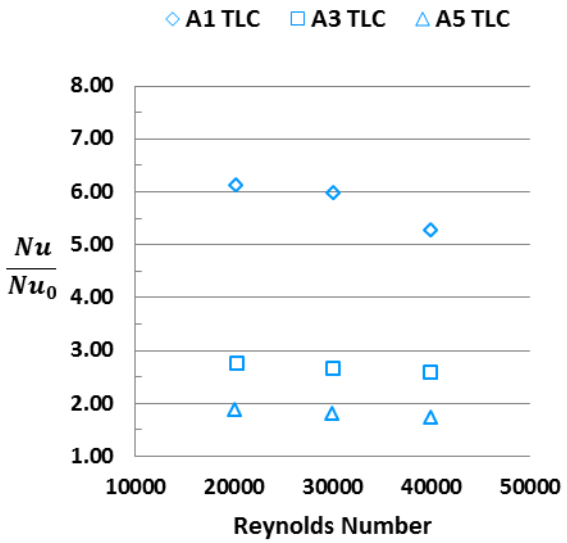

Figure 32: Heat transfer augmentation on rib from experimental study

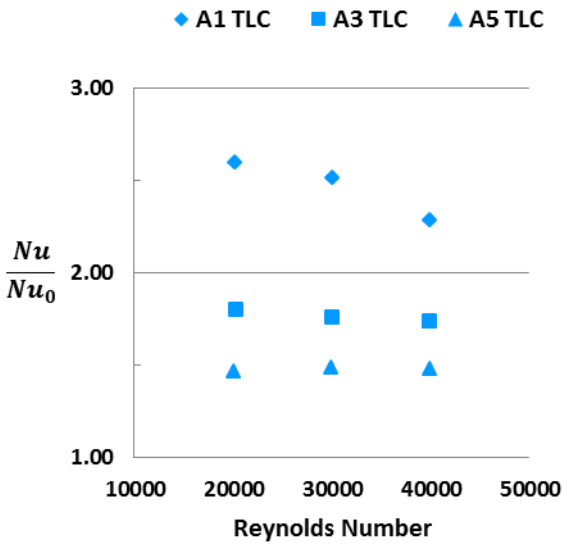

Figure 33: Average heat transfer augmentation on ribbed walls from experimental study

For all the ribbed cases studied, the overall heat transfer augmentation decreases with Reynolds number, a typical trend for surface enhancements in internal cooling channels. The increased bulk mixing that occurs at higher Reynolds numbers and the reduction in the turbulent eddy size decreases the effectiveness of any further mixing promoted by the ribs.

As the rib aspect ratio increases, the overall heat transfer augmentation also decreases but is accompanied by a reduction in the channel pressure drop and friction augmentation. The greatest overall heat transfer augmentation occurs for case A1, with the square ribs, but with also the highest friction. Likewise, case A5 had the lowest overall heat transfer augmentation with a lowest pressure drop penalty. Case A3 was moderately between A1 and A5 in both heat transfer and friction augmentation.

With the increasing rib aspect ratio and rib width, there is less room behind the rib for reattachment to occur. All local fluid momentum is loss where reattachment occurs. The loss of the reattachment region behind the rib is conjectured to be the reason for the corresponding decrease in heat transfer as well as pressure drop with wider ribs.

Smaller square ribs do not allow room on top of the rib for the secondary reattachment to occur. The benefit of a secondary reattachment can occur for the wider ribs (A3 and A5), although the wider ribs were observed to also have a reduction in the overall heat transfer augmentation.

COMPUTATIONAL METHOD

A schematic of the computational domain used in this study is shown in Figure 34. Only half of the channel is modeled; a symmetry plane is used along the channel mid-span to reduce the computational cost. Although an additional symmetry condition could have been used along the channel mid-height to reduce the computational expense even further, this symmetry plane condition was not applied in anticipation of future studies where ribs can be only applied to one wall or where ribs are applied to opposite walls in a staggered fashion. The modeling of both the top and bottom walls will facilitate an easier comparison of results between future rib studies to the current results. Since the periodic fully developed flow is really the only flow of interest in the current study, periodic boundary conditions can be used at the inlet and exit of the domain to reduce the computational domain down to a single rib pitch. The modeling of only one rib pitch significantly reduces the size of the computational domain and also reduces its complexity. Furthermore, with the use of periodic boundary conditions, turbulent inflow data does not need to be supplied at the inlet, since the turbulence of the flow at the exit is reapplied at the inlet.

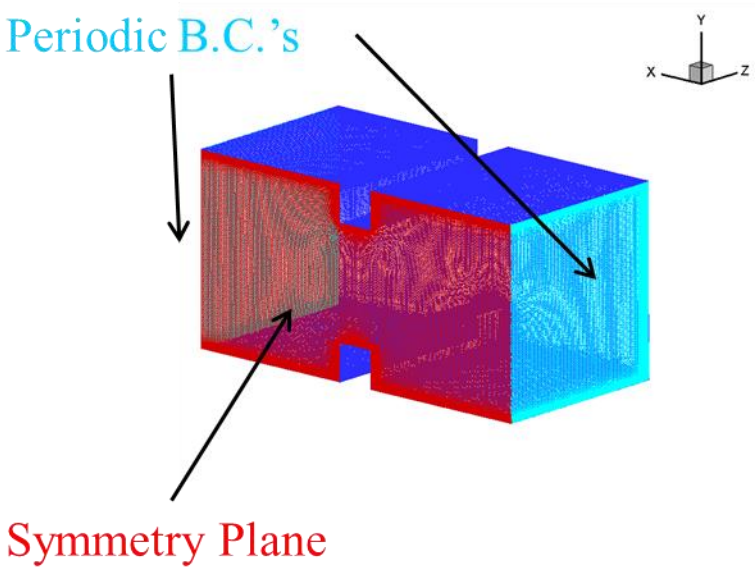

Figure 34: Computational domain

The coordinate system of the computational domain is also displayed on Figure 34. The origin of the coordinate system is placed at the channel half-width (z=0), on the upstream edge of the rib (x=0), and at the channel half-height (y=0). The channel mid-span, symmetry plane, and z=0 plane are all synonymous. The x-direction is in the flow streamwise direction. The y direction is in the direction of the channel height. The z-direction is in the direction of the channel width or span of the ribs. Nearly all the figures in this section are presented in non-dimensional form by normalized each coordinate with respect to the corresponding channel dimension (x/P, y/H, z/W).

The test matrix for the computational study is listed in Table 6. The test matrix for the computational study is the same as the experimental study. The same rib configurations are tested at 20,000, 30,000, and 40,000 Reynolds numbers.

Table 6: Computational test matrix

Case	Reynolds Number		
A1	20,000	30,000	40,000
A3	20,000	30,000	40,000
A5	20,000	30,000	40,000

Mesh Generation

The meshing of the computational domain of each rib case is performed using the commercially available software GridPro. Surfaces are defined to represent the boundaries of the problem and then the loose topology of the block structure of the mesh is defined. The topology of each rib case is shown in Figure 35, Figure 36, and Figure 37. The appropriate topology corners are assigned to each surface and the corners corresponding to the periodic interface are also defined as periodic to ensure GridPro will form a conformal mesh at the periodic interface. GridPro allows for the blocks to be defined loosely, and contains an automated optimization algorithm that will dynamically adjust the block boundaries to achieve a high quality mesh with minimal user interaction.

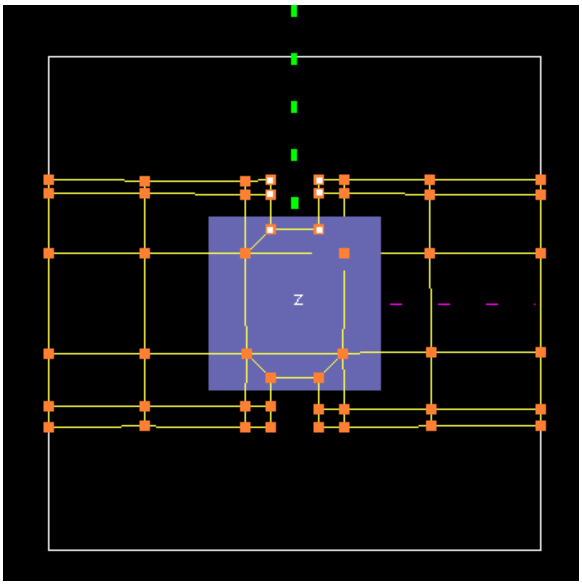

Figure 35: Case A1 topology

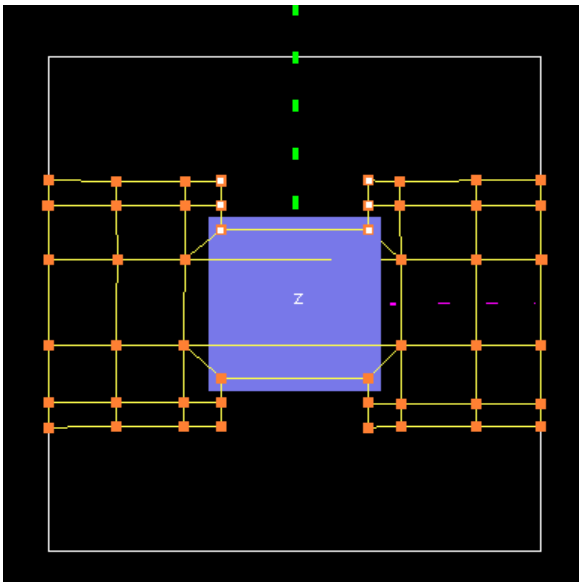

Figure 36: Case A3 topology

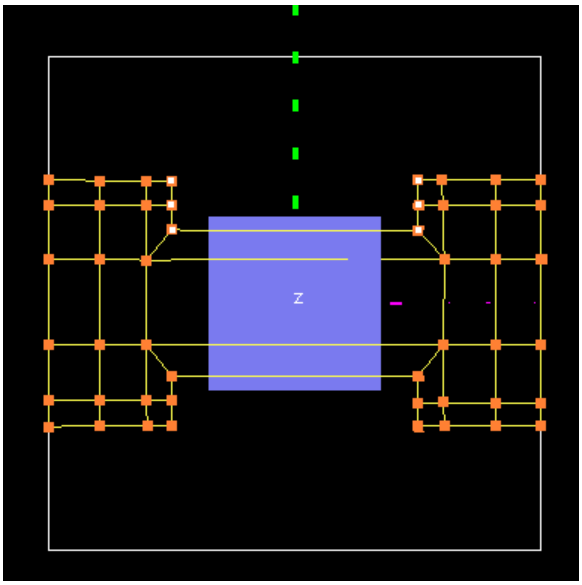

Figure 37: Case A5 Topology

An Eulerian grid is first assembled in GridPro. The Eulerian grid density is assigned in GridPro by assigning a user specified number of cells to each block. The number of cells applied in each coordinate direction at specific regions is described in Table 7. The total number of cells used in the streamwise direction for each case are denoted $\#_x$. The number of cells applied along the height of the rib is denoted $\#_e$, along the rib width, $\#_w$, along the channel half-width $\#_{0.5W}$, and along the channel height $\#_H$. The GridPro grid generation algorithm is run on only the Eulerian grid until the grid is converged. The GridPro algorithm continuously optimizes the mesh quality globally by adjusting the location of cells and does not contain a preconfigured stop command. Instead, the algorithm is allowed to run overnight for each mesh, the Eulerian grids used were in excess of 300,000 iterations of the GridPro algorithm.

Table 7: Mesh density parameters

	Eulerian Grid			After Refinement
Case	$\#_x$	$\#_e$ x $\#_w$	$\#_{0.5W}$ x $\#_H$	$\#_{total}$
A1	212	32x32	80x68	4,730,544
A3	172	32x64	80x72	3,888,312
A5	192	28x80	80x64	3,921,600

Once a suitable Eulerian grid is obtained, the mesh is then refined near the walls where the no-slip boundary conditions are applied. The near wall refinement is performed using GridPro's clustering algorithm. For this study, the same normal wall spacing of 0.00025H and a stretch ratio of 1.10 was used for each wall and for each rib case. The clustering algorithm adds additional cells into the mesh near each wall to achieve the normal wall spacing on the cell closest to the wall and limits the stretch ratio between cells to the user specified value, continuously adding cells until both conditions are satisfied.

The resultant mesh after the clustering step contains more cells than the Eulerian grid, but transitions smoothly from the user specified normal wall spacing towards the Eulerian grid away from the walls. The total number of cells in the final mesh after the grid clustering is listed in the final column of Table 7. The resultant mesh for Case A1 is shown in Figure 38, Figure 39, Figure 40, and Figure 41. Figure 38 depicts the mesh at the channel cross section over the center of the rib. Figure 39 shows the mesh also of the channel cross section but at the periodic interface, at an equal distance between two ribs. The mesh cross section is similar for all three rib cases since they are topologically similar. Figure 40 shows the mesh details at the symmetry plane of the channel for Case A1, Figure 41 also shows the mesh at the same section, but is zoomed in around the region of the rib to show more details of the mesh. Figure 42 and Figure

43 show the details of the mesh at the same locations but for Case A3; Figure 44 and Figure 45 show the details of the mesh at the same locations for Case A5.

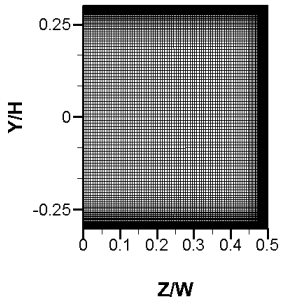

Figure 38: Mesh cross section over ribbed section for Case A1

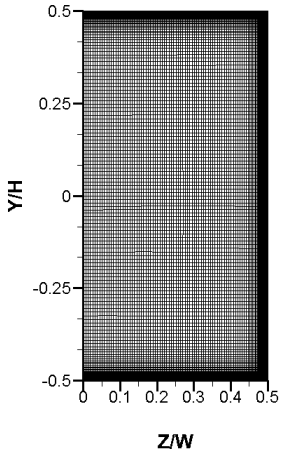

Figure 39: Mesh cross section over non-ribbed section for Case A1

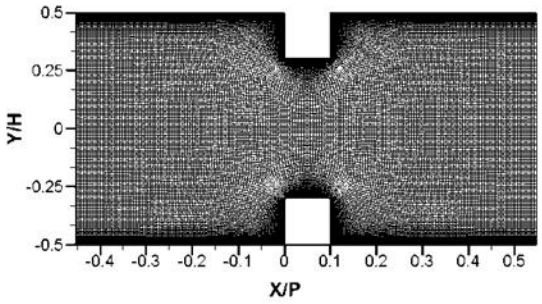

Figure 40: Mesh outline of Case A1 at symmetry plane

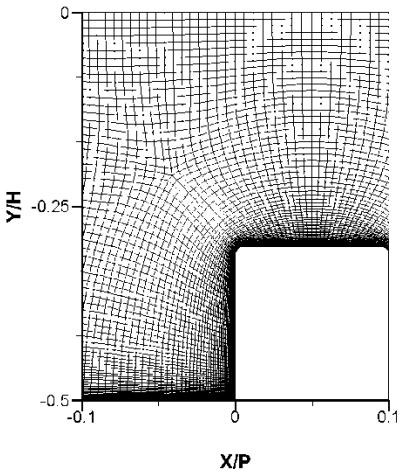

Figure 41: Mesh near rib of Case A1 at symmetry plane

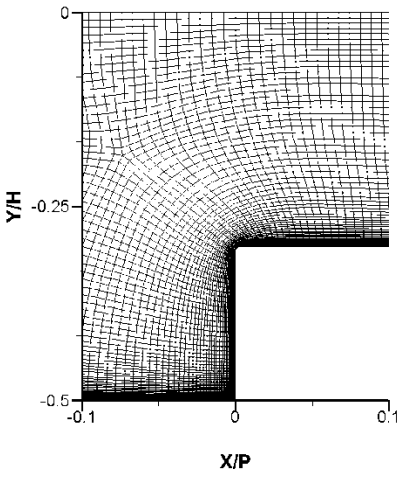

Figure 42: Mesh near rib of Case A3 at symmetry plane

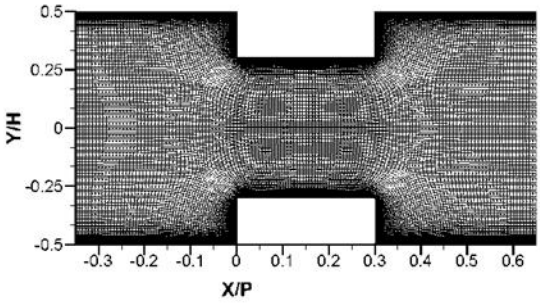

Figure 43: Mesh outline of Case A3 at symmetry plane

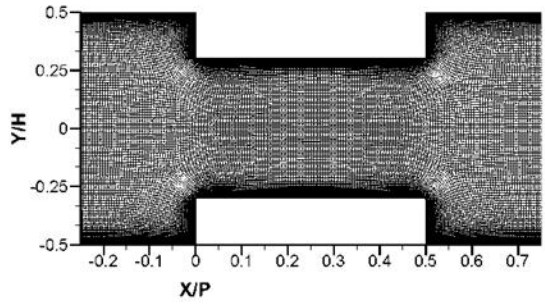

Figure 44: Mesh outline of Case A5 at symmetry plane

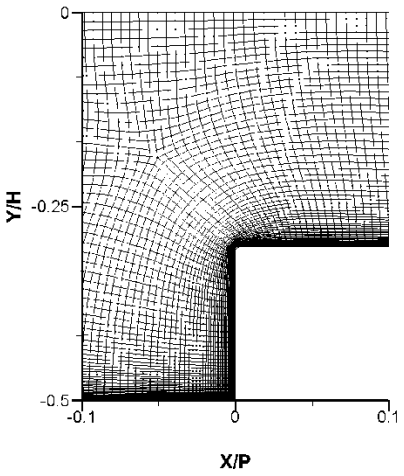

Figure 45: Mesh near rib of Case A5 at symmetry plane

Solution Monitors

Several monitors are defined in Fluent to monitor the solution values after each iteration. The monitors are used to determine solutions quantities at the surface and in the flow. The surface monitor locations correspond to the mid-width of the rib (x/e = 0.5) at the center of the channel (z/W= 0) and at the quarter-span of the channel (z/W = 0.25). The in-flow monitor locations are one rib height downstream of the rib and are also located at the channel mid-span (z/W=0) and quarter-span (z/W=0.25). The actual locations of the monitors for each rib configurations are different because of the differences in rib width, but the relative locations are consistent with the parameters denoted in Table 8. The setup monitors are only necessary to monitor the solution convergence.

Table 8: Monitor locations

Monitor	$\frac{x}{W}$	$\frac{y}{H}$	$\frac{Z}{W}$
1	0.5	0.3016	0
2	0.5	0.3016	0.25
3	0.5	-0.3016	0
4	0.5	-0.3016	0.25
5	1.5	0.3016	0
6	1.5	0.3016	0.25
7	1.5	-0.3016	0
8	1.5	-0.3016	0.25

Solution Strategy

The test matrix of the computational study is given in Table 9. Each rib configuration is tested numerically at 20,000, 30,000, and 40,000, similar to the experimental study.

Table 9: Computational test matrix

Case	Channel Reynolds number		
A1	20,000	30,000	40,000
A3	20,000	30,000	40,000
A5	20,000	30,000	40,000

The computational fluid dynamics study is performed in Fluent. Each mesh generated from GridPro is imported into Fluent directly. The mesh dimensions are also rescaled to match the actual physical dimensions of the channel cross section in the experimental setup so that similar operating conditions can be applied to the numerical simulation as the experimental testing. A steady RANS simulation is performed using the pressure based solver. The realizable k-ϵ turbulence model is used with enhanced wall treatment. A constant density is applied with air as the working fluid. The Simple scheme is used for the pressure-velocity coupling in this study. 2^{nd} order discretization schemes are used for the spatial discretization of the fluxes by utilizing 2^{nd} order upwind schemes for pressure, momentum, turbulence, and energy. The under relaxation are left at their defaults.

Table 10: Properties used in Fluent runs

Property	Value
$\boldsymbol{k_f}$	$0.0242\ \frac{W}{m \cdot \mathrm{K}}$
$\boldsymbol{\rho}$	$1.225\ \frac{kg}{m^3}$
$\boldsymbol{c_p}$	$1006.43\ \frac{J}{kg \cdot \mathrm{K}}$
$\boldsymbol{\mu}$	$1.789 \times 10^{-5} Pa \cdot s$

The symmetry condition is applied at the plane corresponding to the channel half-width (z=0 plane). No-slip boundary conditions are applied to the appropriate surfaces, the rib surfaces, side wall, and top and bottom walls. A uniform wall heat flux is then applied to the no-slip walls in order to provide the heat flux for the calculations of the heat transfer coefficient. Periodic boundary conditions are applied to the channel inlet and exit.

The pressure gradient across the domain can either be specified explicitly or it can be iterated to achieve a desired mass flow rate (or mass flux). In this study, the target mass flow rate approach is used. Even though the pressure gradient is known from experiment, it is not known how accurately the numerical simulation will reproduce the flow physics of the channel. Hence, the mass flow rate is applied to ensure that the numerical simulation will converge to the desired channel Reynolds number. This approach will also allow the channel friction factor from the experiment to be compared directly to the numerical study since the friction will occur at the

same Reynolds number. The inlet bulk temperature is specified as 300 K, although any bulk temperature can be specified.

The wall heat flux and mass flow rate are different for each Reynolds number tested. Table 11 lists the mass-flow rate and heat flux applied for each Reynolds number. The applied boundary conditions are the same for each rib case, since the channel cross section is the same.

Table 11: Boundary conditions at each Reynolds number

	Reynolds Number		
	20,000	**30,000**	**40,000**
Mass flow rate $\frac{kg}{s}$	0.0004295	0.006443	0.00859
Heat flux $\frac{W}{m^2K}$	28360	42540	56720

In order to reduce computational costs, the solution of the flow and energy equations are performed sequentially. After the initialization, only the equations for momentum and turbulence are iterated until a converged solution is obtained, the energy equation is not iterated from the start. Solution convergence is determined by when all the monitored quantities (skin friction coefficient and streamwise velocity) reached asymptotic values, which typically required at least 10,000 iterations. The history of the monitored quantities is provided in Figure 46and Figure 47 for Case A3 at 40,000 Re. The solution behavior as it reaches its asymptotic values is similar for all other cases.

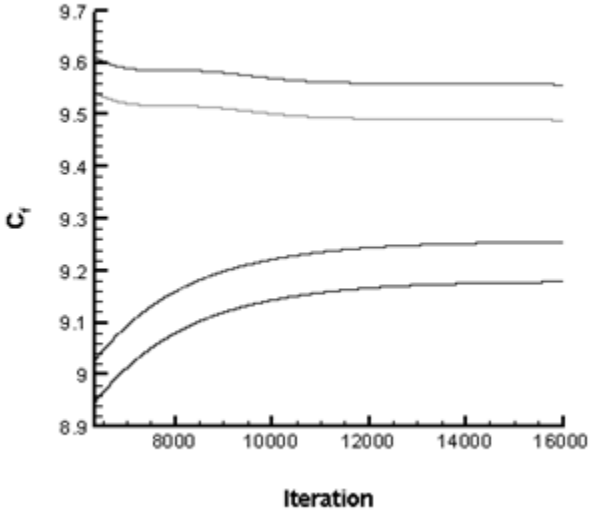

Figure 46: Skin friction coefficient monitors for Case A3 at 40,000 Re

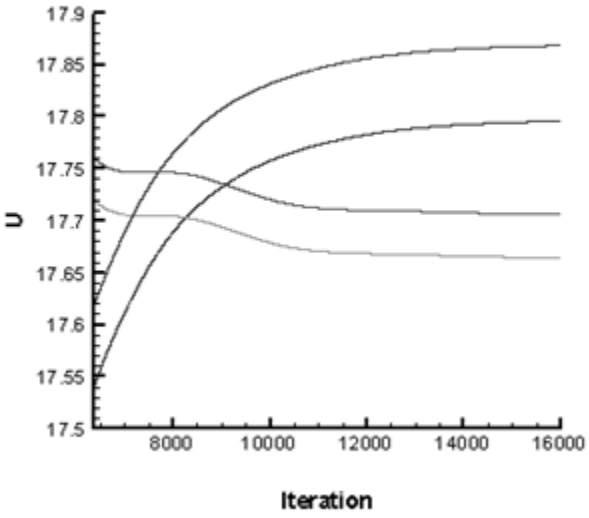

Figure 47: Streamwise velocity monitors for Case A3 at 40,000 Re

Once the momentum and turbulence solutions are converged, their iterations are frozen and disabled. The solver for the energy equation is then activated and then iterated until the monitors also reached asymptotic values (flow temperature and heat transfer coefficient). The history of the monitored quantities for Case A3 at 40,000 Reynolds number is also provided in Figure 48 and Figure 49. The convergence of the energy equation is relatively easy compared to the momentum and turbulence equations, and typically reaches an asymptotic solution within a few hundred iterations, although 1000 iterations were performed for the energy equation alone for all cases studied. Because the energy equation can be solved by itself rather quickly, performing extra iterations for the energy equation and the additional computation cost associated with it were not as much of impediment as extra iterations on the flow and turbulence equations.

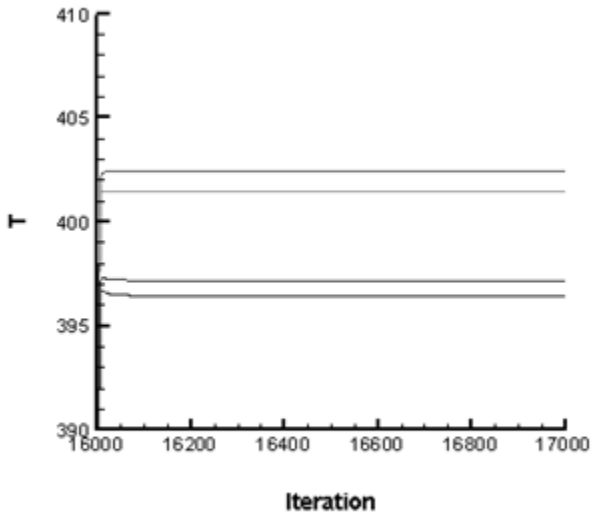

Figure 48: Fluid temperature monitors for Case A3 at 40,000 Re

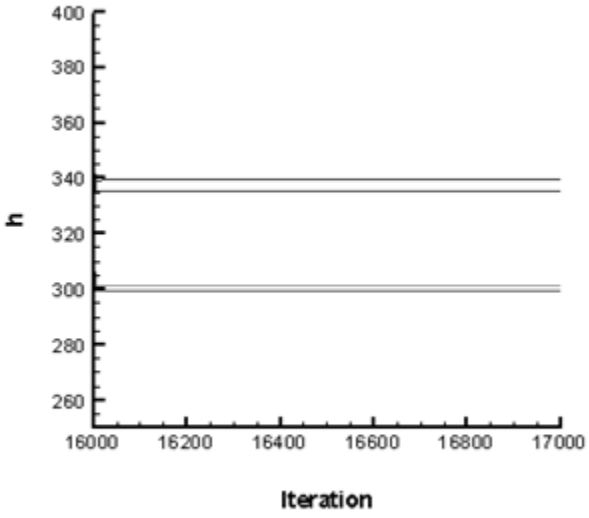

Figure 49: Heat transfer coefficient monitors for Case A3 at 40,000 Re

For a given computational domain, the y^+ values typically only need to be verified for the highest Reynolds number flow rates, since the friction velocity is smaller for lower flow rates (assuming that the local flow conditions do not change dramatically with changes in Reynolds number), the same mesh at a lower friction velocity would result in even lower values of y^+. Usually only one grid point within the viscous sub-layer is considered adequate to apply the linear relation, for cases where only the fluid aerodynamics are of interest. Further resolution near the walls is not warranted because it significantly increases the total cell count and also the computational cost. For an accurate calculation of the wall heat flux however, a very fine grid resolution is necessary near the wall to resolve the wall-normal temperature gradient, which

determines the numerically calculated wall heat flux. Hence a y^+ of less than 1 was desired for this study, since both the flow and heat transfer are of interest.

Computational Results

Wall y^+

The contours of the calculated y^+ at 40,000 Re, the highest Reynolds number tested, are shown for Case A1 Figure 50, for Case A3 in Figure 51, and for Case A5 in Figure 52. The desired condition of $y^+ < 1$ is obtained everywhere. Most of the y^+ values are approximately 0.5 with the highest values of y^+ occurring on the upstream edge of the rib.

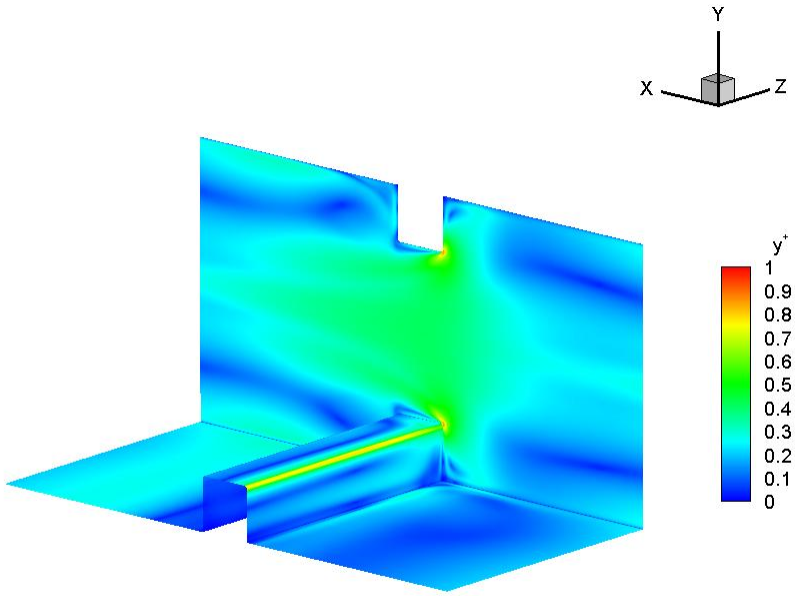

Figure 50: Wall y^+ contours of Case A1 at 40,000 Re

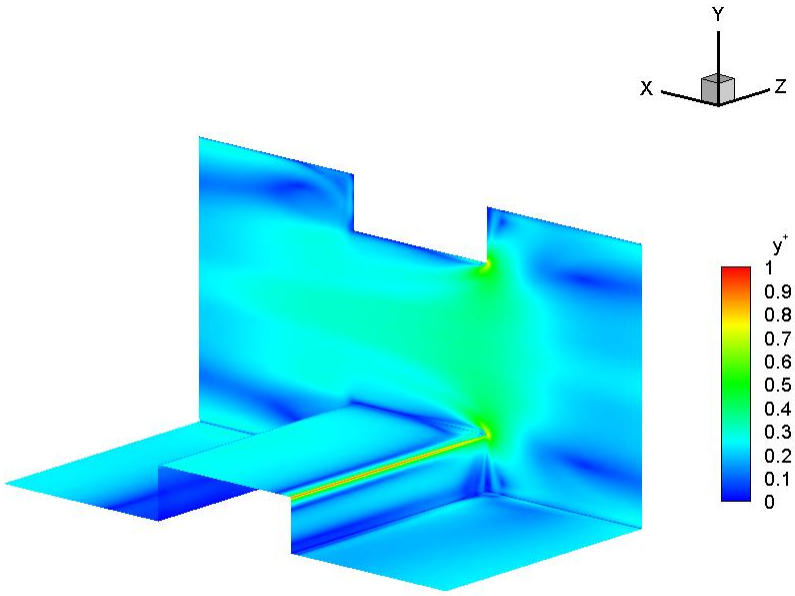

Figure 51: Wall y^+ contours of Case A3 at 40,000 Re

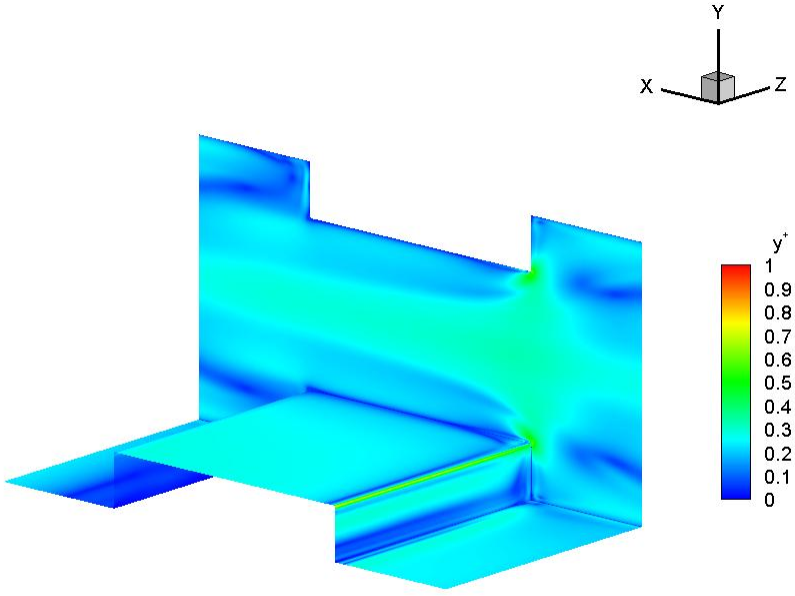

Figure 52: Wall y^+ contours of Case A5 at 40,000 Re

Flow visualization: A1

The local contours of the streamwise velocity at the symmetry plane for Case A1 are shown in Figure 53 for 20,000 Reynolds number, in Figure 54 for 30,000 Reynolds number, and in Figure 55 for 40,000 Reynolds number.

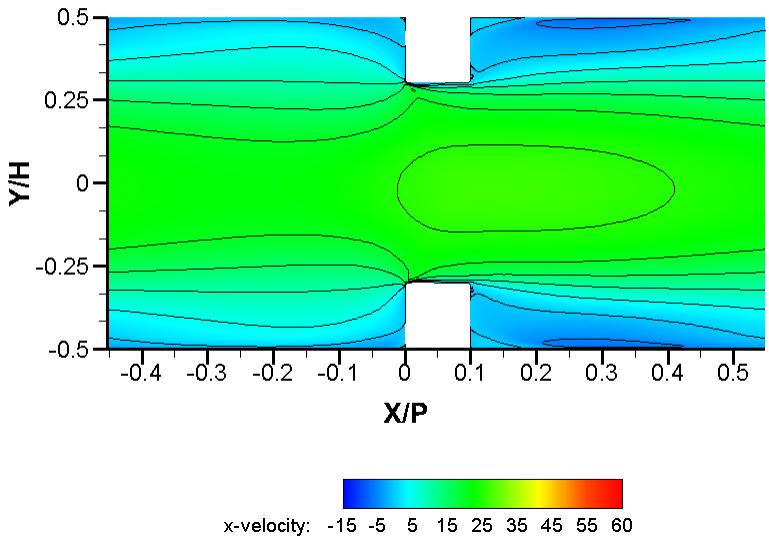

Figure 53: Contours of streamwise velocity at the symmetry plane for Case A1 at 20,000 Re

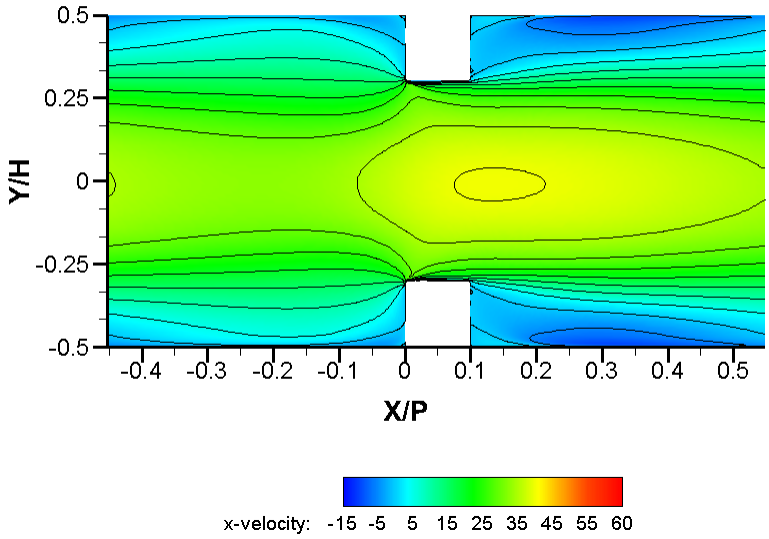

Figure 54: Contours of streamwise velocity at the symmetry plane for Case A1 at 30,000 Re

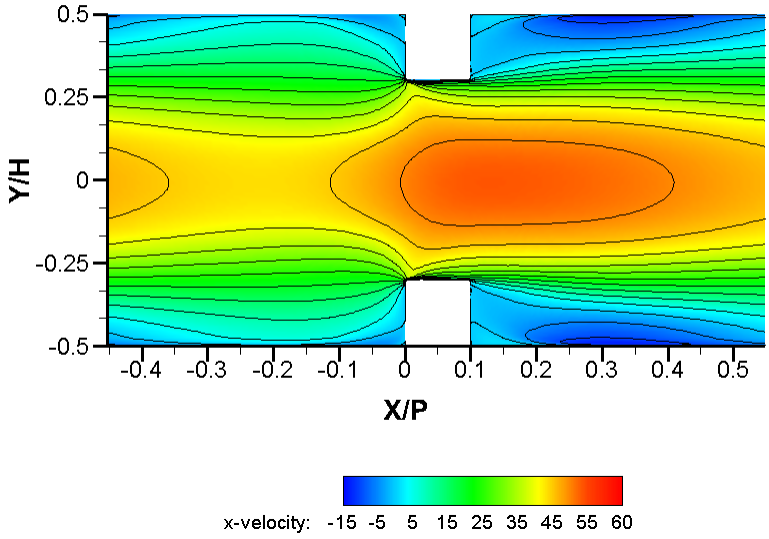

Figure 55: Contours of streamwise velocity at the symmetry plane for Case A1 at 40,000 Re

In Figure 54, Figure 55, and Figure 56, some of the dominant flow features in a ribbed channel can be seen. The increase in the channel bulk velocity corresponds to the increase in channel flow rate and Reynolds number. Downstream of each rib feature, a region of negative streamwise velocity occurs, which occupies a significant portion of the region downstream of the rib. The negative streamwise velocity corresponds to the recirculating flow behind the rib. With increasing Reynolds number, the streamwise velocity behind the rib, and closer to the channel walls, becomes more negative. Although the size of the backward flow region was not found the increase with Reynolds number, the increase in the strength of the backward flow demonstrates the increase in strength or intensity of the recirculating flow behind the rib.

The location at which the streamwise velocity changes sign (backward to forward flow) occurs at a relative location of 5-6 rib heights from the leading edge of the rib, this criteria can be used to determine the location at which the separated flow reattaches on the channel wall. The reattachment location is consistent for all three channel Reynolds numbers tested.

There are also sharp gradients in streamwise velocity near the leading edge of the rib as a result of the flow contraction taking place in the channel. Behind the rib, the streamwise velocity is not reduced immediately as a result of the separation that occurs behind the rib step, which further reduces the effective flow cross section and prevents the flow from expanding to the greater cross sectional area.

The local contours of the normal velocity at the symmetry plane for Case A1 are shown in Figure 56 for 20,000 Reynolds number, in Figure 57 for 30,000 Reynolds number, and in Figure 58 for 40,000 Reynolds number.

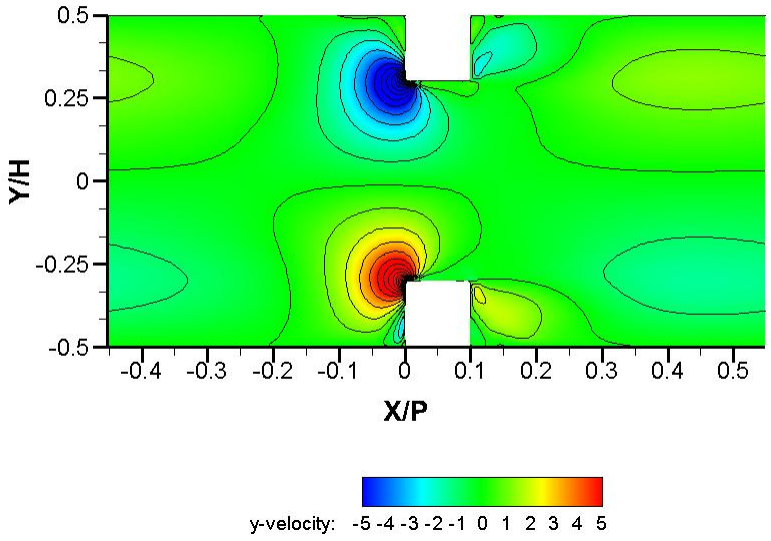

Figure 56: Contours of normal velocity at the symmetry plane for Case A1 at 20,000 Re

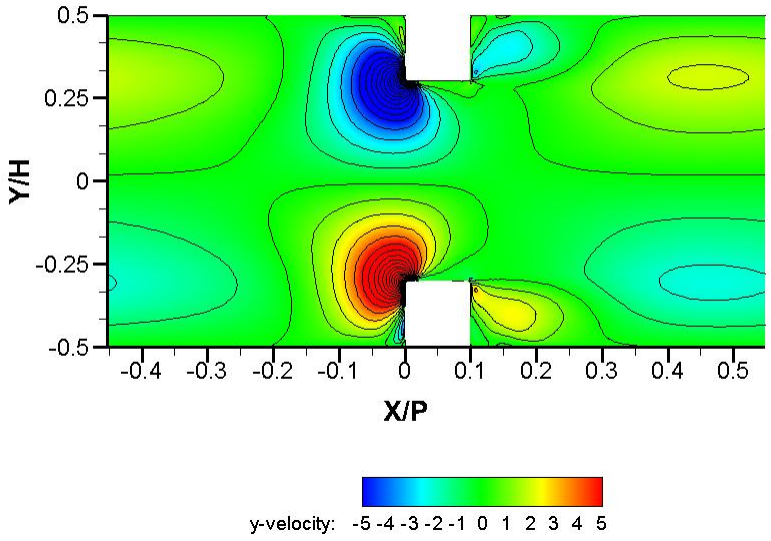

Figure 57: Contours of normal velocity at the symmetry plane for Case A1 at 30,000 Re

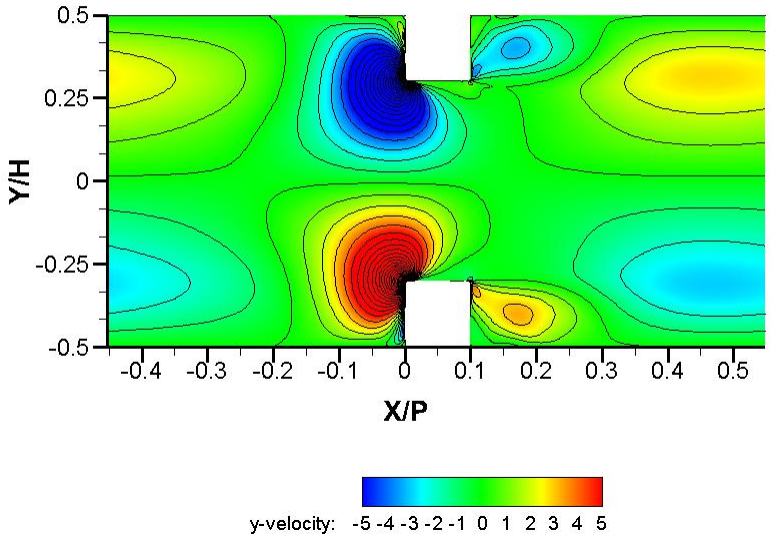

Figure 58: Contours of normal velocity at the symmetry plane for Case A1 at 40,000 Re

At all three channel Reynolds numbers, the characteristics of the normal velocity on the symmetry plane have similar features. Upstream of the rib feature, there is a large region of normal velocities towards the center of the channel. Immediately downstream of the rib feature, rather than towards the channel wall, which is where the normal velocity would point towards if the flow was allowed to expand, instead the normal velocity is also towards the channel center. The normal flow in this region behind the rib is a result of the circulating flow in the back corner of the rib which is entrained by the much larger recirculation region caused by the separated flow behind the rib. The larger recirculation region completes its loop further downstream where the normal velocities point from the channel center towards the channel walls.

The relative sizes of the regions with higher normal velocities increases with increasing Reynolds number. In front of the rib, the increase in normal velocity is a result of the rapid

contraction of the faster moving fluid with increasing Reynolds number and flow rate. As the flow rate is increased, more flow has to squeeze between the ribs. Immediately downstream of the rib, the magnitude of the normal velocity also increases with increasing Reynolds number. Even further downstream, the magnitude of the normal velocity towards the channel wall also increased with increasing Reynolds number. The increase in the normal velocity in these regions behind the rib helps to support the trend of increased strength of the recirculation region with increasing Reynolds number, which was deduced from the streamwise velocity magnitudes. Like the streamwise velocity, the locations of the normal velocities pointing toward the channel centerline or toward the channel wall do not change with Reynolds number, but they do change in size, magnitude, and strength.

A local plot of the absolute velocity vectors at the symmetry plane for Case A1 are shown in Figure 59 for 20,000 Reynolds number, in Figure 60 for 30,000 Reynolds number, and in Figure 61 for 40,000 Reynolds number. The vector lengths are uniformly set and do not correspond to velocity magnitudes. The contours are colored by absolute velocity magnitude.

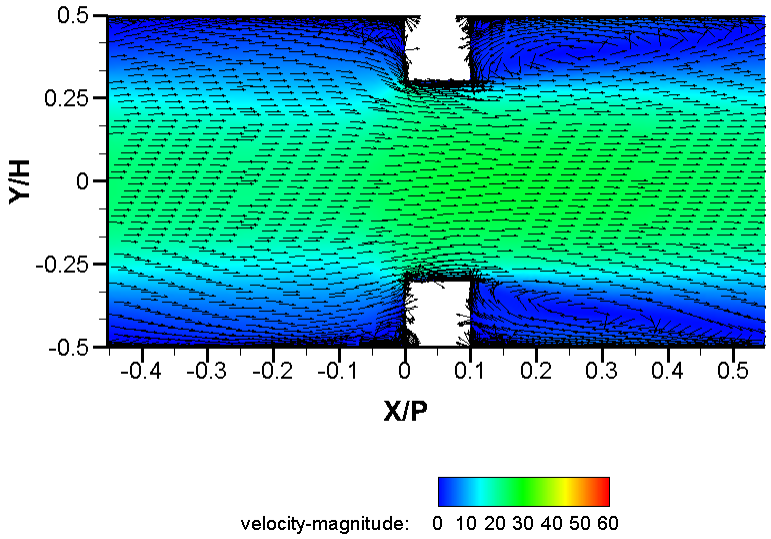

Figure 59: Vector plot of absolute velocity at the symmetry plane for Case A1 at 20,000 Re

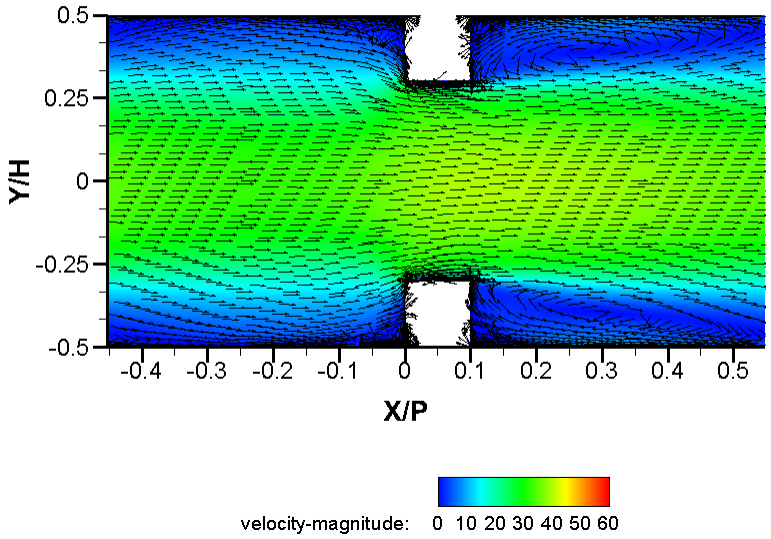

Figure 60: Vector plot of absolute velocity at the symmetry plane for Case A1 at 30,000 Re

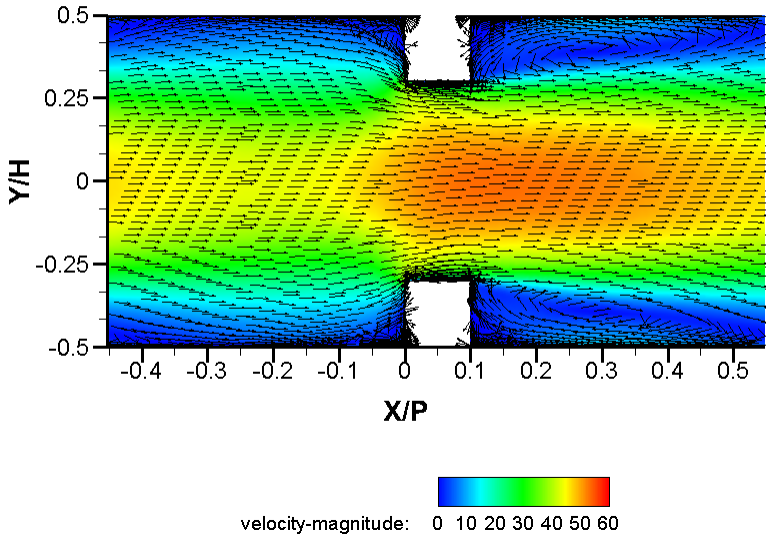

Figure 61: Vector plot of absolute velocity at the symmetry plane for Case A1 at 30,000 Re

The local vectors further demonstrate the characteristics discussed thus far from examining the streamwise and normal velocity components. The flow must accelerate rapidly as it passes in between the blockage caused by the ribs. After the rib, the flow cannot expand immediately and a separated flow occurs. The flow reattaches much further downstream and a recirculation region develops underneath the separated shear layer because of the flow entrainment. This primary recirculation zone also entrains a smaller recirculation region in the corners between the rib trailing edge and channel wall. The reattachment location can be better visualized with the absolute velocity magnitudes and velocity vectors plotted. The reattachment location is also observed to occur consistently in the range of a 5-6 rib heights for all three channel Reynolds numbers.

As a result of the increased strength of the backward flow from the increased magnitudes of the streamwise velocity with increasing Reynolds number, and also the increased magnitudes of the normal velocity with increasing Reynolds number, the size of the primary recirculation zone does not increase with Reynolds number and the flow reattachment location does not change its position. However, the blockage effect of the ribs and the separated flow behind the rib can be seen in the increasing velocity magnitudes nearer the center of the channel at higher Reynolds numbers. The faster moving fluid in this region of the channel does not contribute to any near wall mixing and does not provide any additional heat transfer enhancement at higher Reynolds numbers and is consistent with the decreasing Nusselt number augmentation with increasing Reynolds numbers typically found for ribbed channels.

A plot of the local turbulence intensity percentage at the symmetry plane for Case A1 are shown in Figure 62 for 20,000 Reynolds number, in Figure 63 for 30,000 Reynolds number, and in Figure 64 for 40,000 Reynolds number. The contours are colored by local turbulence intensity percentage.

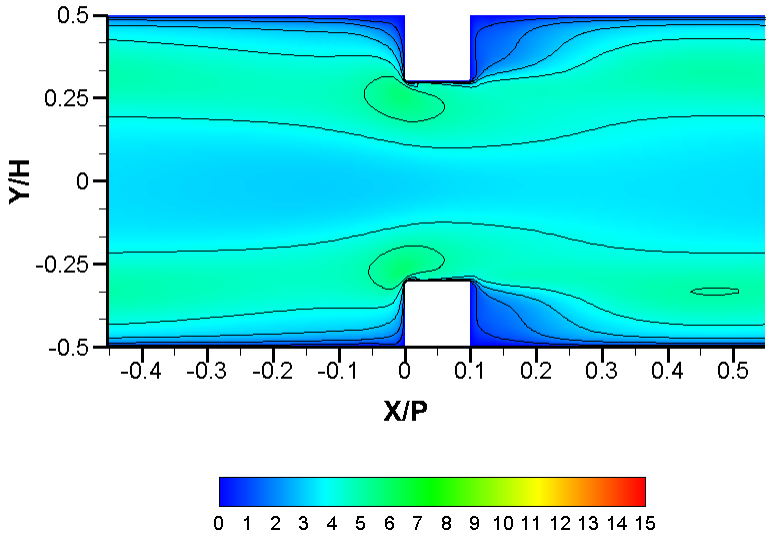

Figure 62: Turbulence intensity at the symmetry plane for Case A1 at 20,000 Re

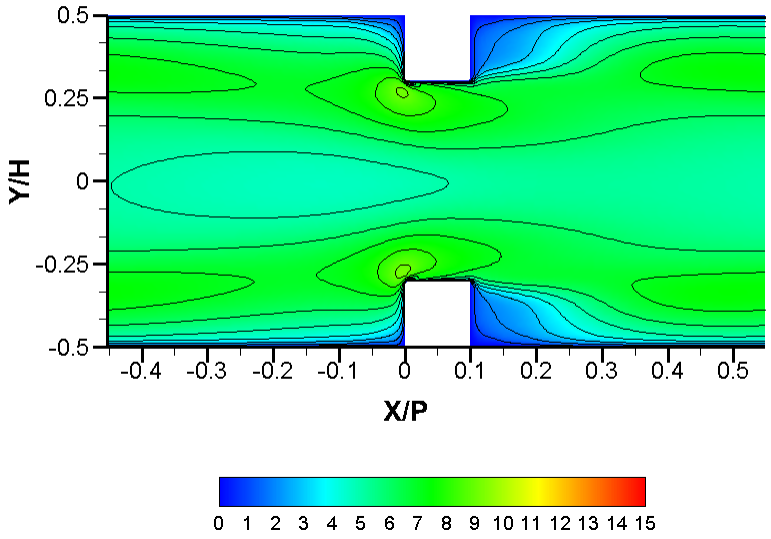

Figure 63: Turbulence intensity at the symmetry plane for Case A1 at 30,000 Re

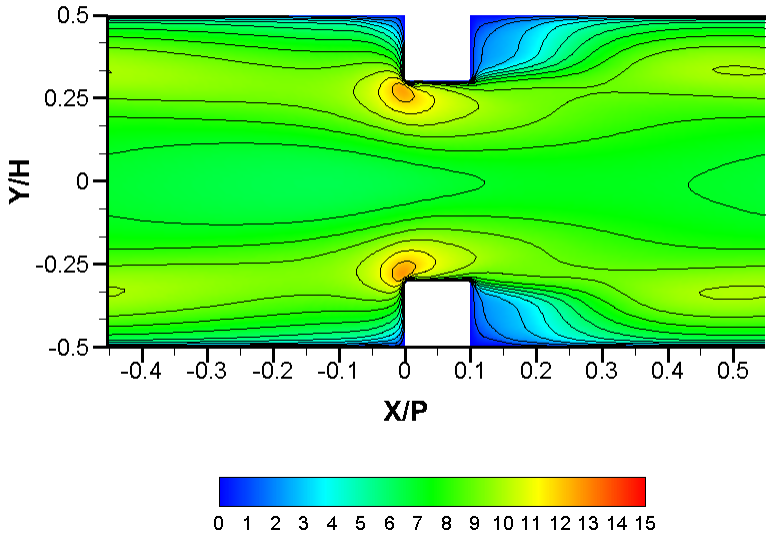

Figure 64: Turbulence intensity at the symmetry plane for Case A1 at 40,000 Re

The turbulence intensity percentage increases tremendously and globally with increasing Reynolds numbers. The turbulence intensity is directly related to the turbulent velocity fluctuations or normalized turbulent kinetic energy. The highest levels of turbulence intensities occur near the upstream edge of the rib. The turbulence intensity is lowest immediately behind the rib in the secondary recirculation. The remaining regions of increased turbulence intensity are well correlated with the reattaching flow; the turbulent kinetic energy in these regions is even higher than near the channel centerline. The additional kinetic energy is generated by the separated shear layer behind the rib which promotes the shear layer growth and eventual reattachment on the channel wall downstream of the rib.

Flow visualization: A3

The local contours of the streamwise velocity at the symmetry plane for Case A3 are shown in Figure 65 for 20,000 Reynolds number, in Figure 66 for 30,000 Reynolds number, and in Figure 67 for 40,000 Reynolds number.

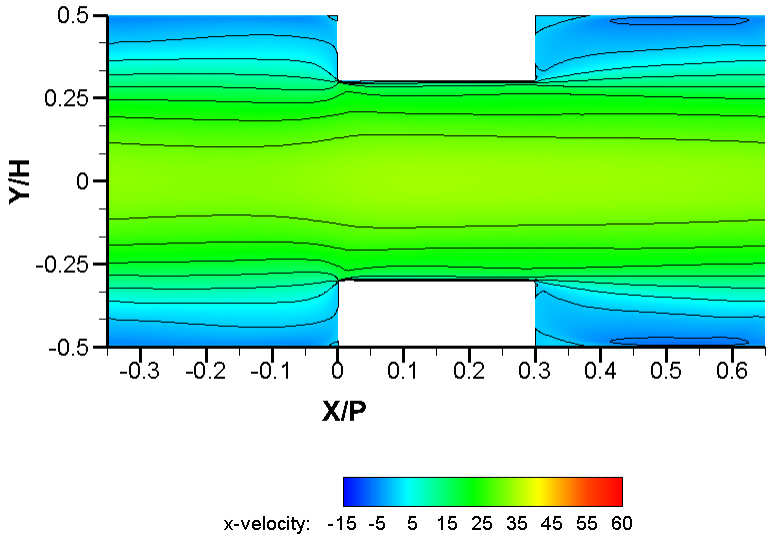

Figure 65: Contours of streamwise velocity at the symmetry plane for Case A3 at 20,000 Re

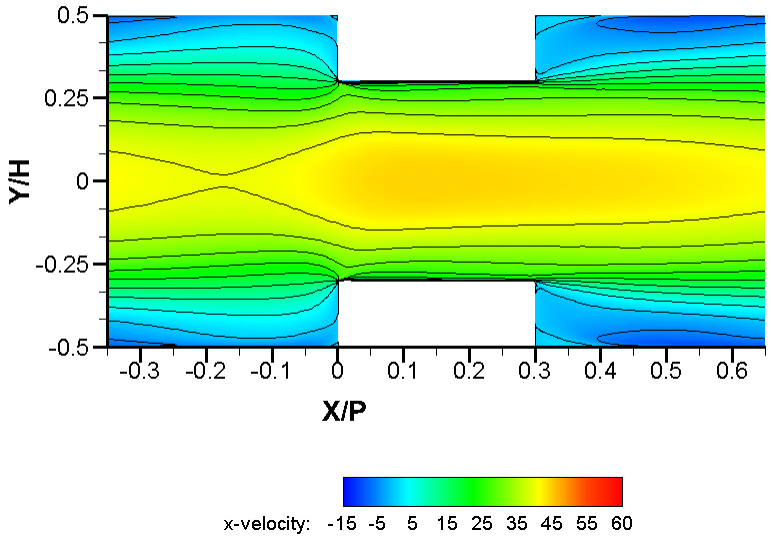

Figure 66: Contours of streamwise velocity at the symmetry plane for Case A3 at 30,000 Re

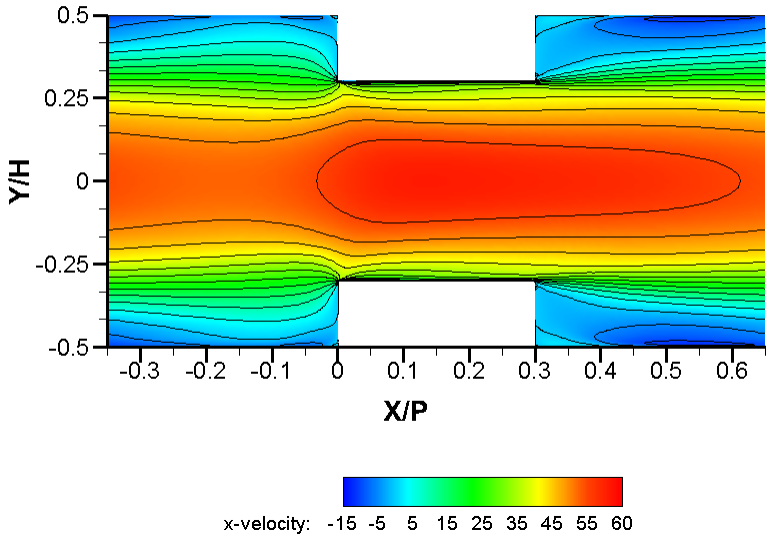

Figure 67: Contours of streamwise velocity at the symmetry plane for Case A3 at 40,000 Re

Case A3 exhibits similar trends to the square ribs case. Downstream of each rib feature, a region of negative streamwise velocity occurs, which occupies a significant portion of the region downstream of the rib. The negative streamwise velocity corresponds to the recirculating flow behind the rib. With increasing Reynolds number, the streamwise velocity behind the rib, and closer to the channel walls, becomes more negative. Although the size of the backward flow region was not found the increase with Reynolds number, the increase in the strength of the backward flow demonstrates the increase in strength or intensity of the recirculating flow behind the rib.

On the other hand there are also some notable differences between Case A3 and A1. Relative to Case A1, the core of the flow does not expand as much after the rib, which can be seen from the larger size of the high velocity region in the core of the flow immediately upstream of the rib for all three Reynolds numbers of Case A3. The reattachment location is also delayed further downstream to a relative distance of 7-8 rib heights downstream of the start of the rib.

At each Reynolds number, the streamwise velocity near the center of the channel is consistently higher for Case A3 compared to Case A1, even though these channels are operating at the same flow rate; more of the flow resides in the core for the wider rib. The wider ribbed channels favors more flow away from the channel walls which weakens any interactions that might take place near the channel walls to improve mixing, since a greater amount of the flow's bulk kinetic energy and momentum is held in the core of the fluid flow.

The local contours of the normal velocity at the symmetry plane for Case A3 are shown in Figure 68 for 20,000 Reynolds number, in Figure 69 for 30,000 Reynolds number, and in Figure 70 for 40,000 Reynolds number.

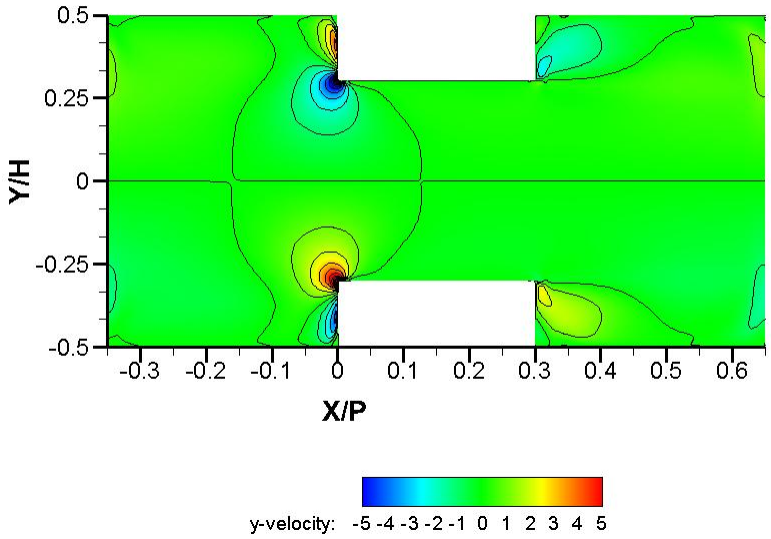

Figure 68: Contours of normal velocity at the symmetry plane for Case A3 at 20,000 Re

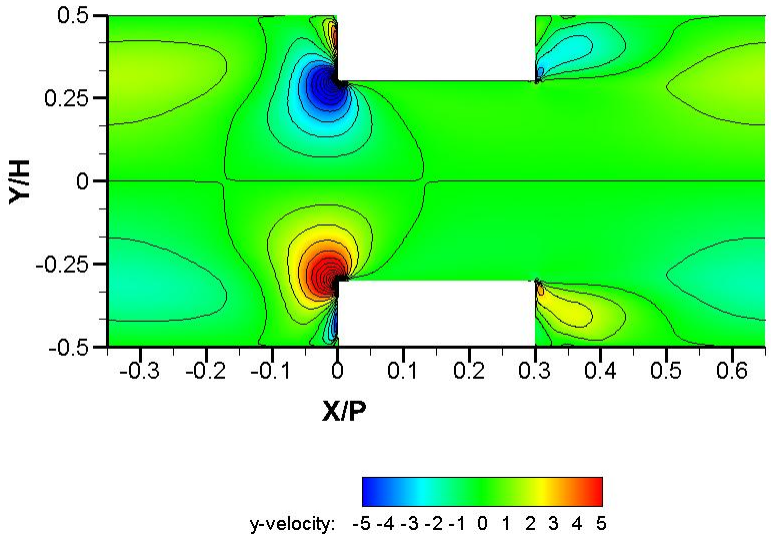

Figure 69: Contours of normal velocity at the symmetry plane for Case A3 at 30,000 Re

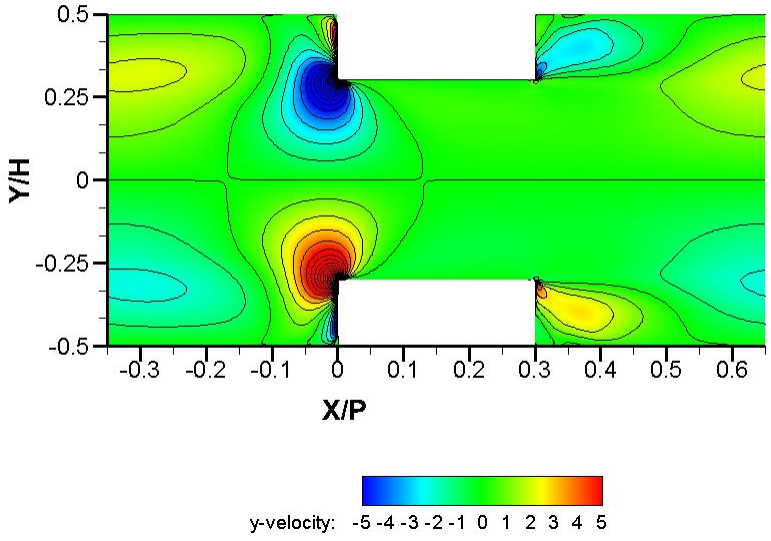

Figure 70: Contours of normal velocity at the symmetry plane for Case A3 at 40,000 Re

At all three channel Reynolds numbers, the characteristics of the normal velocity on the symmetry plane for Case A3 also have similar features. Upstream of the rib feature, there is a large region of normal velocities towards the center of the channel. In addition to the large region of normal velocity directed towards the channel center, there is also a small region in the corner between the rib and the channel wall where the normal velocity is towards the channel wall. The appearance of this feature corresponds to an additional smaller recirculation zone which is induced by the rapidly contracting flow in front of the rib. A small recirculation zone at this location was also observed for the square ribs case, but not as distinct as the 3:1 aspect ratio ribs because the flow was previously dominated by the contraction effects. For the wider 3:1 aspect ratio ribs, the contraction effects are much weaker, the size of the regions of the toward-center normal velocities are consistently smaller for Case A3 than Case A1 at all three Reynolds numbers.

The most visible difference between the normal velocities for Case A3, compared to Case A1, is in the reduced size of the contraction induced effects. Immediately downstream of the rib and further downstream where the flow reattaches, the flow is similar for both rib cases, with the normal velocities for Case A3 weaker than the corresponding ones for Case A1, at all three channel Reynolds numbers.

A local plot of the absolute velocity vectors at the symmetry plane for Case A3 are shown in Figure 71 for 20,000 Reynolds number, in Figure 72 for 30,000 Reynolds number, and in Figure 73 for 40,000 Reynolds number. The vector lengths are uniformly set and do not correspond to velocity magnitudes. The contours are colored by absolute velocity magnitude.

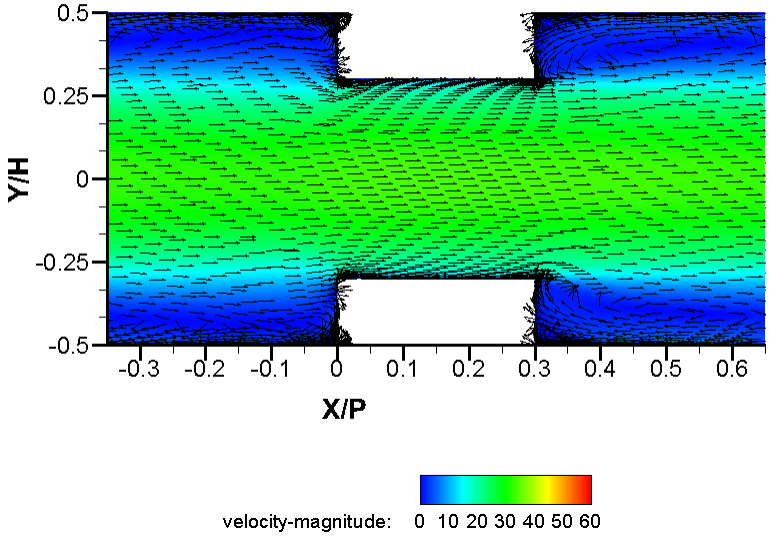

Figure 71: Vector plot of absolute velocity at the symmetry plane for Case A3 at 20,000 Re

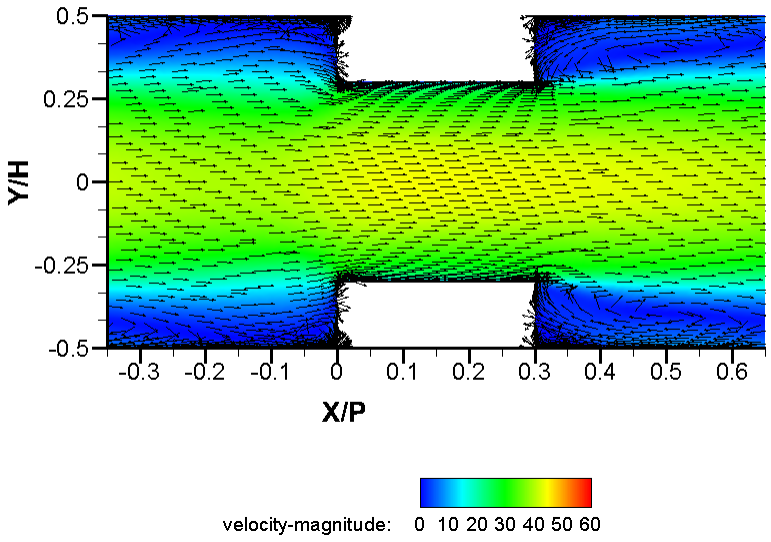

Figure 72: Vector plot of absolute velocity at the symmetry plane for Case A3 at 30,000 Re

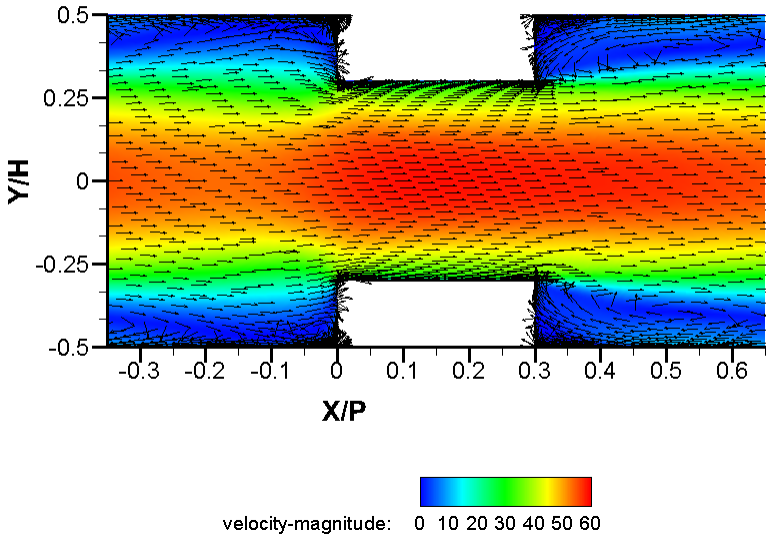

Figure 73: Vector plot of absolute velocity at the symmetry plane for Case A3 at 40,000 Re

Similar to the square ribs case, for Case A3, the size of the primary recirculation zone does not increase with Reynolds number and the flow reattachment location does not change its position. The blockage effect of the ribs and the separated flow behind the rib can be seen in the increasing velocity magnitudes nearer the center of the channel at higher Reynolds numbers.

The reattachment location is seen to occur at approximately 8 rib heights downstream of the start of the rib, further downstream than the reattachment location for the square ribs. With an increase in Reynolds number, the channel velocity does not increase at channel heights below the rib height, the increase in channel velocity mostly occurs towards the center of the channel. The reattachment induced by the wider ribs is not as strong as the smaller, square ribs; the wider ribs also shield the fluid in between two consecutive ribs from changes mainstream flow. The larger recirculation zone also prevents the flow behind the rib from expanding and further restricts the

mainstream flow towards the center of the channel and results in the disproportionate increase in channel velocity towards the channel center.

A plot of the local turbulence intensity percentage at the symmetry plane for Case A3 are shown in Figure 74 for 20,000 Reynolds number, in Figure 75 for 30,000 Reynolds number, and in Figure 76 for 40,000 Reynolds number. The contours are colored by local turbulence intensity percentage.

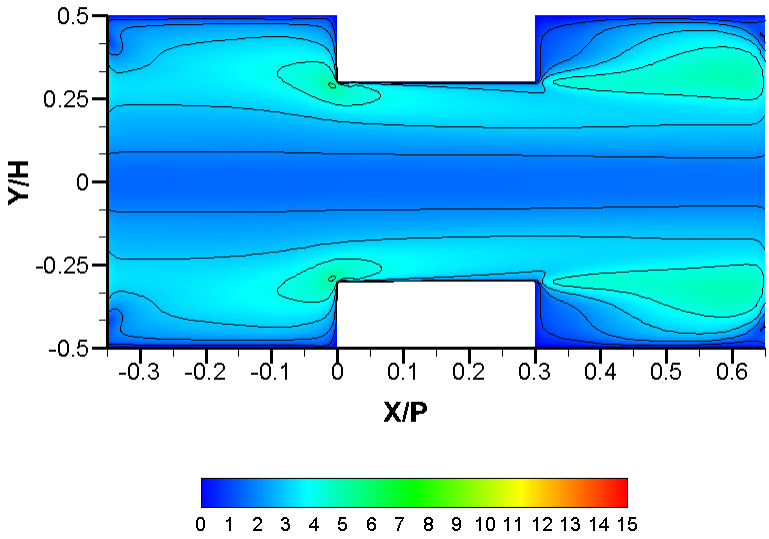

Figure 74: Turbulence intensity at the symmetry plane for Case A3 at 20,000 Re

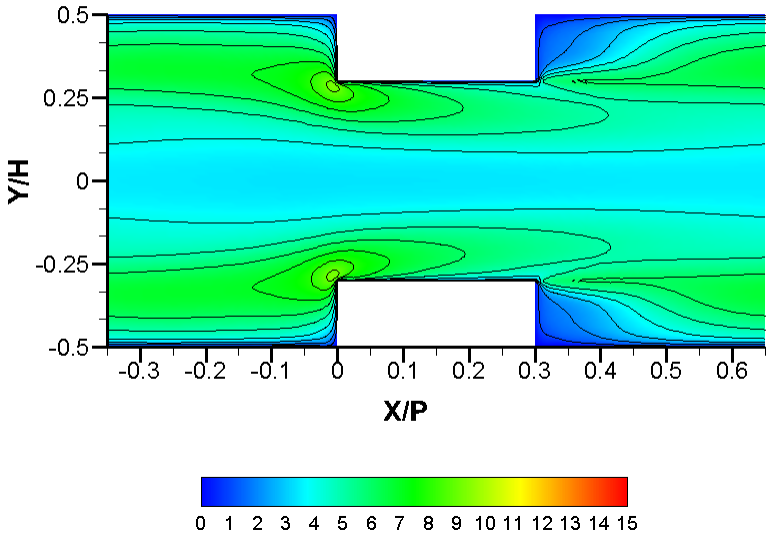

Figure 75: Turbulence intensity at the symmetry plane for Case A3 at 30,000 Re

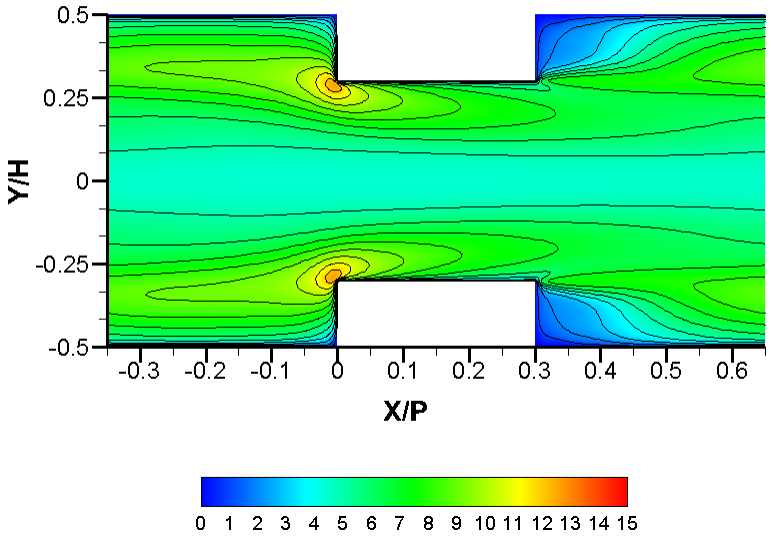

Figure 76: Turbulence intensity at the symmetry plane for Case A3 at 40,000 Re

The local distribution of turbulence intensity for Case A3 is nearly identical to the square ribs case. The turbulence intensity percentage increases globally with increasing Reynolds numbers. The highest levels of turbulence intensities occur near the upstream edge of the rib. The turbulence intensity is also lowest immediately behind the rib in the secondary recirculation. The turbulence intensity at the center of the channel is also lower than near the separated shear layer. However, the actual magnitude, or percentage, of the turbulence intensity level is lower overall for the 3:1 aspect ratio rib case compared to the 1:1 aspect ratio rib case for all three channel Reynolds number. The lower turbulence intensity also reflects the weaker shear layer growth for the 3:1 aspect ratio rib case, which resulted in the weaker and delayed reattachment location further downstream compared to Case A1.

Flow visualization: A5

The local contours of the streamwise velocity at the symmetry plane for Case A5 are shown in Figure 77 for 20,000 Reynolds number, in Figure 78 for 30,000 Reynolds number, and in Figure 79 for 40,000 Reynolds number.

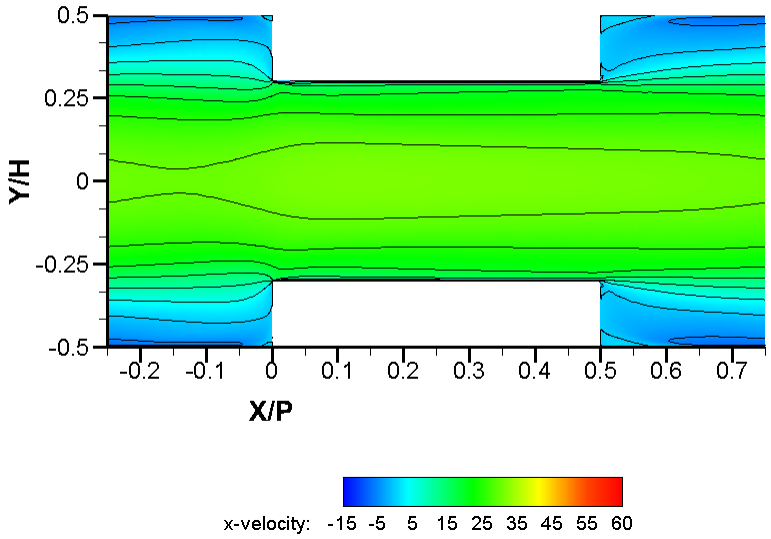

Figure 77: Contours of streamwise velocity at the symmetry plane for Case A5 at 20,000 Re

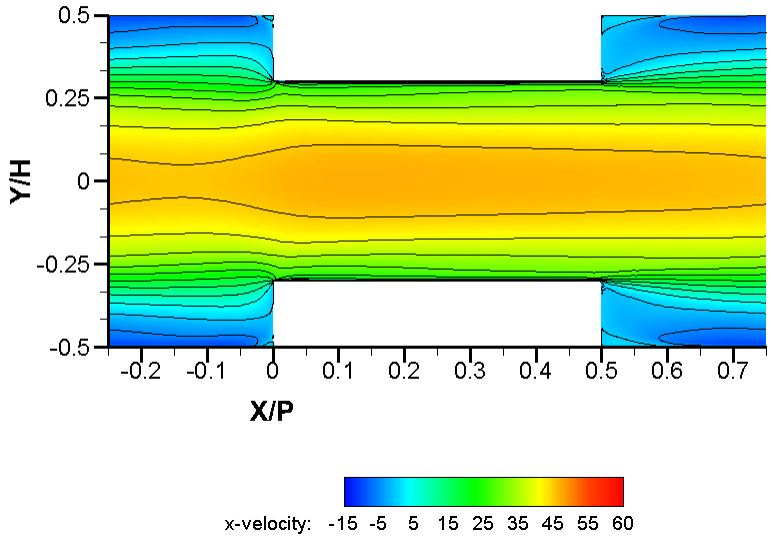

Figure 78: Contours of streamwise velocity at the symmetry plane for Case A5 at 30,000 Re

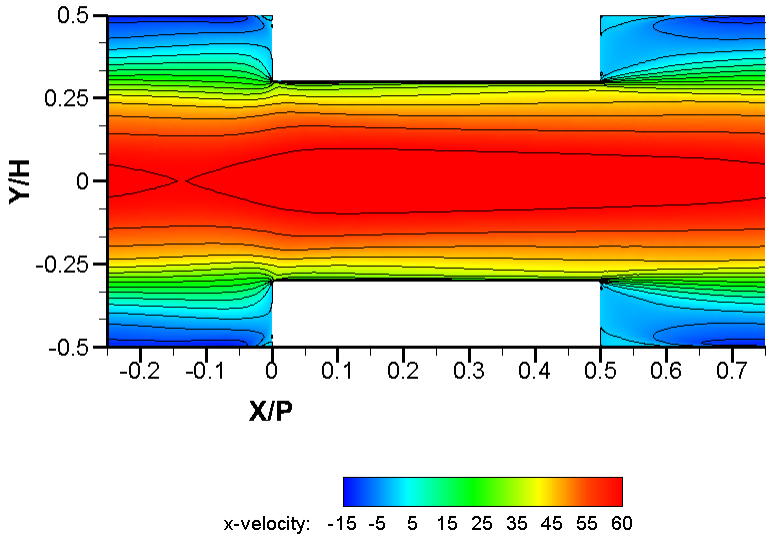

Figure 79: Contours of streamwise velocity at the symmetry plane for Case A5 at 40,000 Re

Unlike the two previous rib cases, for the 5:1 aspect ratio rib case, the region in between two consecutive ribs is completely dominated by reversed flow for each Reynolds number studied. A reattachment location is not observed. Instead the flow impingements on the leading edge of the rib. The strength of the reversed flow also increases with increasing Reynolds number from the increased entrainment of the mainstream flow.

Similar to the 3:1 aspect ratio ribs case, at each Reynolds number, the widest rib case favors more flow away from the channel walls and retains the faster moving fluid closer to the channel center. The highest magnitude of streamwise velocity was found on the highest Reynolds number case for the 5:1 rib aspect ratio configuration at the channel centerline, higher than the 3:1 and 1:1 aspect ratio rib cases.

The local contours of the normal velocity at the symmetry plane for Case A5 are shown in Figure 80 for 20,000 Reynolds number, in Figure 81 for 30,000 Reynolds number, and in Figure 82 for 40,000 Reynolds number.

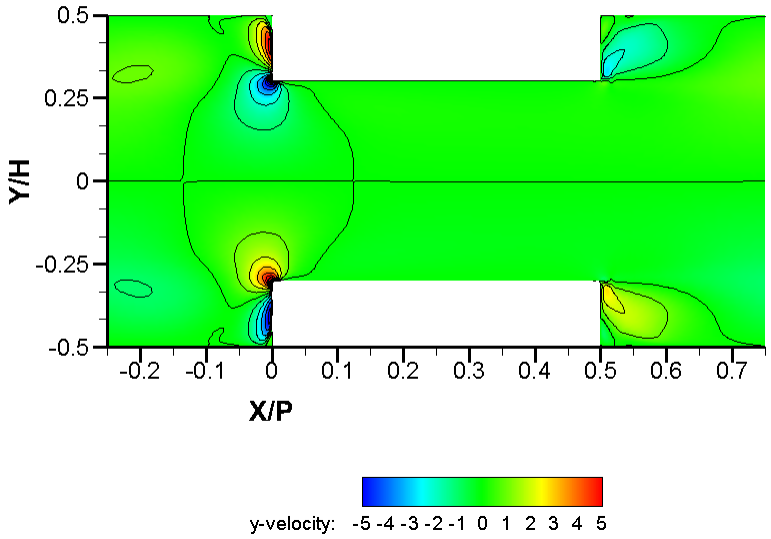

Figure 80: Contours of normal velocity at the symmetry plane for Case A5 at 20,000 Re

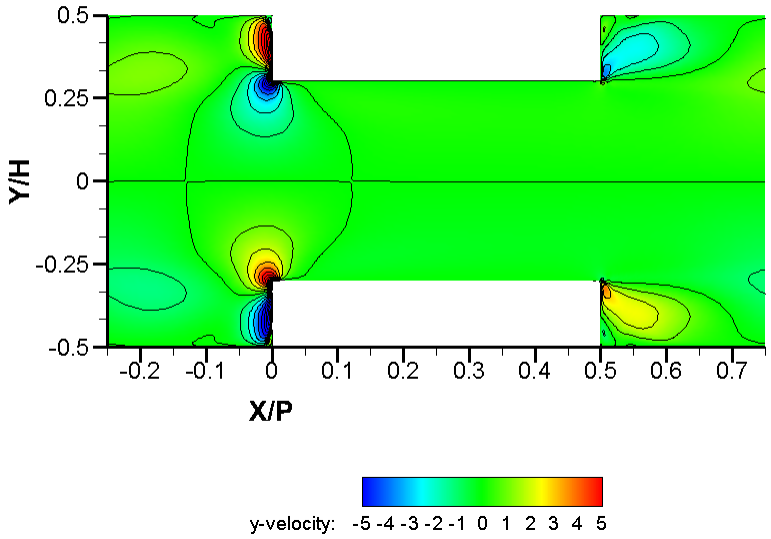

Figure 81: Contours of normal velocity at the symmetry plane for Case A5 at 30,000 Re

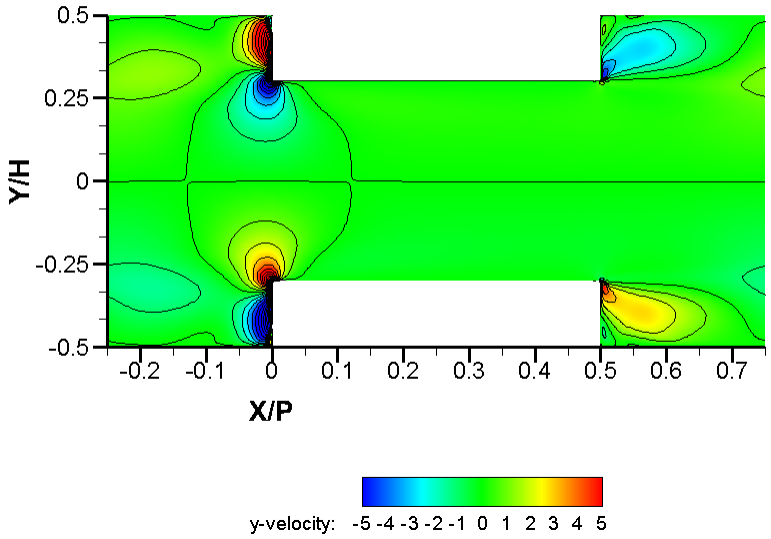

Figure 82: Contours of normal velocity at the symmetry plane for Case A5 at 40,000 Re

The trends in normal velocity for Case A5 are similar in most aspects to Case A3 and Case A1. The strength of the secondary recirculation region upstream of the rib is further increased for the 5:1 aspect ratio rib case. The size of the normal velocity towards the channel walls actually exceeds the region of the normal velocity towards the channel center caused by the contraction effects induced by the rib; the effects of the rib-induced contraction are further weakened for the 5:1 rib aspect ratio case, a trend also observed for the 3:1 aspect ratio rib case compared to the 1:1 aspect ratio ribs. Increasing the rib width weakens the overall strength of the contraction effect induced by the rib, while at the same time also increases the strength of the secondary recirculation upstream of the rib.

A local plot of the absolute velocity vectors at the symmetry plane for Case A5 are shown in Figure 83 for 20,000 Reynolds number, in Figure 84 for 30,000 Reynolds number, and in Figure 85 for 40,000 Reynolds number. The vector lengths are uniformly set and do not correspond to velocity magnitudes. The contours are colored by absolute velocity magnitude.

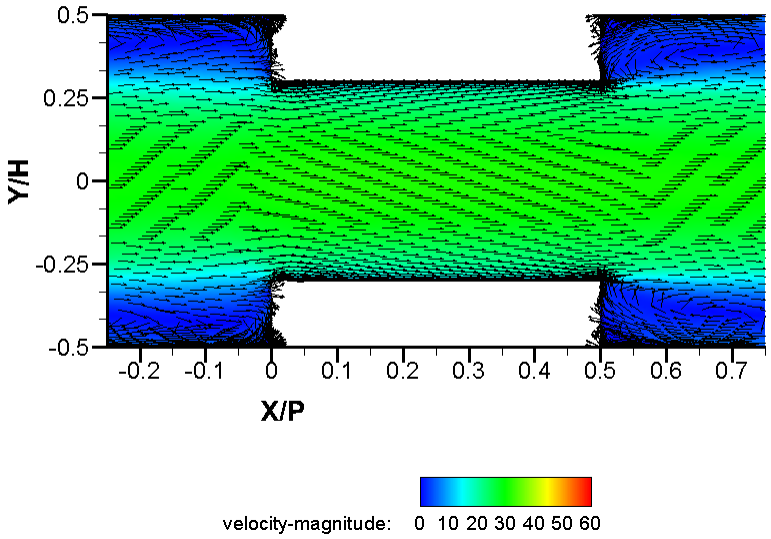

Figure 83: Vector plot of absolute velocity at the symmetry plane for Case A5 at 20,000 Re

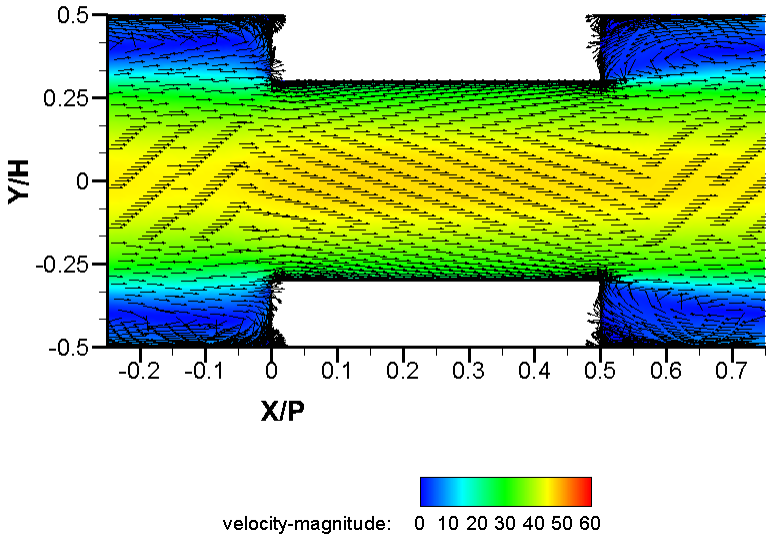

Figure 84: Vector plot of absolute velocity at the symmetry plane for Case A5 at 30,000 Re

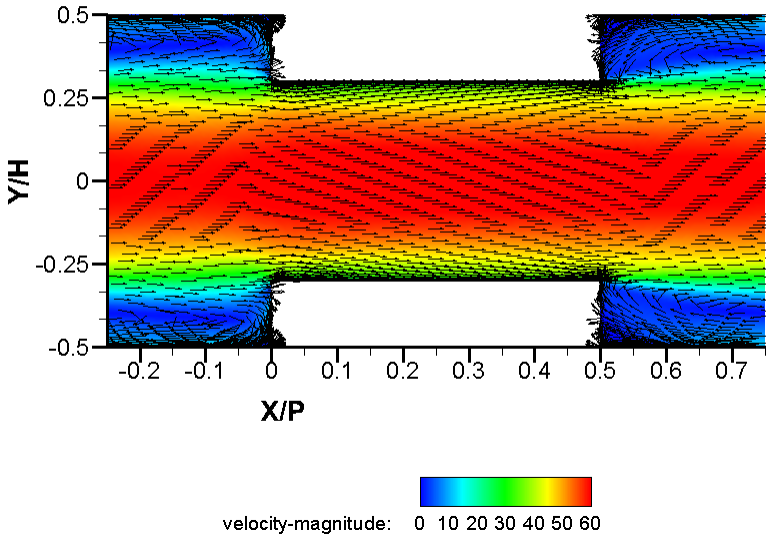

Figure 85: Vector plot of absolute velocity at the symmetry plane for Case A5 at 40,000 Re

The local velocity vectors for the 5:1 rib aspect ratio case further support some of the trends found thus far. For the 5:1 rib aspect ratio case, the flow does not reattach downstream of the rib. Instead, the flow impinges on the upstream edge of the following rib and bifurcates, part of the flow entering the recirculation region and part of the flow passes over the rib. With an increase in Reynolds number, the channel velocity does not increase at channel heights below the rib height, the increase in channel velocity mostly occurs towards the center of the channel. The larger recirculation zone also prevents the flow behind the rib from expanding and further restricts the mainstream flow towards the center of the channel and results in the disproportionate increase in channel velocity towards the channel center, even more pronounced than had occurred for Case A3.

A plot of the local turbulence intensity percentage at the symmetry plane for Case A5 are shown in Figure 86 for 20,000 Reynolds number, in Figure 87 for 30,000 Reynolds number, and in Figure 88 for 40,000 Reynolds number. The contours are colored by local turbulence intensity percentage.

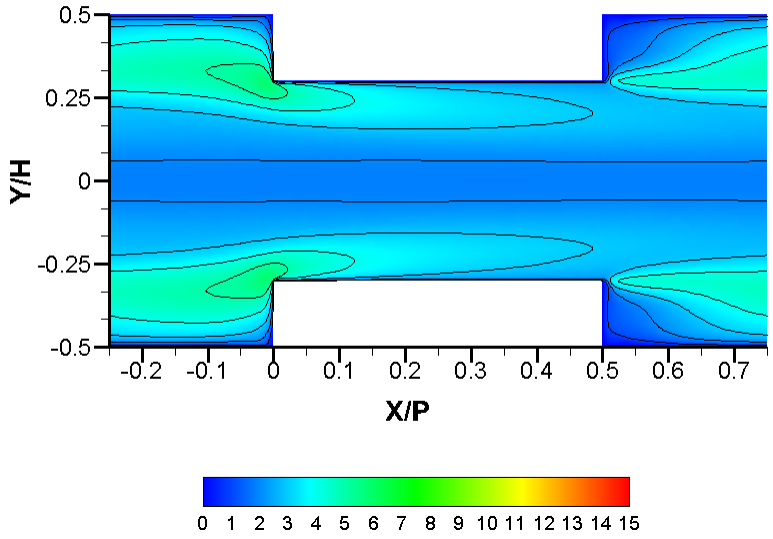

Figure 86: Turbulence intensity at the symmetry plane for Case A5 at 20,000 Re

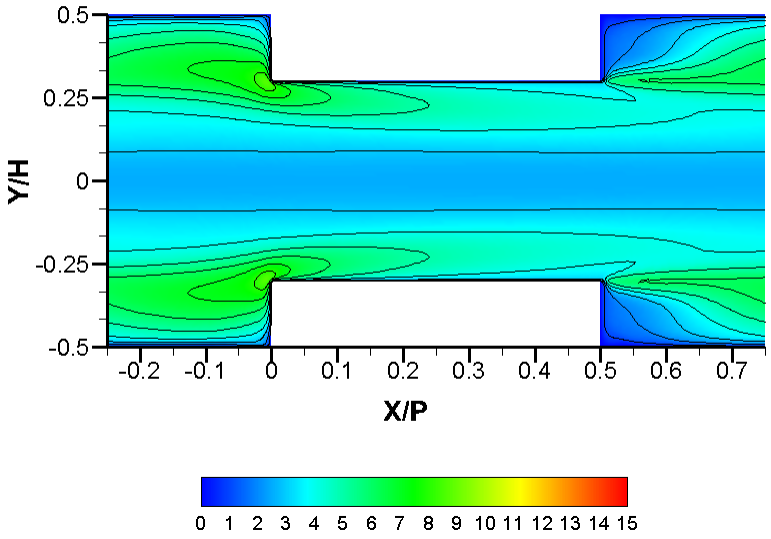

Figure 87: Turbulence intensity at the symmetry plane for Case A5 at 30,000 Re

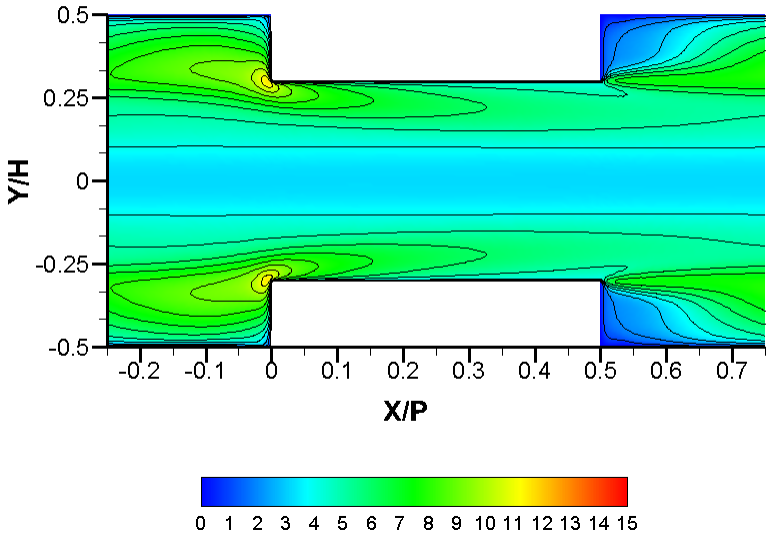

Figure 88: Turbulence intensity at the symmetry plane for Case A5 at 40,000 Re

At 30,000 and 40,000 channel Reynolds number, the turbulence intensity levels in the 5:1 rib aspect ratio configuration is less than the 3:1 rib aspect ratio configuration, which was also less than the 1:1 rib aspect ratio configuration. Increasing the rib width has the result of also reducing the turbulence intensity level and adversely impacts the strength of the shear layer growth; reattachment was not found to occur for Case A5. Interestingly, at 20,000 Reynolds number, the turbulence intensity levels of Case A5 are actually greater than seen in Case A3, however the turbulence intensity levels for Case A5 are still less than Case A1. Additional insight is needed for the 20,000 Reynolds number cases for Case A3 and Case A5 to determine if the turbulent kinetic energy for Case A5 is unusually high or if the turbulent kinetic energy for Case A3 is unusually low.

Case A1: 1:1 Rib Aspect Ratio Local Heat Transfer Results

Figure 89 contains the local heat transfer augmentation values on the ribbed wall for Case A1 at 20,000 Reynolds number from a normal viewing location. Only the top surface of the rib is visible in the figure, the leading and trailing surfaces of the rib are not shown. Figure 90 contains the local heat transfer augmentation values for the same Reynolds number, but on the non-ribbed side wall.

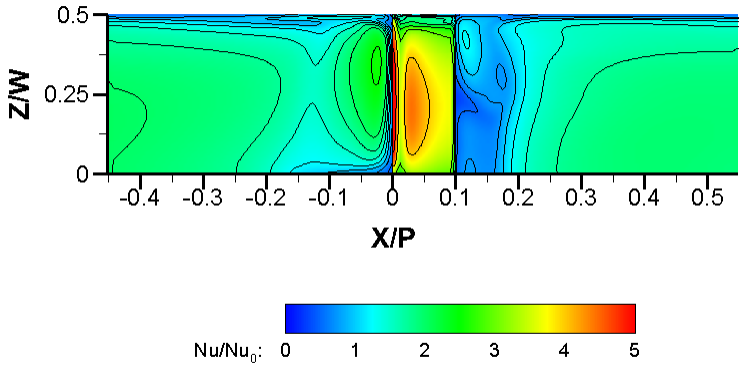

Figure 89: Local heat transfer augmentation on ribbed wall of Case A1 at 20,000 Re

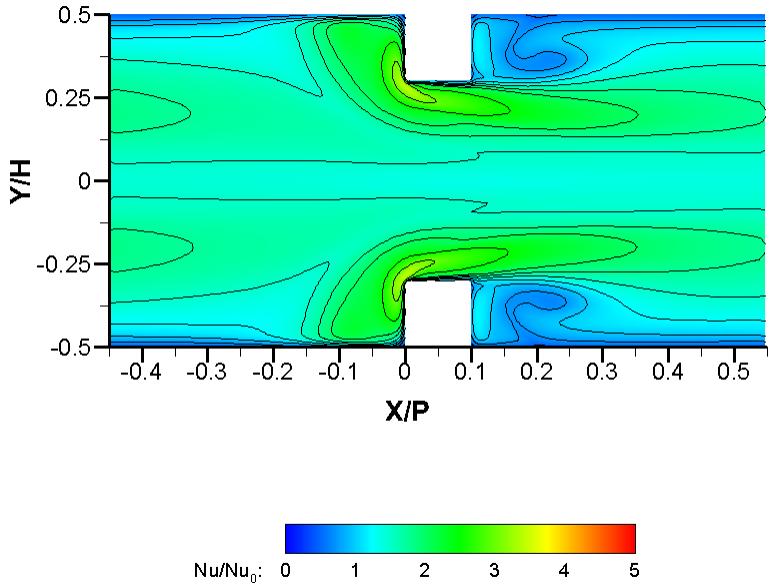

Figure 90: Local heat transfer augmentation on non-ribbed wall of Case A1 at 20,000 Re

Figure 91 contains the local heat transfer augmentation values on the ribbed wall for Case A1 at 30,000 Reynolds number from a normal viewing location and Figure 92 contains the local heat transfer augmentation values on the non-ribbed side wall.

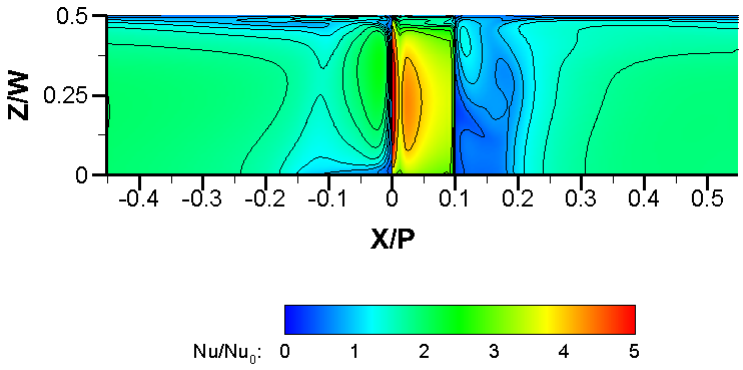

Figure 91: Local heat transfer augmentation on ribbed wall of Case A1 at 30,000 Re

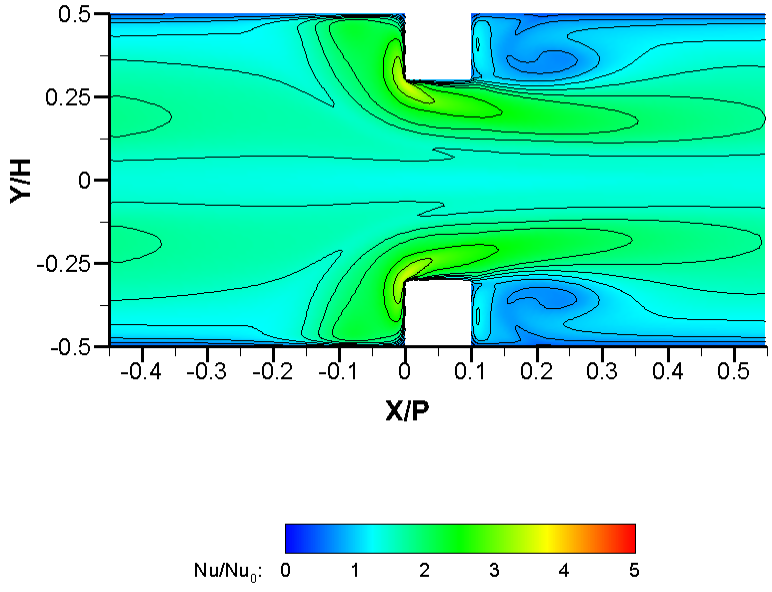

Figure 92: Local heat transfer augmentation on non-ribbed wall of Case A1 at 30,000 Re

Figure 93 contains the local heat transfer augmentation values on the ribbed wall for Case A1 at 40,000 Reynolds number from a normal viewing location and Figure 94 contains the local heat transfer augmentation values on the non-ribbed side wall.

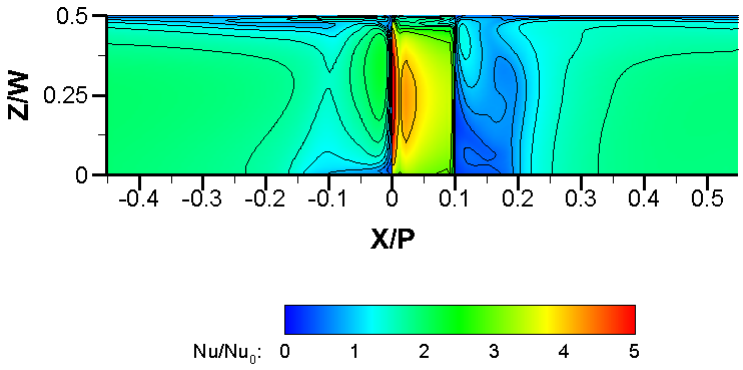

Figure 93: Local heat transfer augmentation on ribbed wall of Case A1 at 40,000 Re

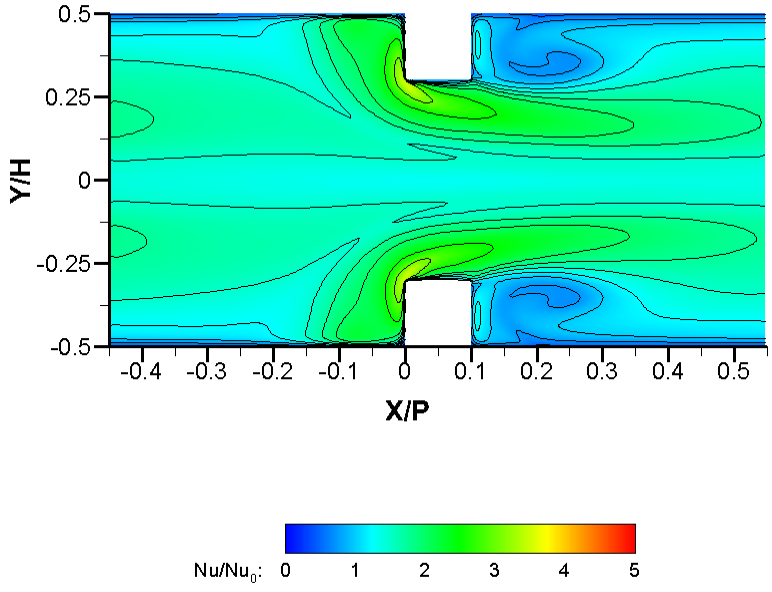

Figure 94: Local heat transfer augmentation on non-ribbed wall of Case A1 at 40,000 Re

The highest heat transfer enhancement occurs on the top surface of the rib and occupies the entire top surface of the rib, higher near the leading edge. A small region of low heat transfer occupies the region immediately behind the rib; the region of lowest heat transfer occupies approximately one rib height (1.0 e) of space behind the rib. The heat transfer enhancement then increases rapidly in-between two ribs but decreases slightly about one rib height upstream of the next rib. On top of the rib surface and upstream of the rib, there is also a bubble of heat transfer enhancement, nearer to the channel side walls and away from the channel mid-span. These features of the local heat transfer distribution suggest that there is a tendency for interactions to occur between the rib-induced flow and the side walls in order to push the location of higher heat transfer enhancement away from the channel mid-span, further away from the channel centerline. However, these findings are not conclusive because the realizable-k-ϵ model is an isotropic turbulence model; additional study needs to be performed through either more detailed experiments or to use an anisotropic turbulence model to confirm the additional flow interactions.

The side walls do not receive as much enhancement as the ribbed walls overall, but there are some regions that do receive a significant amount near the leading edge of the rib where the flow must accelerate rapidly resulting in a heat transfer enhancement in regions offset from the channel half-height (Y=0). The heat transfer enhancement from the rib induced flow weakens gradually downstream of the rib but persists throughout the entire rib pitch. The influence of the recirculation can also be perceived on the sidewall heat transfer. The region immediately behind the rib is occupied by a low heat transfer region similar to the ribbed wall. The heat transfer augmentation recovers after a few rib heights but does not increase significantly above a heat

transfer augmentation of unity; the heat transfer enhancement of the rib induced flow primarily affects the ribbed walls and does not influence the side walls as strongly.

On the side walls, the local distribution of Nusselt number enhancement does not change significantly with changes in Reynolds number. The values of the heat transfer enhancement are also consistent. The ribbed walls also exhibit similar trends at all three Reynolds numbers. Although the characteristic regions of high and low heat transfer did not change with Reynolds numbers, the level of heat transfer enhancement overall decreased with increasing Reynolds number.

Case A3: 3:1 Rib Aspect Ratio Local Heat Transfer Results

Figure 95 contains the local heat transfer augmentation values on the ribbed wall for Case A3 at 20,000 Reynolds number from a normal viewing location. Only the top surface of the rib is visible in the figure, the leading and trailing surfaces of the rib are not shown. Figure 96 contains the local heat transfer augmentation values for the same Reynolds number but on the non-ribbed side wall.

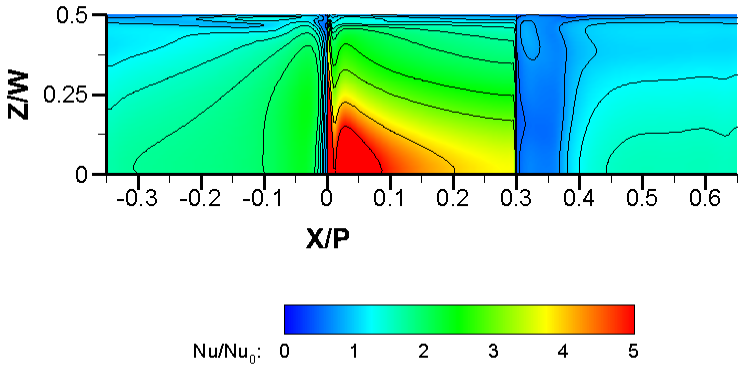

Figure 95: Local heat transfer augmentation on ribbed wall of Case A3 at 20,000 Re

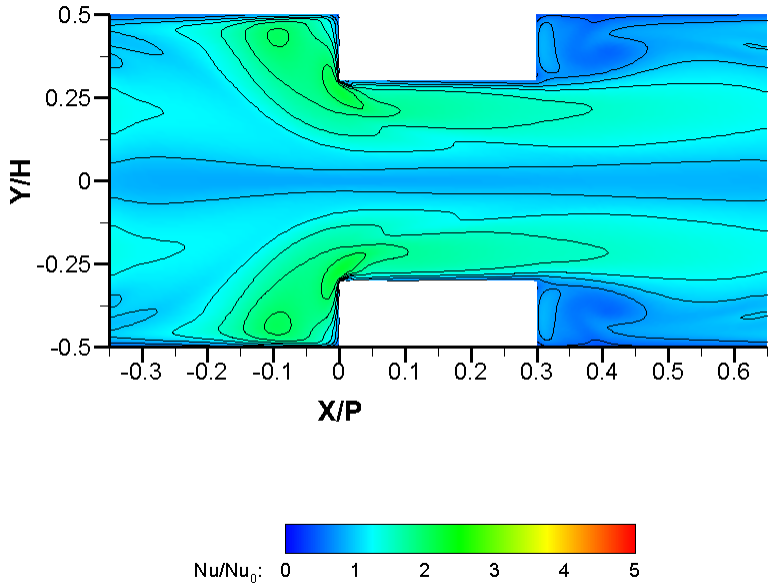

Figure 96: Local heat transfer augmentation on non-ribbed wall of Case A3 at 20,000 Re

Figure 97 contains the local heat transfer augmentation values on the ribbed wall for Case A1 at 30,000 Reynolds number from a normal viewing location and Figure 98 contains the local heat transfer augmentation values on the non-ribbed side wall.

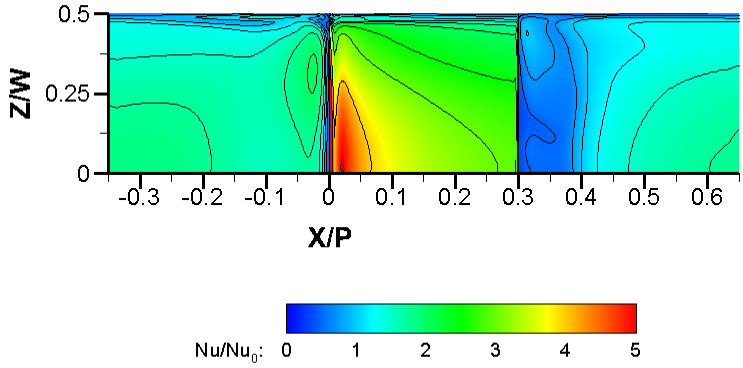

Figure 97: Local heat transfer augmentation on ribbed wall of Case A3 at 30,000 Re

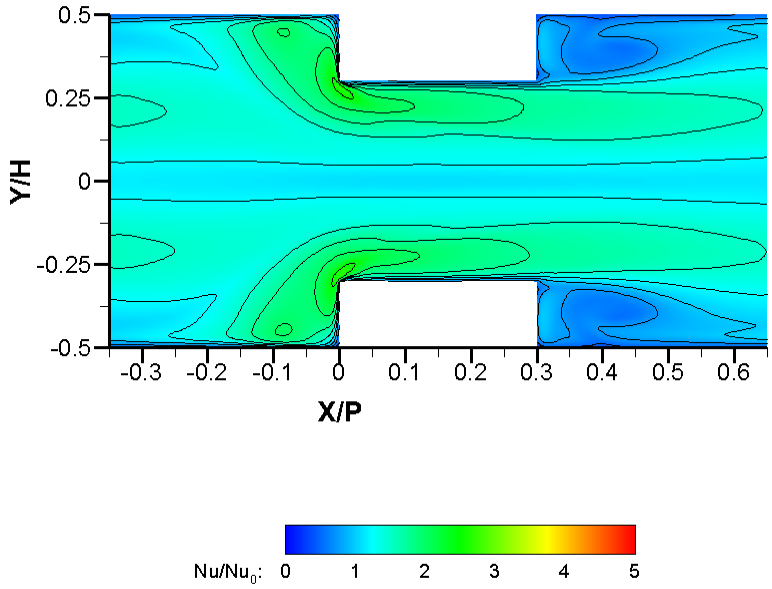

Figure 98: Local heat transfer augmentation on non-ribbed wall of Case A3 at 30,000 Re

Figure 99 contains the local heat transfer augmentation values on the ribbed wall for Case A3 at 40,000 Reynolds number from a normal viewing location and Figure 100 contains the local heat transfer augmentation values on the non-ribbed side wall.

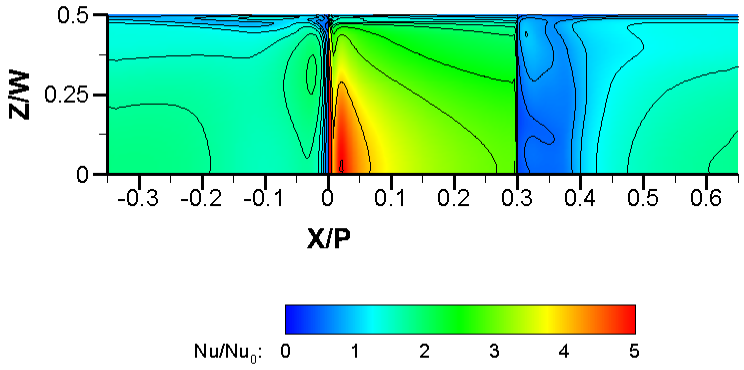

Figure 99: Local heat transfer augmentation on ribbed wall of Case A3 at 40,000 Re

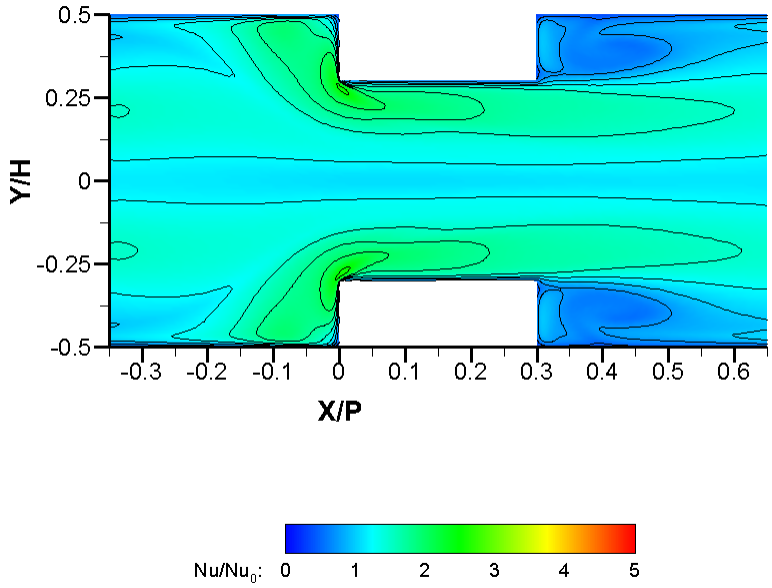

Figure 100: Local heat transfer augmentation on non-ribbed wall of Case A3 at 40,000 Re

Similar to the square ribs case, Case A1, the local trends in heat transfer enhancement did not vary significantly with changes in Reynolds number for both the ribbed walls and non-ribbed side walls for Case A3 but did decrease overall with increasing Reynolds number.

On the ribbed wall on Case A3, at the channel location upstream of the rib the bubble of higher heat transfer occurs at the channel mid-span and on the top of the rib surface, the highest heat transfer enhancement location for Case A3 also occurs at the mid-span (Z=0) and is contrary to Case A1, where both regions occurred at locations offset from the mid-span.

The side walls on Case A3 show similar trends in heat transfer enhancement compared to Case A1. Near the rib, there is a region of higher heat transfer, most pronounced upstream of the rib, corresponding to where the flow must accelerate between the ribs on the top and bottom wall. The heat transfer enhancement persists until the next rib, but is not as strong compared to Case A1.

The highest heat transfer enhancement occurs on the top surface of the rib, also near the leading edge. Comparatively, there is a smaller region of very high heat transfer enhancement on top of the rib for Case A3 compared to Case A1; from the region of highest heat transfer near the leading edge, the enhancement level decreases away from the mid-span more quickly than in Case A1. A small region of low heat transfer occupies the region immediately behind the rib; the region of lowest heat transfer occupies approximately one rib height (1.0 e) of space behind the rib, similar to Case A1. The heat transfer enhancement then increases in-between two ribs but decreases slightly about one rib height upstream of the next rib, which also occurred for Case A1.

Case A5: 5:1 Rib Aspect Ratio Local Heat Transfer Results

Figure 101 contains the local heat transfer augmentation values on the ribbed wall for Case A3 at 20,000 Reynolds number from a normal viewing location. Only the top surface of the rib is visible in the figure, the leading and trailing surfaces of the rib are not shown. Figure 102 contains the local heat transfer augmentation values for the same Reynolds number but on the non-ribbed side wall.

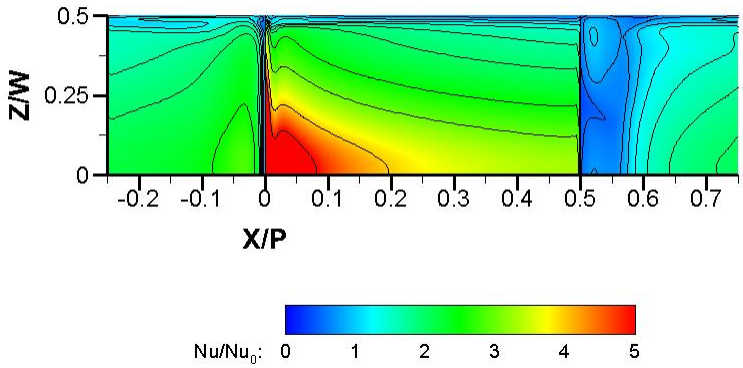

Figure 101: Local heat transfer augmentation on ribbed wall of Case A5 at 20,000 Re

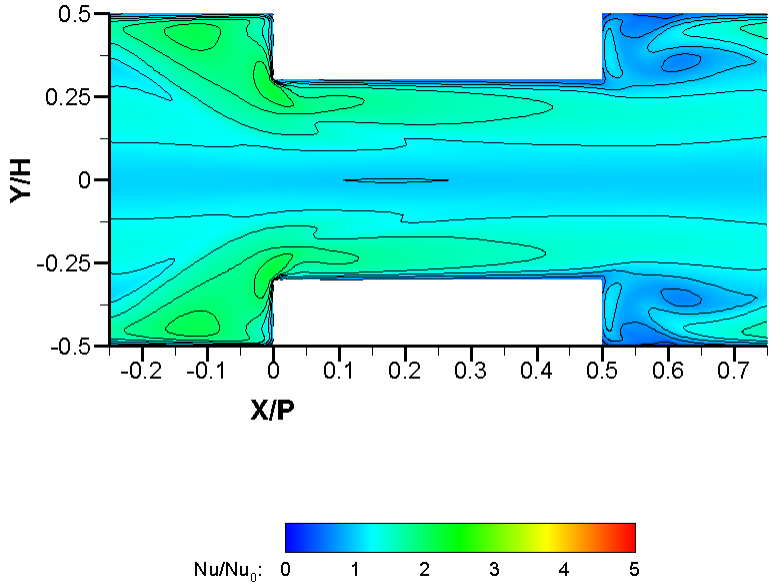

Figure 102: Local heat transfer augmentation on non-ribbed wall of Case A5 at 20,000 Re

Figure 103 contains the local heat transfer augmentation values on the ribbed wall for Case A5 at 30,000 Reynolds number from a normal viewing location and Figure 104 contains the local heat transfer augmentation values on the non-ribbed side wall.

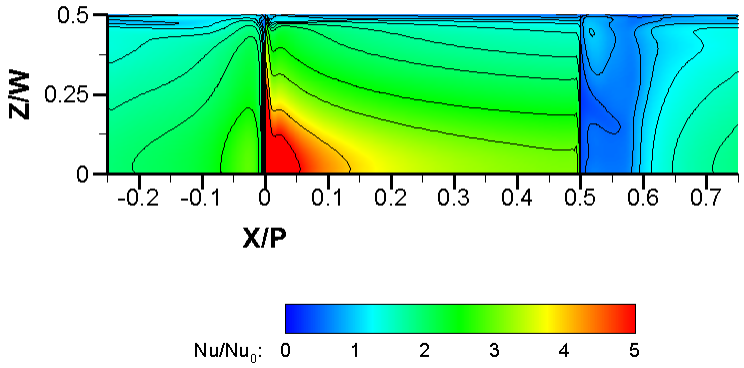

Figure 103: Local heat transfer augmentation on ribbed wall of Case A5 at 30,000 Re

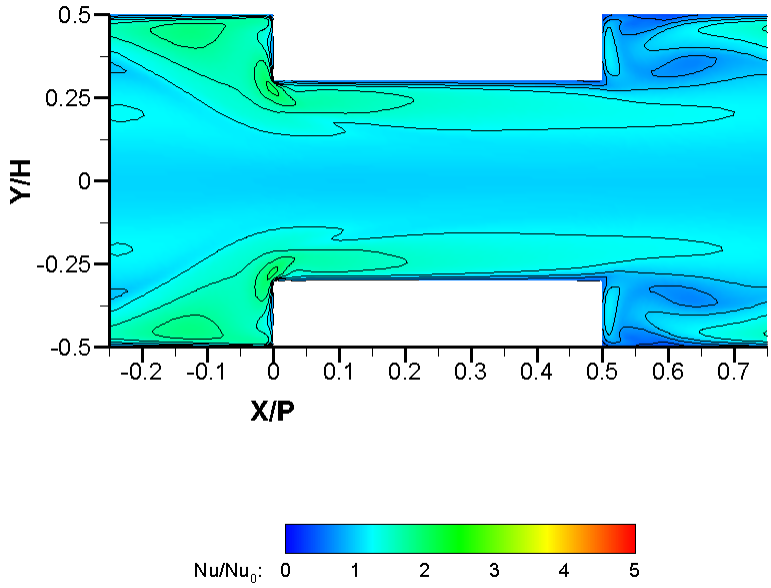

Figure 104: Local heat transfer augmentation on non-ribbed wall of Case A5 at 30,000 Re

Figure 105 contains the local heat transfer augmentation values on the ribbed wall for Case A5 at 40,000 Reynolds number from a normal viewing location and Figure 106 contains the local heat transfer augmentation values on the non-ribbed side wall.

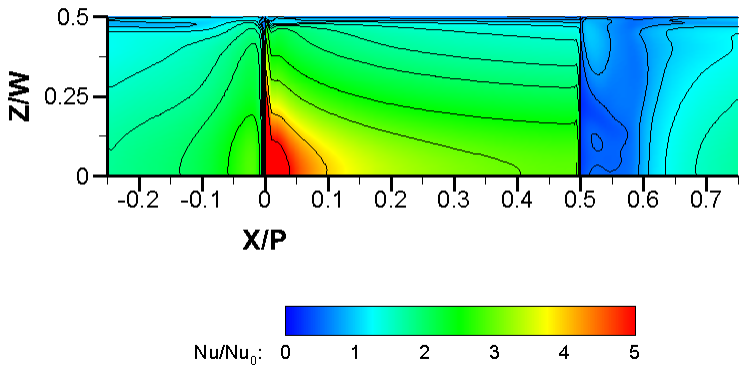

Figure 105: Local heat transfer augmentation on ribbed wall of Case A5 at 40,000 Re

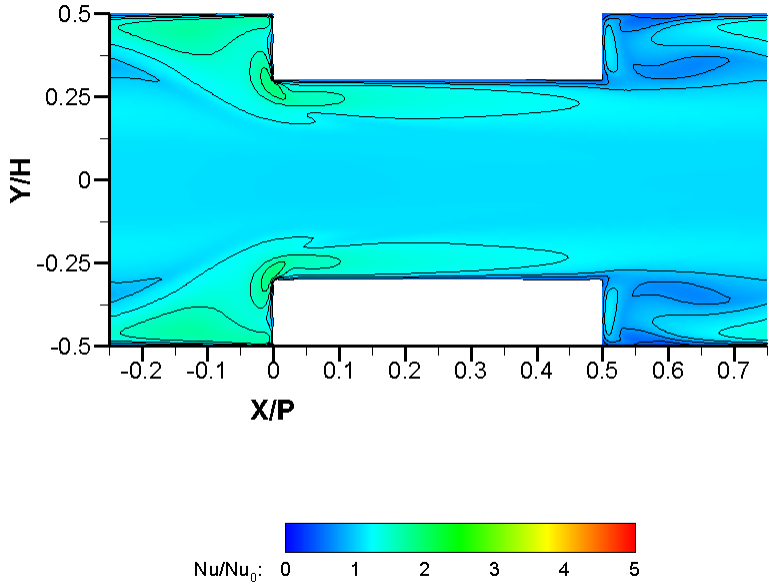

Figure 106: Local heat transfer augmentation on non-ribbed wall of Case A5 at 40,000 Re

Similar to the Case A1 and A3, the local trends in heat transfer enhancement did not vary significantly with changes in Reynolds number for both the ribbed walls and non-ribbed side walls on Case A5.

Similar to the square ribs case, Case A1, the local trends in heat transfer enhancement did not vary significantly with changes in Reynolds number for both the ribbed walls and non-ribbed side walls for Case A3 but did decrease overall with increasing Reynolds number.

On the ribbed wall on Case A5, the distribution of the heat transfer enhancement is more akin to that of Case A3; at the channel location upstream of the rib the bubble of higher heat transfer occurs at the channel mid-span and on the top of the rib surface, the highest heat transfer enhancement location for Case A5 also occurs at the mid-span (Z=0). The offset location of the

highest heat transfer enhancement, away from the channel mid-span, occurred only for the square ribs case and was not repeated on the two wider rib cases.

The heat transfer enhancement on top of the rib for Case A5 is also comparatively less than Cases A1 and A3. The region of highest heat transfer on the top of the rib is smaller compared to Case A3 and even smaller than Case A1. Near the corners of the channel, the ribbed surface of Case A5 also has a comparatively larger region of lower heat transfer than A3 and A1. The lower heat transfer enhancement on the rib of Case A5, coupled with the larger physical size of the rib results in the rib of Case A5 having the lowest heat transfer enhancement.

The side walls on Case A5 have a resemblance to the same trends of heat transfer enhancement that occurred for Cases A1 and A3, but the features are not as distinct. The small region of heat transfer enhancement near the rib and the region of low heat transfer behind the rib are both still observable; however the side walls for Case A5 largely do not exhibit any significant levels of heat transfer enhancement.

The highest heat transfer enhancement occurs on the top surface of the rib, near the leading edge. A small region of low heat transfer occupies the region immediately behind the rib; the region of lowest heat transfer occupies approximately one rib height (1.0 e) of space behind the rib, similar to both Cases A1 and A3. The heat transfer enhancement then increases in-between two ribs and reaches a maximum immediately upstream of the next rib. For Case A5, a region of reduced heat transfer enhancement was not observed between two ribs, which were found previously on both Case A1 and Case A3.

Comparison of Numerical Friction Results

The overall channel friction factor of all the rib configurations studied is plotted in Figure 107. The corresponding channel friction factor augmentations are plotted in Figure 108.

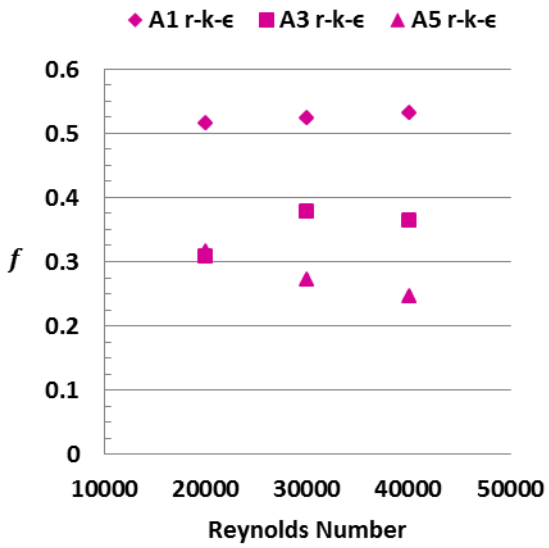

Figure 107: Numerical friction factor

For the square ribs case, the channel friction factor is found to increase slightly with Reynolds number. For Case A3, at 30,000 Reynolds number, the numerically obtained friction factor was actually greater than at 20,000 and at 40,000 Reynolds number. In other words, the friction factor at 20,000 Reynolds number was much less than at 30,000 and 40,000 Reynolds numbers. At 30,000 and 40,000 Reynolds number, the friction factors can be considered approximately equal. For Case A5, the friction factor obtained from the realizable-k-ϵ model decreased with increased with increasing Reynolds number. At 20,000 Reynolds number, the friction factor of Case A5 was even greater than Case A3 by approximately 2%. With the

exception of the 20,000 Reynolds number cases for Cases A3 and A5, the channel friction factor for the square ribs, Case A1, was consistently greater than Case A3, which was also greater than Case A5.

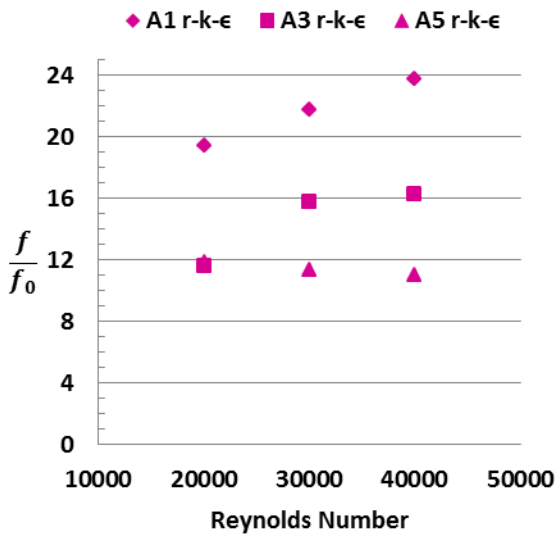

Figure 108: Numerical friction factor augmentation

The trends in the friction factor augmentation are similar to the friction factors, the friction factor augmentation being derived from the friction factor, but normalized by the Blasius correlation. The trends for the friction augmentation for Case A1 and A3 are increasing friction factor augmentation with an increase in Reynolds number. For Case A5, the friction augmentation decreases slightly with Reynolds number. Similar to the friction factor, the friction augmentation of Case A1 is consistently greater than Case A3. The friction augmentation of Case A3 is also greater than Case A5, except at 20,000 Reynolds number.

Comparison of Numerical Rib and Wall Averaged Heat Transfer Results

The average heat transfer augmentation of only the ribbed portions of the channel is plotted in Figure 109. Unfilled symbols in the figure represent the rib-only averaged Nusselt number ratio.

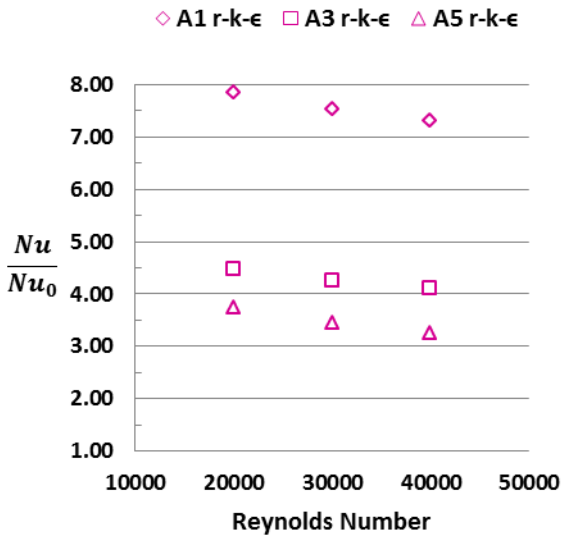

Figure 109: Heat transfer augmentation on rib from numerical study

With increasing rib aspect ratio, the heat transfer enhancement on the ribbed surfaces decreased for each of the Reynolds numbers tested. For each of the rib configurations, the heat transfer enhancement on the ribs decreased with increasing Reynolds number. The square ribs have the greatest heat transfer enhancement of all the rib cases studied, followed by the 3:1 aspect ratio ribs, with the 5:1 aspect ratio ribs having the lowest heat transfer enhancement of the cases studied. The heat transfer enhancement of the 1:1 aspect ratio ribs was nearly double the heat transfer enhancement on the other ribs studied.

The wall averaged heat transfer augmentation of the entire top and bottom wall is contained in Figure 110. Filled symbols are used to represent the wall averaged Nusselt number ratios. The wall averaged heat transfer augmentation includes both the heat transfer augmentation of the ribbed and non-ribbed portions of the channel.

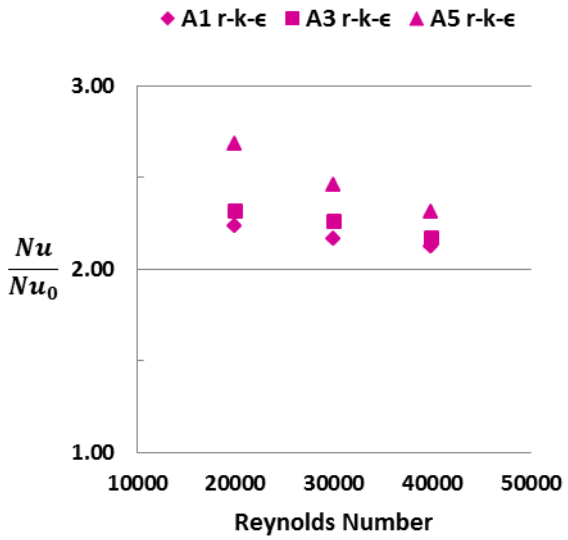

Figure 110: Average heat transfer augmentation on ribbed walls from numerical study

In contrast to the heat transfer enhancement on the ribs, the trends in overall heat transfer enhancement are the opposite. The 1:1 rib aspect ratio case produced the lowest heat transfer enhancement overall, followed by the 3:1 aspect ratio ribs, with the 5:1 aspect ratio rib channel having the highest overall heat transfer enhancement. Despite the square ribs having the highest heat transfer, the effect on the overall heat transfer in the channel is less pronounced. The square ribs have the smallest projected area (or wall coverage) and hence their contribution to the overall heat transfer in less compared to the larger ribs.

COMPARISON OF EXPERIMENTAL AND NUMERICAL RESULTS

With the combination of both experimental and numerical techniques applied to this study, a direct comparison of the results obtained from each method is a logical step. The results presented in this section reiterate the ones already presented, but in one location in order to facilitate enhanced visualization of the key differences in the results and to make a direct comparison of the results obtained through each method, experimental and numerical.

Comparison of Friction Results

The overall channel friction factor of all the cases studied is plotted in Figure 111. The plotted data follows the same conventions used earlier. The diamond shapes correspond to Case A1, the square shapes correspond to Case A3, and the triangle shapes correspond to Case A5. Separate colors are used to fill the shapes to denote the ones obtained experimentally from the ones obtained numerically. Likewise, the overall friction factor augmentation of each of the cases studied, both experimentally and numerically, is plotted in Figure 112.

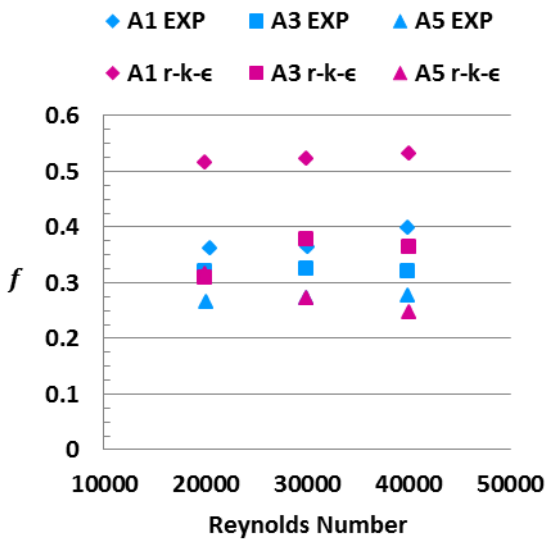

Figure 111: Comparison of experimental and numerical friction factor

There are a number of notable differences between the channel friction factors obtained numerically using the realizable-k-ϵ model and that obtained experimentally. For the square ribs case, the realizable-k-ϵ model vastly over-predicts the channel friction compared to the experimentally obtained values by 30-45% depending on Reynolds number, well beyond the experimental uncertainty in the experiment. The realizable-k-ϵ model does however predict a relatively constant friction factor as was obtained experimentally.

For Case A3, at 30,000 Reynolds number, the numerically obtained friction factor was actually greater than at 20,000 and 40,000 Reynolds numbers, a trend not observed experimentally although the experiments also contain a finite amount of uncertainty in the measurements. At 20,000 Reynolds number, the realizable-k-ϵ model is in agreement with the

experiment. The realizable-k-ϵ model over-predicts the channel friction by 16% at 30,000 Reynolds number, and 14% at 40,000 Reynolds number.

For Case A5, the friction factor obtained from the realizable-k-ϵ model decreased with increased with increasing Reynolds number, whereas the friction factor was nearly constant when measured experimentally. At 20,000 Reynolds number, the realizable-k-ϵ model over-predicted the friction factor by approximately 19%. The friction factors were in agreement at 30,000 Reynolds number. And at 40,000 Reynolds number, the realizable-k-ϵ model under-predicted the friction factor by approximately 12%.

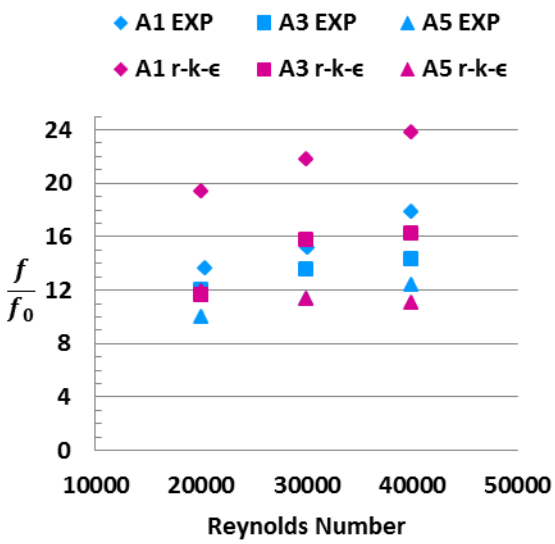

Figure 112: Comparison of experimental and numerical friction augmentation

The same discrepancies in the friction factor between the experimental and numerical study also affect the trends in the overall friction factor augmentation.

For the square ribs case, the realizable-k-ϵ model vastly over-predicts the channel friction augmentation compared to the experimentally obtained values, well beyond the experimental uncertainty in the experiment. The realizable-k-ϵ model does however does predict trends similar to the experimental measurements, an increasing friction factor augmentation with increasing Reynolds number.

For Case A3, the differences between the predictions offered by the realizable-k-ϵ model are within acceptable levels of agreement with the experimental results.

For Case A5, the friction factor obtained from the realizable-k-ϵ model decreased with increased with increasing Reynolds number, whereas the friction factor was nearly constant when measured experimentally.

Comparison of Heat Transfer Results

The average heat transfer augmentation of only the ribbed portions of the channel is plotted in Figure 109. Following the convention used in the previous sections when presenting the individual experimental and numerical results, unfilled symbols in the figure represent the rib-only averaged Nusselt number ratio. Different coloring is used to distinguish the experimental results from the numerical results obtained from the realizable-k-ϵ model.

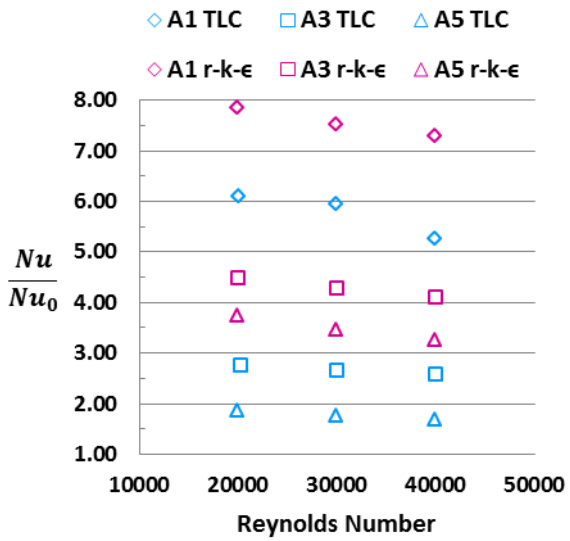

Figure 113: Comparison of rib-averaged heat transfer augmentation

For the ribbed portions of the channel, the realizable-k-ϵ model consistently predicts higher heat transfer on the ribs than what was obtained experimentally. However, the experimental and numerical techniques both predict the same trend of decreasing heat transfer augmentation with increasing Reynolds number.

The current method of calculating the heat transfer coefficient from the lumped capacitance is known to be a conservative estimate of the heat transfer because the conduction of heat through the interface between the copper rib features and the acrylic substrate underneath is currently neglected. Correctly accounting for the conduction through the interface is one of the shortcomings of the current experimental results. However, even if the additional conduction is accounted for, the corrected results would likely maintain a similar offsets between the numerical and experimental results. The offset between the experimental and numerical results are well

beyond both the experimental uncertainty of the experiments, and beyond what could possibly be corrected for by accounting for the additional heat conduction; the offset between the two methods for the square ribs case ranges from 1.58 to 2.05. A method of accounting for the additional conduction is under development.

The averaged heat transfer augmentation in the region in between ribs is shown in Figure 115. The hatched symbols are used to represent the average heat transfer enhancement of the smooth wall portions wall in between two ribs.

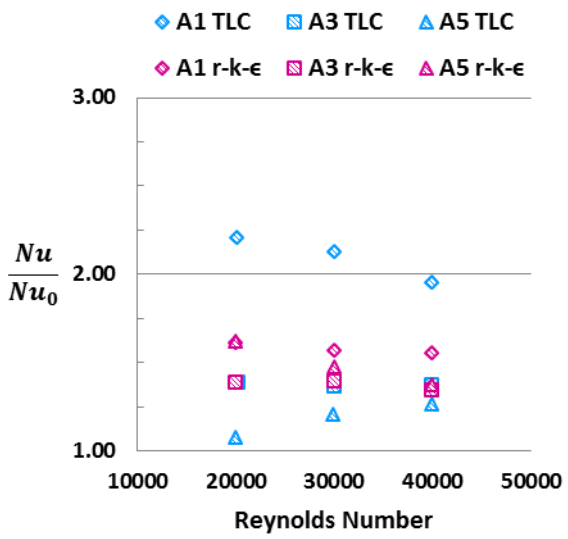

Figure 114: Comparison of heat transfer augmentation in non-ribbed portion

In between ribs, the realizable-k-ϵ model under-predicts the heat transfer enhancement on the square ribs case for all three channel Reynolds numbers. For Case A3, the numerical and experimental results are in agreement at all three channel Reynolds numbers. For Case A5, the

realizable-k-ϵ model over-predicts the heat transfer enhancement occurring in between ribs at all three Reynolds numbers, although the disagreement is less at 40,000 Reynolds number.

The wall averaged heat transfer augmentation of the entire top and bottom wall is shown in Figure 115. Following the convention used in the previous sections when presenting the individual experimental and numerical results, filled symbols are used to represent the wall averaged Nusselt number ratios. The wall averaged heat transfer augmentation includes both the heat transfer augmentation of the ribbed and non-ribbed portions of the channel.

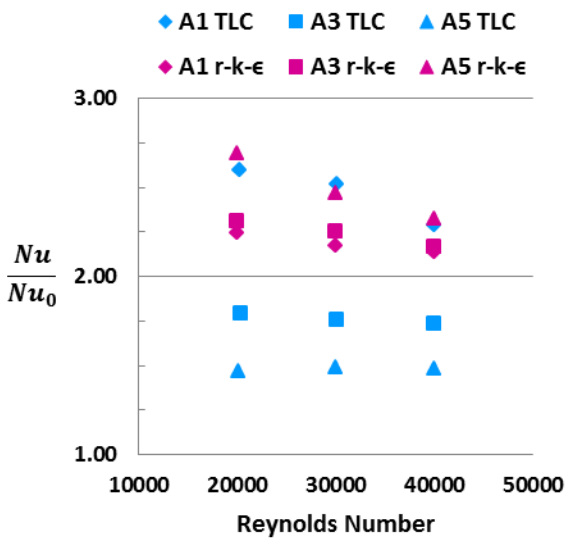

Figure 115: Comparison of ribbed wall averaged heat transfer augmentation

The compounded discrepancies between the results obtained experimentally and using the realizable-k-ϵ model are evident. Significant offset between the results from the two methods exist for all three rib configurations. The realizable-k-ϵ model is over-predicting the heat transfer enhancement on the two larger rib cases, Case A3 and Case A5, but is under-predicting the heat

transfer enhancement for the square ribs case. As discussed earlier, the heat transfer on the ribbed surface is currently under-predicted for the experiment (a conservative estimate for the heat transfer enhancement). A more accurate calculation of the surface heat transfer coefficient on the copper ribs would increase the heat transfer enhancement seen on the ribs for all of the experimental cases and subsequently would increase the wall-averaged heat transfer augmentation. This increase would bring the experimental results closer to the numerical results for Cases A3 and A5, but would increase the discrepancy for Case A1.

CONCLUSION

The local heat transfer on two opposite rib roughened walls was studied at 20,000, 30,000, and 40,000 Reynolds numbers in a 2:1 aspect ratio rectangular channel. The overall channel pressure drop, friction factor, and friction augmentation were also studied. Three rib aspect ratio cases were studied by systematically altering the rib width while holding all other parameters constant. The ribs were applied orthogonal to the main flow direction, with ribs aligned between opposite walls. The ribbed channels were studied both experimentally and numerically. The transient TLC technique was utilized to deduce local heat transfer coefficients and wall static pressure taps were utilized to measure the overall channel pressure drop. The computational fluid dynamics study was performed using a steady RANS simulation using the realizable k-ϵ model.

From the experiments, a number of conclusions on the performance of the different rib configurations can be made:

- Overall heat transfer augmentation decreased with increasing Reynolds numbers for all ribbed channels studied.
- At a constant rib pitch, wider ribs induce weaker reattachment zones in the space between ribs, with no reattachment being observed for the case of the rib aspect ratio of 5.
- Increasing the rib width decreased the overall heat transfer augmentation but also decreased the friction factor augmentation.

The discrepancy between the experimental results and the numerical results obtained from the realizable-k-ϵ model should be addressed, since there was not a clear pattern to the differences. Since the experimental measurements are unlikely to be completely flawed, it can

only be concluded that the realizable-k-ϵ model is not accurately reproducing the same heat transfer and friction results as the experiments.

The realizable-k-ϵ model predicted the correct trends in heat transfer enhancement on the ribbed surfaces, but there was an offset between the results from the realizable-k-ϵ model and the experimentally obtained results.

The heat transfer enhancement in between ribs was in agreement for Case A3 for the realizable-k-ϵ model and the experimental results obtained with the transient TLC technique. However, the performance of the 1:1 RAR configuration was under-predicted by the realizable-k-ϵ model, but over-predicted for the 5:1 RAR configuration.

An improved method for correctly calculating the heat transfer coefficient using the lumped capacitance model needs to be performed, which is currently under development and will be employed in future testing. Performing this correction on the current results may recover some of the discrepancies between the experimental results and numerical results.

Further study of the same rib configurations can also be done with other turbulence models. The k-ω model has yet to be tested and may produce more accurate results than the current realizable-k-ϵ model. However, the Reynolds Stress Modeling approach would likely produce the most accurate results, since the RSM modeling approach allows for anisotropic turbulence. The secondary flows and corner vortices, which are a result of the turbulence anisotropy, are currently not being predicted at all by the realizable-k-ϵ model, which is an isotropic model. The k-ω model, similar to the k-ϵ model is also an isotropic model, hence the use of the RSM model is more recommended. The most accurate study can be performed with

Large Eddy Simulations. A Large Eddy Simulation can be performed on the current computational grid with the appropriate implicit time-stepping scheme. The computation grids used in the current study were generated with the intent of performing an LES study to directly compare the results obtained from the use of different turbulence models. It is recommended however, to further optimize the current mesh.

REFERENCES

Bejan, A. (1978). General criterion for rating heat-exchanger performance. *International Journal of Heat and Mass Transfer, 21*, 655-658.

Bejan, A. (1993). *Heat Transfer.* John Wiley & Sons, Inc.

Bejan, A. (2006). *Advanced Engineering Thermodynamics* (3 ed.). John Wiley & Sons.

Bunker, R. S., Wetzel, T. G., & Rigby, D. l. (2002). Heat Transfer in a Complex Trailing Edge Passage for a High Pressure Turbine Blade – Part 1: Experimental Measurements. *ASME Turbo Expo 2002*, (pp. 1-7). Amsterdam.

Carlson, J., Jaffe, A., & Wiles, A. (2000). *The Millenium Prize Problems.* Cambridge, Massachusetts, United States of America: Clay Mathematics Institute.

Casarsa, L., Cakan, M., & Arts, T. (2002). Characterization of the Velocity and Heat Transfer Fields in an Internal Cooling Channel with High Blockage Ratio. *Turbo Expo 2002*, (pp. 1-8). Amsterdam.

Chandra, P. R., Niland, M. E., & Han, J. C. (1997, April). Turbulent Flow Heat Transfer and Friction in a Rectangular Channel with Varying Numbers of Ribbed Walls. *Journal of Turbomachinery, 119*, 374-380.

Chen, S. P., Li, P. W., & Chyu, M. K. (2006). Heat Transfer in an Airfoil Trailing Edge Configuration with Shaped Pedestals Mounted Internal Cooling Channel and Pressure Side Cutback. *ASME Turbo Expo 2006.* Barcelona.

Cho, H. H., Lee, S. Y., & Wu, S. J. (2001). The Combined Effect of Rib Arrangements and Discrete Ribs on Local Heat/Mass Transfer in a Square Duct. *ASME 46th Annual International Gas Turbineand Aeorengine Congress and Exhibition*, (pp. 1-11). New Orleans, LA.

Chyu, M. D. (1998). Determination of Local Heat Transfer Coefficient Based on Bulk Mean Temperature Using a Transient Liquid Crystals Technique. *Experimental Thermal and Fluid Science*, 142-149.

Chyu, M. K. (2010). Recent Advances in Turbine Heat Transfer-With a View of Transition to Coal Gas Based Systems. *14th International Heat Transfer Conference.* Washington D.C.

Eriksson, S. (2007). The Swedish Development of Turbogenerators with directly water-cooled Rotors. *2007 IEEE Conference on the History of Electric Power* (pp. 109-116). Newark: IEEE.

Gladden, H. J., & Simoneau, R. J. (1989). Review and Assessment of the Database and Numerical Modeling for Turbine Heat Transfer. In I. D. E. Sokolowski (Ed.), *Toward Improved Durability in Advanced Aircraft Engine Hot Sections* (Vol. 2, pp. 39-55).

Hallcrest. (1991). *Handbook of Thermochromic Liquid Crystal Technology*. Handbook, Hallcrest, Liquid Crystal Research, Glenview.

Han, J. C., Park, J. S., & Lei, C. (1985). Heat Transfer Enhancement in Channels With Turbulence Promoters. *Journal of Engineering for Gas Turbines and Power, 107*(3), 628-635.

Han, J.-C. (1984, November). Heat Transfer and Friction in Channels With Two Opposite Rib-Roughened Walls. *Journal of Heat Transfer, 106*, 774-781.

Han, J.-C., Glicksman, L., & Rohsenow, W. (1978). An Investigation of Heat Transfer and Friction for Rib-Roughened Surfaces. *Int. J. Heat Mass Transfer, 21*, 1143-1156.

Han, J.-C., Huang, J. J., & Lee, C. P. (1993). Augmented Heat Transfer in Square Channels with Wedge-Shaped and Delta-Shaped Turbulence Promoters. *Enhanced Heat Transfer, 1*(1), 37-52.

Huh, M., Liu, Y.-H., Han, J.-C., & Chopra, S. (2008). Effect of Rib Spacing on Heat Transfer in a Two-Pass Rectangular Channel (AR=1:4) With a Sharp Entrance at High Rotation Numbers. *ASME Turbo Expo 2008.* Berlin.

Incropera, F. P., Dewitt, D. P., Bergman, T. L., & Lavine, A. S. (2006). *Fundamentals of Heat and Mass Transfer* (6 ed.). John Wiley and Sons.

Kakac, S., Shah, R. K., & Aung, W. (1987). *Handbook of Single-Phase Convective Heat Transfer.* New york, United States of America: John Wiley & Sons.

Kasagi, N., Hasegawa, Y., Fukagata, K., & Iwamoto, K. (2010). Control of Turbulent Transport: Less Friction and More Heat Transfer. *14th International Heat Transfer Conference.* Washington, D.C.: ASME.

Kline, S. J., & McClintock, F. A. (1953, January). Describing uncertainties in single sample experiments. *Mechanical Engineering, 75*, 3-8.

Kunstmann, S., von Wolfersdorf, J., & Ruedel, U. (2009). Heat Transfer and Pressure Loss in Rectangular One-Side-Ribbed Channels With Different Aspect Ratios. *ASME Turbo Expo 2009.* Orlando.

Lakshminarayana, B. (1996). *Fluid Dynamics and Heat Transfer of Turbomachinery.* New York: John Wiley and Sons.

Liu, Y.-H., Wright, L. M., Fu, W.-L., & Han, J.-C. (2006). Rib Spacing Effect on Heat Transfer and Pressure Loss in a Rotating Two-Pass Rectangular Channel (AR=1:2) with 45-Degree Angled Ribs. *ASME Turbo Expo.* Barcelona.

Liu, Y.-H., Wright, L. M., Fu, W.-L., & Han, J.-C. (2007). Rib Spacing Effect on Heat Transfer in Rotating Two-Pass Ribbed Channel (AR = 1:2). *Journal of Thermophysics and Heat Transfer, 21*(3), 582-595.

Mahmood, G. I., Ligrani, P. M., & Won, S. Y. (2002). Spatially-Resolved Heat Transfer and Flow Structure in a Rectangular Channel with 45° Angled Rib Turbulators. *ASME Turbo Expo 2002.* Amsterdam.

Maurer, M., Ruedel, U., Gritsch, M., & von Wolfersdorf, J. (2008). Experimental Study of Advanced Convective Cooling Technique for Combustor Liners. *ASME Turbo Expo 2008.* Berlin.

Moffat, R. J. (1985). Uncertainty analysis in the planning of an experiment. *Journal of Fluids Engineering, 107,* 173-181.

Otugen, M. V. (1991). Expansion Ratio Effects on the Separated Shear Layer and Reattachment Downstream of a Backward-Facing Step. *Experiments in Fluids, 10*, 273-280.

Pinelli, A., Uhlmann, M., Sekimoto, A., & Kawahara, G. (2010). Reynolds number dependence of mean flow structure in square duct turbulence. *Journal of Fluid Mechanics, 644*, 107-122.

Promvonge, P., & Thianpong, C. (2008). Thermal Performance Assessment of Turbulent Channel Flows Over Different Shaped Ribs. *International Communications in Heat and Mass Transfer, 35*, 1327-1334.

Rallabandi, A. P., Alkhamis, N., & Han, J.-C. (2009). Heat Transfer and Pressure Drop Measuremets for a Square Channel with 45deg Round Edged Ribs at High Reynolds Numbers. *ASME Turbo Expo 2009*. Orlando.

Salim, S. M., & Cheah, S. C. (2009). Wall y+ Strategy for Dealing with Wall-bounded Turbulent Flows. *International MultiConference of Engineers and Computer Scientists, 2*. Hong Kong.

Shih, T.-H., Liou, W. W., Shabbir, A., Yang, Z., & Zhu, J. (1995). A New k - ϵ Eddy-Viscosity Model for High Reynolds Number Turbulent Flows – Model Development and Validation. *Computers Fluids, 24*(3), 227-238.

Sparrow, E. M., & Cur, N. (1982). Turbulent Heat Transfer in a Symmetrically or Assymetrically Heated Flat Rectangular Duct with flow Separation at Inlet. *Journal of Heat Transfer, 104*, 82-89.

Taslim, M. E., Li, T., & Spring, S. D. (1998). Measurements of Heat Transfer Coefficients and Friction Factors in Passages Rib-Roughened on All Walls. *Journal of Turbomachinery, 120*(3), 564-570.

Tennekes, H., & Lumley, J. L. (1972). *A First Course in Turbulence.* United States of America: The Massachusetts Institute of Technology.

Wang, Z., Ireland, P. T., Kohler, S. T., & Chew, J. W. (1998). Heat Transfer Measurements to a Gas Turbine Cooling Passage with Inclined Ribs. *Journal of Turbomachinery, 120*(1), 63-69.

Wright, L. M., & Gohardani, A. S. (2008). Effect of Turbulator Width and Spacing on the Thermal Performance of Angled Ribs in a Rectangular Channel (AR=3:1). *ASME International Mechanical Engineering Congress and Exposition.* Boston: ASME.

Zhang, Y. M., Gu, W. Z., & Han, J.-C. (1994). Heat Transfer and Friction in Rectangular Channels with Ribbed or Ribbed-grooved walls. *Journal of Heat Transfer, 116*(1), 58-65.

APPENDIX A: EXPERIMENTALLY MEASURED STATIC PRESSURE DISTRIBUTIONS IN RIBBED CHANNELS

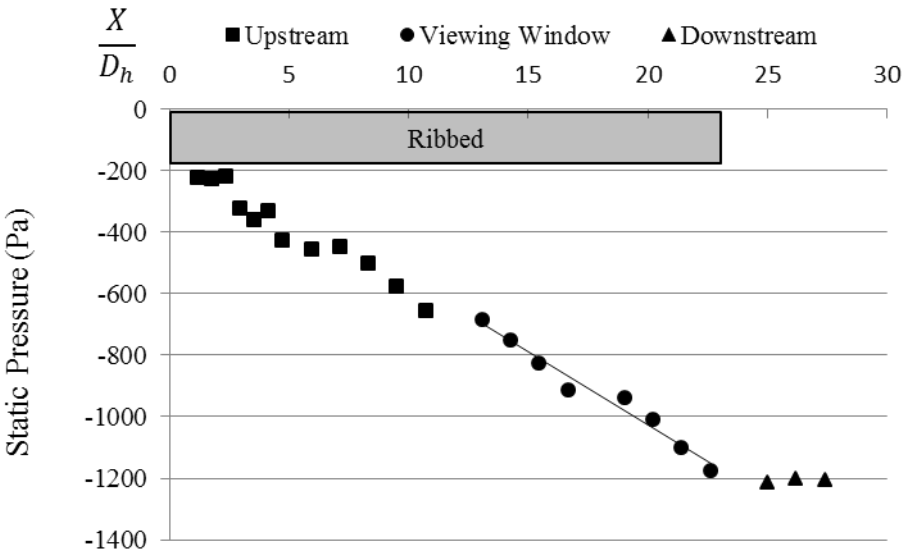

Figure 116: Static pressure distribution of Case A1 at 20,000 Re

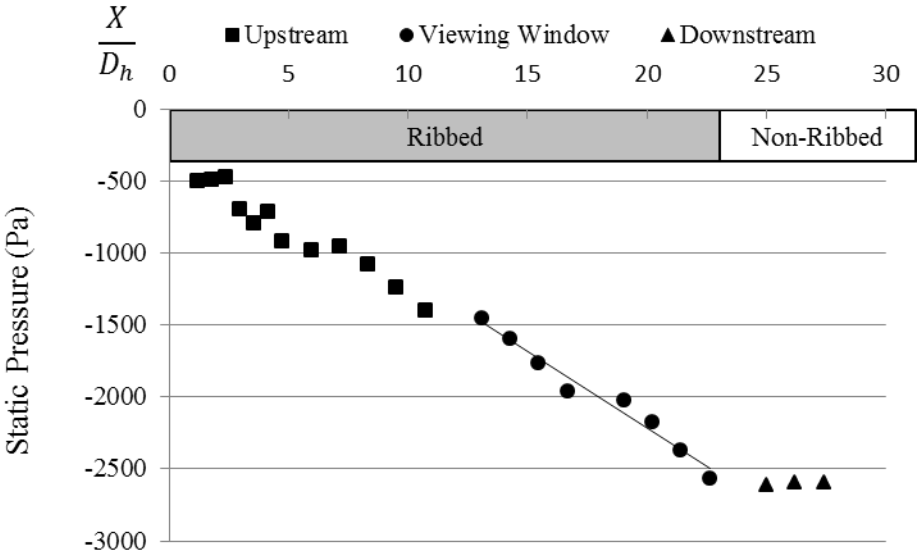

Figure 117: Static pressure distribution of Case A1 at 30,000 Re

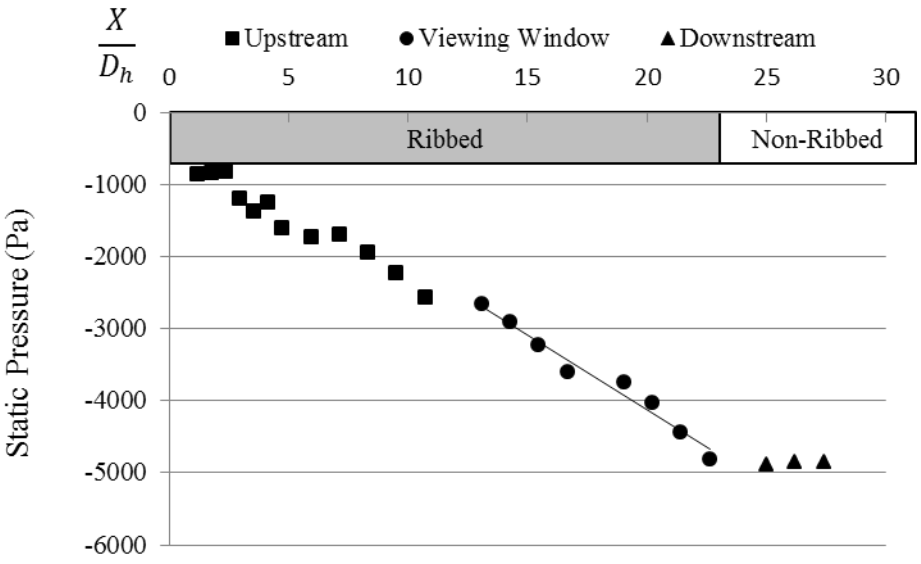

Figure 118: Static pressure distribution of Case A1 at 40,000 Re

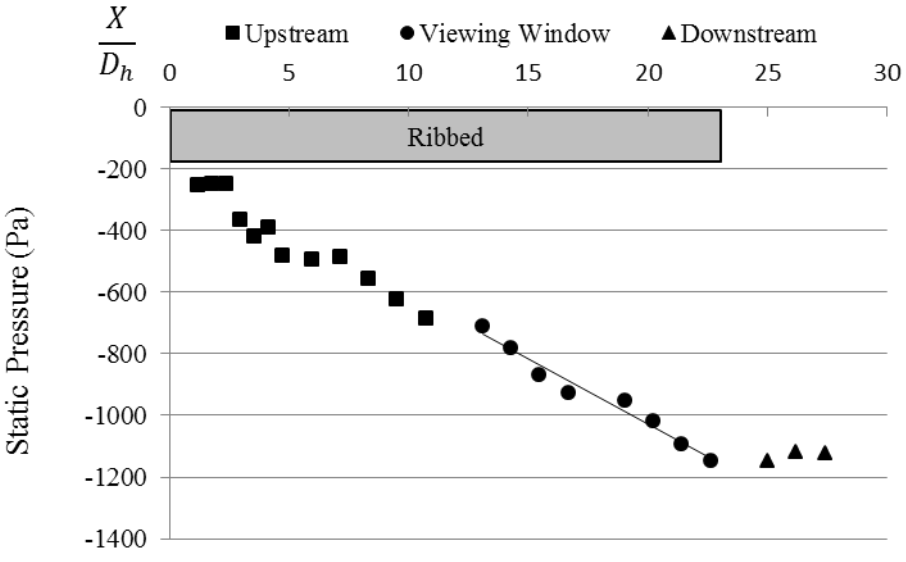

Figure 119: Static pressure distribution of Case A3 at 20,000 Re

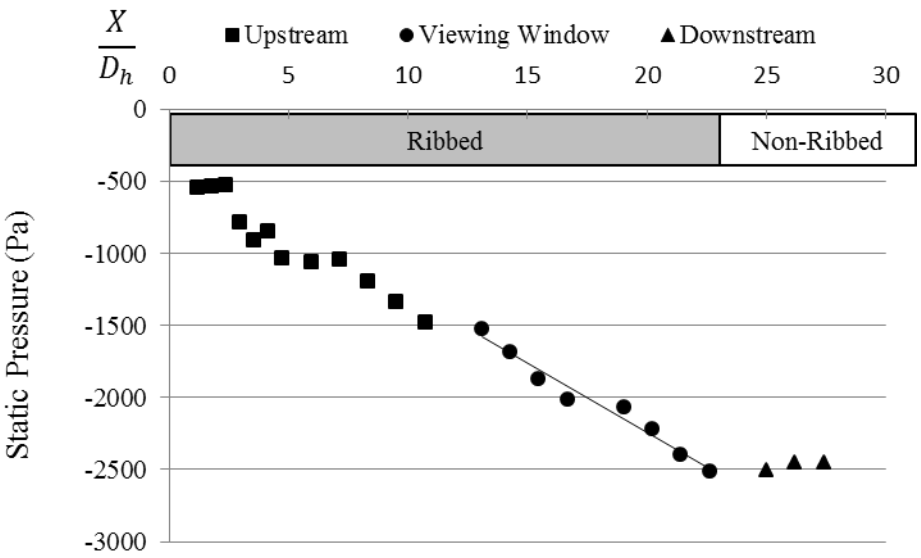

Figure 120: Static pressure distribution of Case A3 at 30,000 Re

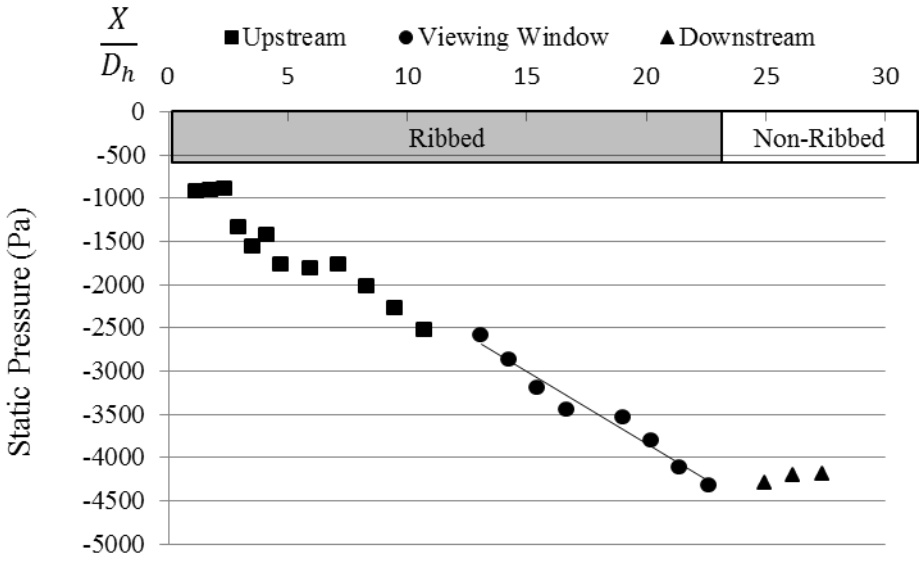

Figure 121: Static pressure distribution of Case A3 at 40,000 Re

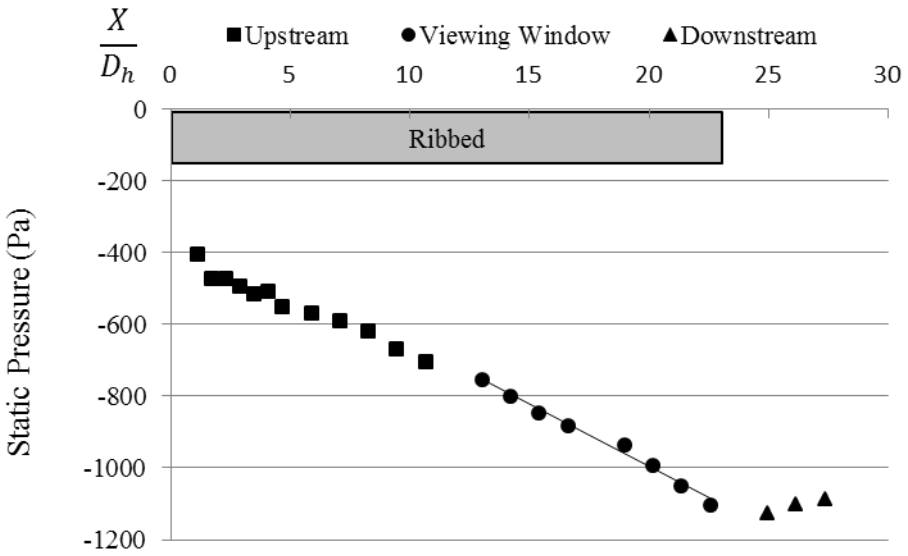

Figure 122: Static pressure distribution of Case A5 at 20,000 Re

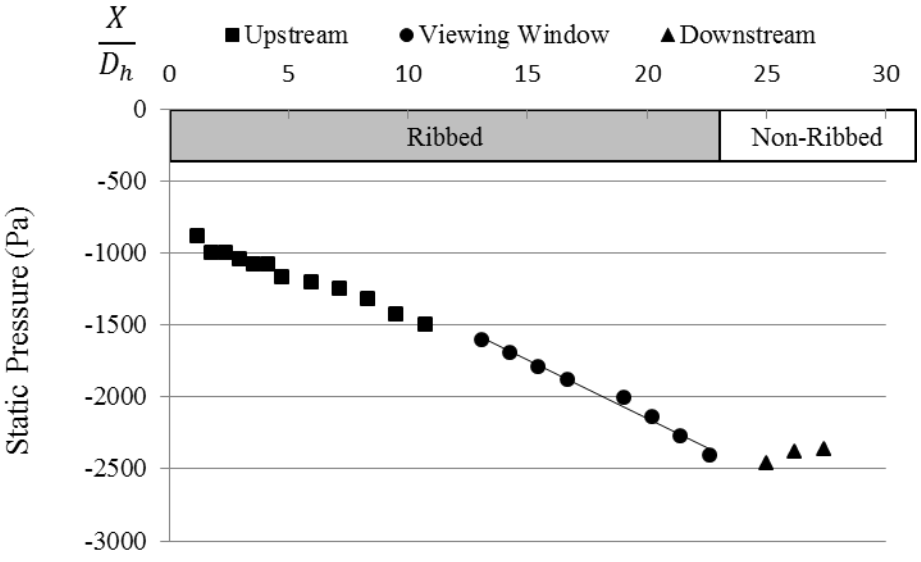

Figure 123: Static pressure distribution of Case A5 at 30,000 Re

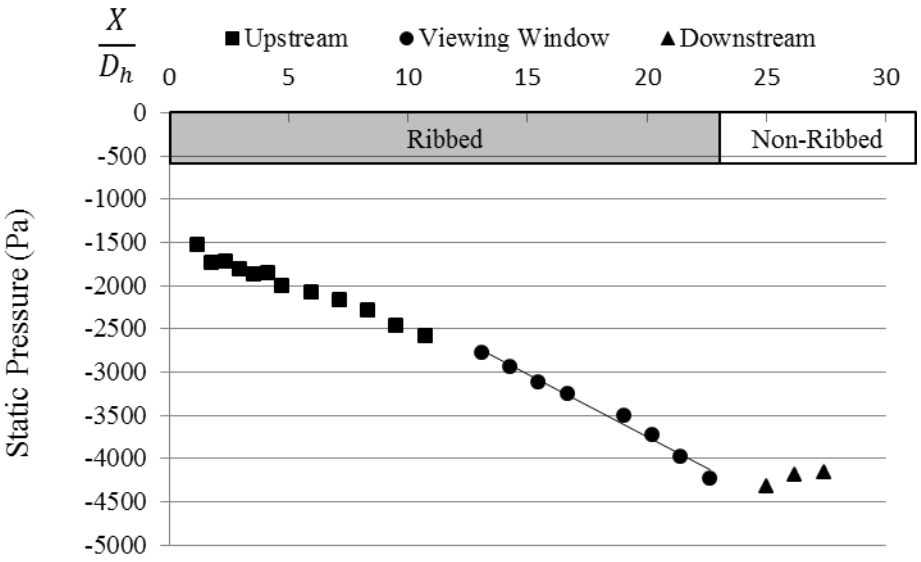

Figure 124: Static pressure distribution of Case A5 at 40,000 Re

APPENDIX B: EXPERIMENTAL FRICTION RESULTS

Table 12: Summary of experimental friction results for Case A1

Re	$\frac{\partial P}{\partial x}\ \left(\frac{Pa}{m}\right)$	f	$\frac{f}{f_0}$
20000	2240	0.362	13.6
30000	5050	0.363	15.1
40000	9800	0.399	17.8

Table 13: Summary of experimental friction results for Case A3

Re	$\frac{\partial P}{\partial x}\ \left(\frac{Pa}{m}\right)$	f	$\frac{f}{f_0}$
20000	1980	0.320	12.0
30000	4510	0.325	13.5
40000	7860	0.320	14.3

Table 14: Summary of experimental friction results for Case A5

Re	$\frac{\partial P}{\partial x}\ \left(\frac{Pa}{m}\right)$	f	$\frac{f}{f_0}$
20000	1640	0.265	10.0
30000	3780	0.273	11.4
40000	6830	0.277	12.4

APPENDIX C: EXPERIMENTAL HEAT TRANSFER RESULTS

Table 15: Summary of experimental heat transfer augmentation results for Case A1

Re	$\frac{Nu}{Nu_0}$		
	Rib	Non-Ribbed	Wall Average
20000	6.10	2.20	2.59
30000	5.95	2.13	2.51
40000	5.25	1.95	2.28

Table 16: Summary of experimental heat transfer augmentation results for Case A3

Re	$\frac{Nu}{Nu_0}$		
	Rib	Non-Ribbed	Wall Average
20000	2.74	1.39	1.80
30000	2.66	1.37	1.75
40000	2.58	1.37	1.73

Table 17: Summary of experimental heat transfer augmentation results for Case A5

Re	$\frac{Nu}{Nu_0}$		
	Rib	Non-Ribbed	Wall Average
20000	1.85	1.07	1.46
30000	1.77	1.20	1.49
40000	1.69	1.26	1.48

Table 18: Wall-averaged heat transfer results for Case A1 from TLC

A1	20,200 Re	30,000 Re	40,000 Re
Rib	6.10	5.95	5.25
Non Ribbed	2.20	2.13	1.95
Wall Averaged	2.59	2.51	2.28

Table 19: Wall-averaged heat transfer for Case A3 from TLC

A3	20,300 Re	30,000 Re	40,000 Re
Rib	2.74	2.66	2.58
Non Ribbed	1.39	1.37	1.37
Wall Averaged	1.80	1.75	1.73

Table 20: Wall-averaged heat transfer results for Case A5 from TLC

A5	20,000 Re	30,000 Re	40,000 Re
Rib	1.85	1.77	1.69
Non Ribbed	1.07	1.20	1.26
Wall Averaged	1.46	1.49	1.48

APPENDIX D: NUMERICAL FRICTION RESULTS

Table 21: Summary of numerical friction results for Case A1

A1	$\frac{\partial P}{\partial x}\left(\frac{Pa}{m}\right)$	f	$\frac{f}{f_0}$
20,000 Re	2776	0.516	19.4
30,000 Re	6328	0.523	21.8
40,000 Re	11435	0.531	23.8

Table 22: Summary of numerical friction results for Case A3

A3	$\frac{\partial P}{\partial x}\left(\frac{Pa}{m}\right)$	f	$\frac{f}{f_0}$
20,000 Re	1658	0.308	11.6
30,000 Re	4577	0.378	15.7
40,000 Re	7828	0.364	16.3

Table 23: Summary of numerical friction results for Case A5

A5	$\frac{\partial P}{\partial x}\left(\frac{Pa}{m}\right)$	f	$\frac{f}{f_0}$
20,000 Re	1698	0.315	11.9
30,000 Re	3288	0.272	11.3
40,000 Re	5295	0.246	11.0

APPENDIX F: NUMERICAL HEAT TRANSFER RESULTS

Table 24: Summary of numerical heat transfer augmentation results for Case A1

Re	$\frac{Nu}{Nu_0}$		
	Rib	Non-Ribbed	Wall Average
20000	7.86	1.61	2.24
30000	7.53	1.57	2.17
40000	7.30	1.55	2.13

Table 25: Summary of numerical heat transfer augmentation results for Case A3

Re	$\frac{Nu}{Nu_0}$		
	Rib	Non-Ribbed	Wall Average
20000	4.48	1.39	2.31
30000	4.27	1.39	2.26
40000	4.10	1.34	2.17

Table 26: Summary of numerical heat transfer augmentation results for Case A5

Re	$\frac{Nu}{Nu_0}$		
	Rib	Non-Ribbed	Wall Average
20000	3.75	1.62	2.68
30000	3.45	1.47	2.46
40000	3.26	1.37	2.31

Table 27: Wall-averaged heat transfer results for Case A1 from CFD

A1	20,000 Re	30,000 Re	40,000 Re
Rib	7.86	7.53	7.30
Non Ribbed	1.61	1.57	1.55
Wall Averaged	2.24	2.17	2.13

Table 28: Wall-averaged heat transfer results for Case A3 from CFD

A3	20,000 Re	30,000 Re	40,000 Re
Rib	4.48	4.27	4.10
Non Ribbed	1.39	1.39	1.34
Wall Averaged	2.31	2.26	2.17

Table 29: Wall-averaged heat transfer results for Case A5 from CFD

A5	20,000 Re	30,000 Re	40,000 Re
Rib	3.75	3.45	3.26
Non Ribbed	1.62	1.47	1.37
Wall Averaged	2.68	2.46	2.31